The hot phase of the ISM: Investigation of the soft X–ray background

Dissertation
zur
Erlangung des Doktorgrades (Dr. rer. nat.)
der
Mathematisch–Naturwissenschaftlichen Fakultät
der
Rheinischen Friedrich–Wilhelms–Universität
Bonn

vorgelegt von
Juan Enrique Pradas Simón
aus Madrid

Bonn, September 2004

Angefertig mit Genehmigung
der Mathematicsh–Naturwissenschaftlichen Fakultät
der Rheinischen Friedrich–Wilhelms–Universität Bonn

1. Referent: Priv. Doz. Dr. habil. Jürgen Kerp
2. Referent: Prof. Dr. Ulrich Mebold

Tag der Promotion:
Bonn, den 30. September 2004

Contents

1 Introduction

The first successful observation of an X–ray source (Sco X–1) located outside the Solar System by Giacconi et al. (1962) presented already evidence for the existence of a cosmic diffuse background in the X–ray energy regime. Already at this early stage of X–ray astronomy, this first cosmic background ever detected was found to be not isotropic, revealing significant variations in intensity as a function of the line of sight. This characteristic points to the different origin of the X-ray background in comparison to other backgrounds with cosmological origin like the Cosmic Microwave Background (Penzias & Wilson, 1965). However, the first constrains on the real nature of the X–ray Background (XRB) were delayed until the development of X–ray observatories with capabilities improved by orders of magnitude in angular and spectral resolution as well as sensitivity, in comparison with those used by Giacconi.

For the high energy region of the XRB, corresponding to photon energies above 1 keV, it has been demonstrated (Fabian & Barcons, 1992; Barber et al., 1996; Hasinger et al., 2001) that the X–ray background is not diffuse in nature. In fact, it originates from the superposition of distant X–ray sources which require prolonged exposure times to be resolved (see Fig. 1). The majority of these sources are AGNs at high redshifts (Tozzi et al., 2001). For this reason, this part of the XRB is called the *extragalactic* X-ray background, which is observed as an isotropic radiation with the bulk of its emission in the high energy X–ray regime.

However, the extragalactic origin is not sufficient to explain the entire XRB radiation. The proofs for the existence of additional components arise form the study of the soft spectral region of the XRB: the so called soft X–ray background (SXRB), with photon energies below 1 keV. In this regime, and in particular in the softest regime below 1 keV, the background radiation is highly anisotropic in contrast to the hard part of the XRB. This can be partly attributed to the photoelectric absorption caused by the interstellar medium in the soft X–rays. The calculations for this attenuation effect (Morrison & McCammon, 1983) predict an anti–correlation between the surface brightness of the SXRB and the HI column density which had been already observed during the first years of X–ray astronomy (Bowyer et al., 1968; Bunner et al., 1971). Furthermore, the high column densities within the Galactic Plane would make these regions opaque for distant soft X–rays and impenetrable for the soft X-ray radiation contributed by the extragalactic background. But this was not consistent with the observations, which detected diffuse soft X–ray radiation in practically all directions across the sky. Following this line of argumentation, Sanders et al. (1977) proposed the existence of a local contribution to the XRB, a diffuse foreground emitted by the so called Local

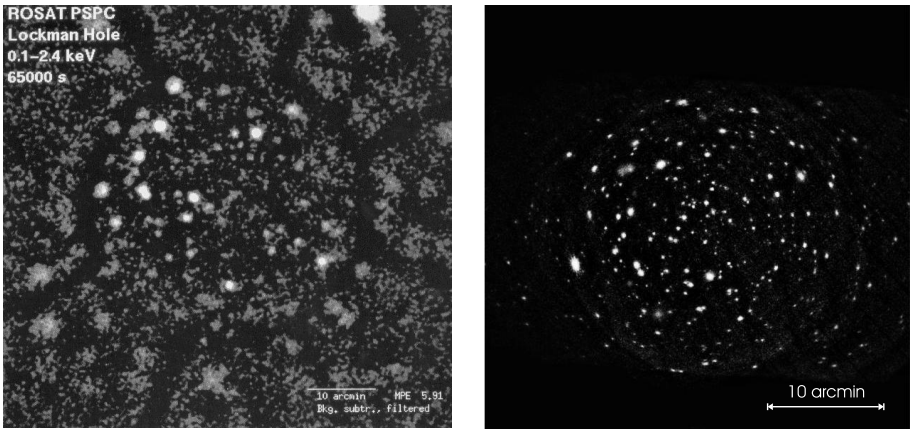

Fig. 1: **Left:** *ROSAT deep exposure in the soft X–ray regime towards the Lockman window, which is the area of the lowest absorbing column density region in the sky. In the center of the field of view, about the size of the full moon, more than 60 X-ray point sources can be identified – mostly quasars at cosmological distances. These sources were first spatially resolved from the XRB by ROSAT. At this stage, about 90% of the emission previously assumed to be diffuse was resolved into distant point sources.* **Right:** *Image of the same region as in the left panel obtained with the XMM–Newton satellite (see Chap. 3.3) for the 0.5 to 10 keV energy regime. With about 1 Ms exposure, more than 95% of the high energy background is resolved into distant point sources (Hasinger et al., 2001). Images taken from the ROSAT and ESA/XMM–Newton Science Operation Center homepages (http://wave.xray.mpe.mpg.de/rosat and http://xmm.vilspa.esa.es/, respectively)*

Hot Bubble (LHB). Thus, a hot gas ($T \simeq 10^6$K) filling the local cavity around the Sun (Paresce, 1984), with a mean radius of about 100 pc, would be the source of the part of the SXRB that could not be explained by the contribution of the extragalactic background to the soft energy regime. In the *displacement model* (see, e.g. Snowden et al. (1990)) all the variations in intensity of the SXRB were attributed to the foreground component with only marginal contribution of the extragalactic background.

Evidence for the existence of a further contributor to the SXRB was presented first by Nousek et al. (1982) and confirmed beyond any doubt in the ROSAT era. The ROSAT X–ray satellite observatory (Trümper, 1984) was launched in 1990 and became one of the most successful X–ray mission until today. Making use of ROSAT observations, Snowden et al. (1991) and Burrows & Mendenhall (1991) detected the X–ray *shadow* of an interstellar cloud situated at a distance of about 600 pc towards the Draco region (see Fig. 2). Since this shadowing could not be attributed to the attenuation of the extragalactic background, the existence of a distant Galactic component (beyond the LHB) in the SXRB was demonstrated. This component is called the Galactic X–ray Halo and its true gas distribution and properties are still a matter of debate today.

But the Milky Way Halo is not the only X–ray halo that has been observed (see Fig.

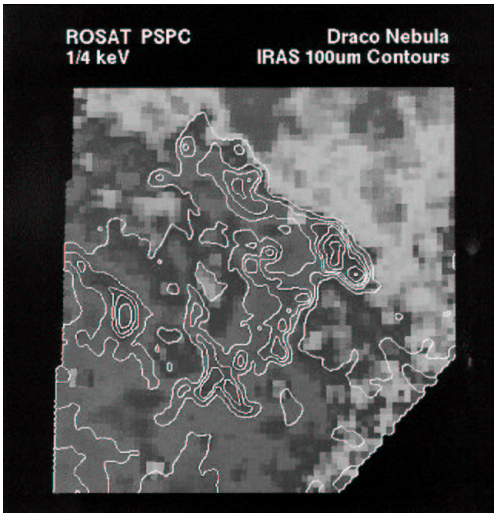

Fig. 2: *Observation of the X–ray shadow casted by the Draco Nebula in the diffuse X-ray radiation. The X–ray map, at an energy of 0.25 keV, is taken from the ROSAT homepage (*$10^\circ \times 10^\circ$ *FOV). The grey scale corresponds to the X–ray intensity distribution where the brighter means the higher X–ray intensity. The contours represent the amount of absorbing material responsible for the X–ray attenuation are derived from the IRAS 100* μm *survey. The discovery of this shadow allowed to distinguish between a foreground and a background component contributing to the SXRB. Furthermore, the absorbing material is situated about 600 pc away from the Sun, these observations indicate the existence of a Galactic X–ray Halo. Note, that no equivalent XMM–Newton image is available like in Fig 1. This is probably because of the technical problems in the data reduction still present for XMM–Newton (see Chap. 7).*

3). Moreover, numerous detections towards galaxies of different morphological types (ellipticals and spirals) and in different environments (in rich and poor clusters as well as in field galaxies) showed the ubiquity of X–ray halos (e.g. Forman et al., 1979; Kriss et al., 1980; Biermann et al., 1982; Fabbiano & Trinchieri, 1984; Trinchieri et al., 1997; Dahlem & Stuhrmann, 1998). The gaseous nature of the detected emission could be inferred from asymmetries in the X–ray isophotes of the diffuse emission. These asymmetries are attributed to ram pressure stripping experienced by the hot gas and caused by the medium in which the galaxy is moving. Thus, an origin of the detected emission by the superposition of unresolved X–ray point sources is ruled out. Examples can be found in Fabian et al. (1980) for M86 and Forman et al. (1985); Trinchieri et al. (1986) for NGC 4472. Reviews can be found in Fabbiano (1989) and Strickland et al. (2004).

With the detection of X–ray halos in other galaxies a new window for the investigation of the distribution of the Dark Matter in galaxies was opened. It is clear that the existence of a hot plasma ($10^6\,\mathrm{K} \leq \mathrm{T} \leq 10^{6.5}\,\mathrm{K}$) extending much further than the optical galaxy implies the presence of a Dark Matter halo. Otherwise the gravitational poten-

tial created by the sum of stars, gas and dust in the galaxy would not be sufficient to bind the hot gas to the galaxy. Unfortunately, the actual technology does not permit exploiting this most useful aspect of the relation between X–ray and Dark Matter halo. Ideally the radial distribution of the X–ray halo can be used to infer the shape of the Dark Matter halo. But the sensitivity of the present X–ray telescopes is only sufficient to perform these kind of studies only towards some peculiar types of galaxies. In the case of XMM–Newton, this insufficiency does not arise from the capabilities of the telescope but from technical problems in the data reduction for soft and faint diffuse X–ray emission, like the emission from the galactic X–ray halos (e.g. in Lumb et al. (2002); Read & Ponman (2003); Katayama et al. (2004)). This topic will be treated in detail in Chap. 7.

This thesis will focus mainly on the investigation of the nature and distribution of the X–ray Halo of the Milky Way based on ROSAT observations. New improved HI data of the Galactic column density distribution[1] will be used to construct consistent **all–sky** models of the SXRB in the **entire energy regime** detectable with ROSAT for the first time. The models will be compared with selected areas of the ROSAT observations in order to test some assumptions on the 3–D structure of the Galactic diffuse X–ray absorber and emitter. For instance, to give constraints to the distance to the so–called high–velocity clouds (Wakker & van Woerden, 1997). One fundamental concept in this work will be the use of new models for the emission of the Galactic X–ray Halo based in **Galactic Dark Matter Halo models** which have been deduced by independent methods (see Fig 3). The actual status of the data reduction for XMM–Newton will be also discussed in detail, with the goal to develop methods that would permit extending the investigations of the SXRB performed with ROSAT to XMM–Newton.

The structure of this thesis is as follows: In Chap. 2, we briefly introduce the physical processes involved in X–ray astronomy. Chap. 3 presents the techniques used to perform astronomical X–ray observations and some general characteristics of two X–ray observatories: ROSAT and XMM–Newton. In Chap. 4, we introduce the *phases of the interstellar medium* and present the most important effect involved in the radiative transfer of the soft X–rays through the interstellar medium: The photoelectric absorption in the X–ray energy regime. In Chap. 5 we make use of the ROSAT all–sky survey to find a consistent model for the soft X–ray background that is applied in Chap. 6 to investigate the 3–D structure of the absorber in some fields of interest –*high–velocity clouds*– and to search for traces of additional sources in the ROSAT data –*Warm/Hot intergalactic medium*–. In Chap. 7, we present our results in developing a data reduction method for XMM–Newton observations, that would permit the study of faint diffuse X–ray emission with this X–ray satellite. In Chap. 8 we summarize and give an outlook on future activities.

[1] Leiden/Dwingeelo/Argentitian Institute of Radioastronomy/University of Bonn 21 cm–line all–sky survey. The original data were published by Hartmann & Burton (1997); Arnal et al. (2000), while the latest data reduction is by Kalberla et al., in prep.

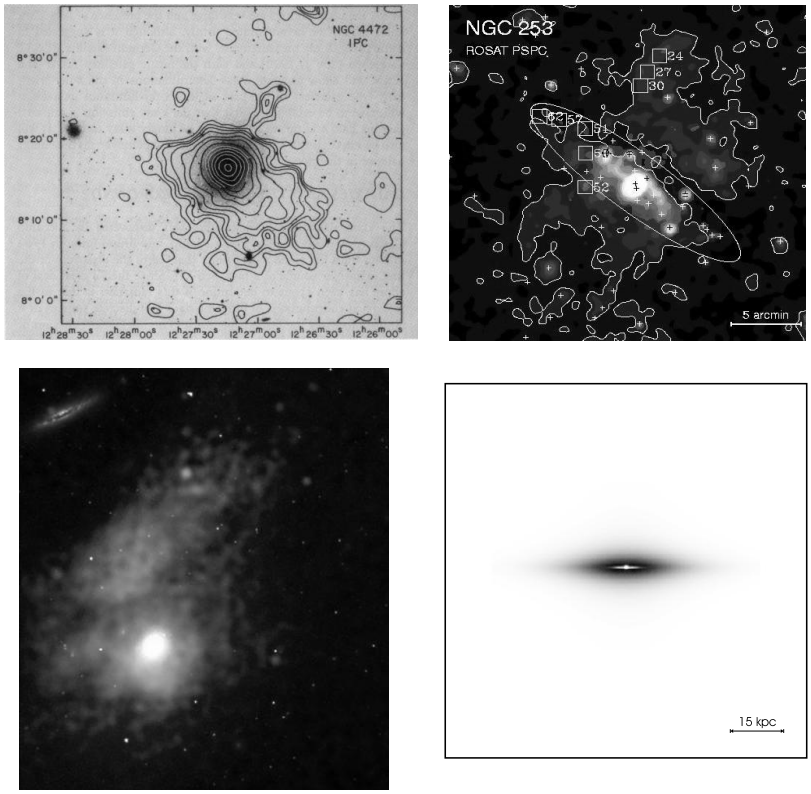

Fig. 3: **Upper left:** *Optical image of the elliptical galaxy NGC 4472 with soft X–ray contours obtained with ROSAT. The X–ray halo extends much further than the optical part of the Galaxy. The asymmetry in the X–ray distribution indicates the true diffuse nature of the X–rays because it is originated in a hot gas stripped by ram pressure of the medium that the galaxy is crossing (see more details in, e.g. Forman et al., 1985; Trinchieri et al., 1986).* **Upper right:** *ROSAT image of the edge–on spiral galaxy NGC 253. The contours indicate soft diffuse X–ray emission and the ellipse indicates the optical extension of the galaxy. Again, the X-ray halo extends much further than the optical emission, fundamentally in the direction perpendicular to the galactic plane. The high intensity region in the center corresponds to an active star forming region (Pietsch et al., 2000).* **Lower left:** *Image of the X–ray halo of giant elliptical M86 taken by Chandra. This galaxy is crossing the Virgo galaxy cluster with supersonic velocity. Consequently, the halo presents a tail extending to the upper–right of the picture like in the case of NGC 4472 (Loewenstein et al., 2001). Image form the Chandra homepage (http://chandra.harvard.edu/index.html)* **Lower Right:** *Representation of the Dark Matter Halo model for the Milky Way by Kalberla (2003). The optical extension of the Galaxy corresponds to the inner white region and the Dark Matter distribution is represented by the grey scale. Following these approaches, the gravitational potential created by the Dark Matter determines the temperature of the gas and distribution of the X–ray emission of the halos. In fact, the extension of the Dark Matter Halo is a good first approximation to the theoretical distribution of the X–ray Halo (see also Chaps. 4 and 5).*

2 Astronomical X–ray emission

In order to understand the X–ray sky, a basic knowledge of the fundamentals of X–ray physics is required. This chapter will introduce the most relevant concepts for X–ray astronomy and, in particular, for the study of astronomical *soft* X–rays.

X–rays were first identified by W. C. Röntgen in 1895, although it took still 20 years to verify the electromagnetic wave nature of the at that time called *X–radiation*. Laue showed in 1912 the diffraction of X–rays by crystals. The required wavelength in order to have diffraction in natural crystals implied, that the X–radiation should be in the range of some Å. In fact, X–rays are electromagnetic waves with a wavelength between 0.01 and 10 nm, which approximately corresponds to 0.1 KeV $\leq$ E $\leq$ 100 keV in the equivalent energy scale. Energies in this range can be easily be achieved in the laboratory by the use of X–ray tubes (sketch shown in Fig. 4).

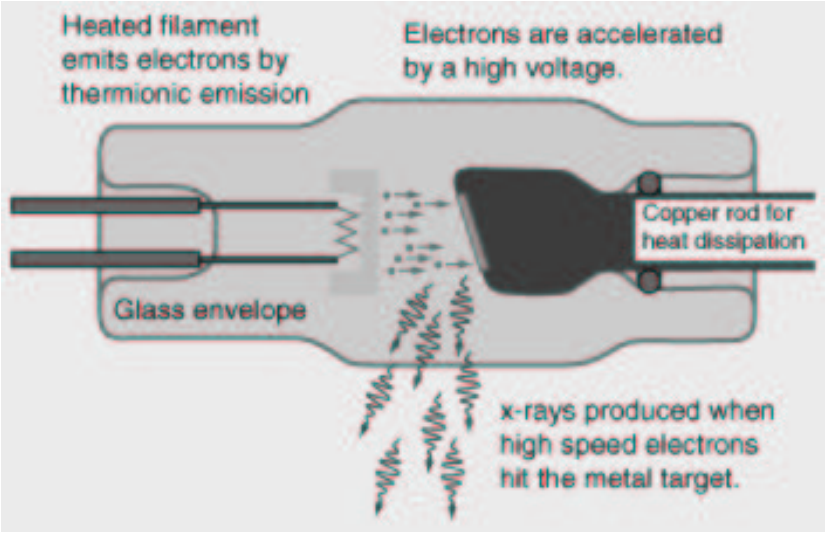

Fig. 4: *Sketch of an X–ray tube similar to that used by Röntgen for his first detections of X–rays. The electrons freed in the cathode are accelerated towards the anode by strong electrical fields. The kinetic energy acquired by the electrons is liberated in form of X–rays when the electrons impact in the anode. In the high energy part of the spectrum, non–thermal bremsstrahlung (see Sect. 2.1) dominates while discrete emission lines, characteristic of the material of the anode, dominate the low energy part. A device to dissipate the heat in the anode increases significantly the emission of the X–ray tube.*

In nature, the first indirect evidence for the existence of matter under the extreme conditions necessary for the emission of X–rays was presented by Lyot (1932). During his spectrographic investigation of the solar corona in optical wavelengths, Lyot found emission lines which did not correspond to any known element at that time. Only some years later, it was clear that the lines found by Lyot corresponded to transitions in highly ionized elements like CV or OVIII. These ionization states can only be reached in plasmas with temperatures above one million K, being these high temperatures also consistent with the considerable line broadening observed by Lyot. Finally in 1948, the X–ray emission of a hot gas in the corona of the Sun was detected directly using a X–ray detector launched with a rocket by Friedman and collaborators.

2.1 Emission processes for X–rays in Astronomy

There are several mechanisms found in the Universe which are able to produce electromagnetic radiation in the X–ray regime. It is common in the literature to divide these processes into two groups: thermal and non–thermal radiation. In thermal processes the electrons are described by a Maxwellian energy distribution characterized only by the temperature T. In the non–thermal case, charged particles with relativistic motions are involved. For X–ray astronomy, it is fundamental that most of the emission processes can be distinguished because of the significant differences in their spectra. Theoretically, the investigation of features like the spectral energy distribution or emission lines permits disentangling the nature of an X–ray source. In the following sections, we will introduce some fundamental concepts in the types of spectra encountered in X–ray astronomy.

2.1.1 Thermal emission

- **Blackbody radiation** with spectral distribution given by the well–known Planck formula

$$B_\nu(T) = \frac{2h\nu^3}{c^2}\frac{1}{e^{\frac{h\nu}{kT}} - 1} \tag{1}$$

  ν is the frequency, h the Planck constant, k Boltzmann constant, c the speed of light and T the temperature of the blackbody. The units are $\mathrm{W\,m^{-2}\,s^{-1}\,sr^{-1}\,Hz^{-1}}$. In the X–ray regime, it generally holds $h\nu >> kT$, where the Wien approximation is applicable. A blackbody is a physical idealization in which an optically thick object inside a surface at a certain temperature T absorbs all the incident radiation (Goldin & Novikova, 1988). Then, all electromagnetic radiation emerging from a perfect blackbody follows Eq. 1. Temperatures above $5 \cdot 10^5\,\mathrm{K}$ are required for a blackbody to become a significant X–ray emitter (see also Fig. 5).

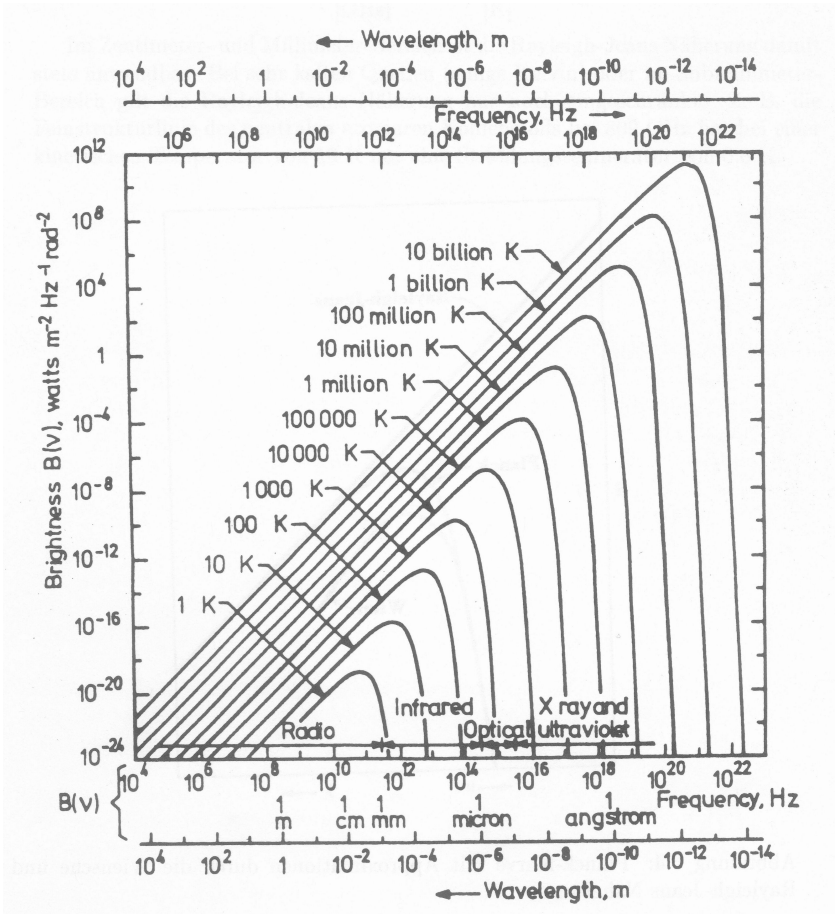

Fig. 5: *Brightness of spectrum of a blackbody as a function of wavelength. The lines correspond to the different temperatures shown. We can see that in order to have the peak intensity in the X–ray regime, temperatures approximately above* $5 \cdot 10^5\,\mathrm{K}$ *are required.*

- **Thermal bremsstrahlung**. This emission process occurs when an electron approaches an atomic nucleus. Then, there is a change in the velocity of the electron which triggers the emission of a photon. If the acceleration experienced by the electron is sufficiently strong, an X–ray photon can be emitted. The spectrum of thermal bremsstrahlung is described by functions of the from $T^{-\frac{1}{2}}e^{-\frac{E}{kT}}$ (continuum). In nature, this emission mechanism dominates the spectrum of hot optically thin plasmas with temperatures $T \geq 10^7\,\mathrm{K}$ (see also Sect. 2.2).

- **Discrete line emission** as the dominant process in an optically thin plasma with $10^6\,\mathrm{K} \leq \mathrm{T} \leq 10^7\,\mathrm{K}$ (see Sect. 2.2). This emission is produced by electronic transitions between two bound levels of an ion which is highly ionized. The excitation of the ions is regulated by collisions or by ionization produced by photons (see Sect. 2.2).

- **Radiative recombination.** This type of emission is a continuum radiation. It originates when free electrons of a plasma are recombined to the innermost bound states of highly ionized elements. Then, a photon with energy equal to the corresponding ionization energy of this state plus the kinetic energy of the electron is emitted (see, e.g., the *SPEX* documentation[2]). The specific shape of the recombination spectrum depends on the chemical composition of the emitting plasmas. In fact, a recombination spectrum shows emission edges that correspond to the ionization energies of the elements present in the plasma (see Fig 6). Quantitatively, the contribution of recombination is generally dominated by the other emission processes in X–ray astronomy and negligible for temperatures above $3 \cdot 10^7$ K (Blumenthal & Tucker, 1974).

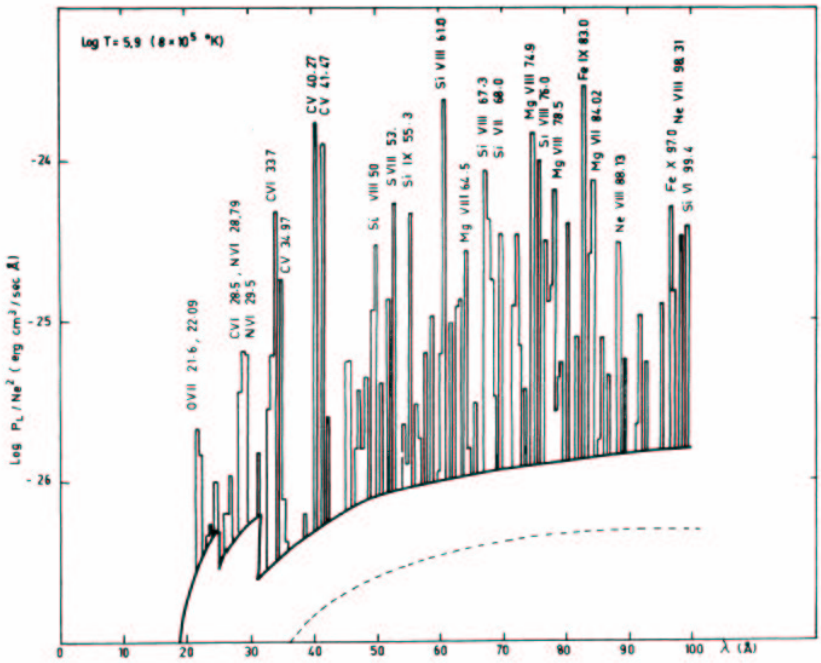

Fig. 6: *X–ray spectrum of a hot thin plasma (see Sect. 2.2.1) at temperature* $8 \cdot 10^5$ K *from Kato (1976). The dashed line indicates the contribution of the thermal bremsstrahlung emission and the solid line shows the sum of bremsstrahlung and recombination continuum. The contribution of some discrete emission lines is marked. In this range of plasma temperature, the contribution of the recombination continuum is maximized and recombination edges can be easily recognized (see also Landini & Monsignori Fossi, 1970). However, note that the contribution is about two orders of magnitude below the discrete line contribution even in the low temperature regime shown here.*

- **Dielectric recombination lines** are produced when a free electron is radiationless captured by an ion. The freed energy (ionization energy plus kinetic energy

[2] *http://www.sron.nl/divisions/hea/spex/version1.10/*

of the electron) is used to excite an electron in the innermost bound states of the ion. The ion is in a doubly excited state that leads to eventual emission of a photon in the X–ray regime. It is important to remark that neither the recombination continuum nor the lines make a significant contribution to the spectra of plasmas with temperatures in the million K range, like in the case of the sources that will be studied in this thesis.

- **Two–photon** continuum is emitted when an excited ion decays via the emission of two photons. This process occurs only when the transition is highly forbidden and, like in the case of dielectric recombination lines, its contribution is negligible comparison with thermal bremsstrahlung and discrete emission lines.

2.1.2 Non–thermal emission

- **Synchrotron radiation.** Continuum emission produced by relativistic electrons interacting with magnetic fields. Synchrotron radiation is characterized by a very high degree of polarization and its spectrum is described by a power law, with the general form $E^{-\alpha}$. Here, E is the photon energy and α is the power law index which is determined by the energy distribution of the relativistic electrons.

- **Non–thermal bremsstrahlung** which differs from thermal bremsstrahlung in the relativistic nature of the electrons involved in this process. Like in the case of synchrotron radiation, the spectrum is described by a power law.

- **Inverse Compton radiation** where high kinetic energy particles transfer a part of their linear momentum to low energy photons. With this mechanism, photons in the radio regime, for example from the Cosmic Microwave Background, can be transfered into the X–ray or even higher energy regimes.

The continuum nature of all the non–thermal processes relevant for X–ray astronomy, yields immediate differences in the spectral capabilities required for the investigation of such sources in comparison to thermal sources. Concretely, the relatively high spectral resolution required for line studies is not necessary for the analysis of non–thermal sources. Unfortunately, the latter case does not permit investigations of pressure, density and chemical composition of the source, in contrast to the possibilities which arise from spectral line analysis. Ideally, high spectral resolution allows the investigation of line widths and ratios in thermal plasmas, which can be used to infer the physical parameters mentioned above.

Finally, it is important to note that, in practice, the emission processes do not commonly occur isolated but in combinations of two to several. Thus, disentangling the nature of an X–ray source usually requires the consideration of relatively complex mixtures of emission mechanisms.

2.2 Types of cosmic X–ray sources

We have seen what kind of emission processes are relevant in X–ray astronomy. In this section, we will present the most important sources of interest in X–ray astronomy. This will be done, by briefly introducing the most important types of known X–ray sources. More details can be found in Charles & Seward (1995).

Which cosmic objects can create the conditions necessary for the emission of X–rays? Firstly, let us consider the case of sources of thermal nature, i. e. sources in which the dominant emission process is thermal. This is the case of the so–called X–ray plasmas. Apart from the plasma temperature, which has to be $T \geq 5 \cdot 10^5\,\mathrm{K}$, both the opacity and the ionization state of the plasma play a fundamental role to determine what emission processes occur in a certain X–ray source.

2.2.1 Optically thin plasma

Here, the conditions of the plasma imply that practically every emitted photon abandons the plasma, i. e. there is no self absorption in the plasma. Another condition is that collisional excitation (and ionization) dominate as heating mechanisms. Then, the dominating emission process is bremsstrahlung for temperatures above $T \geq 10^7\,\mathrm{K}$ and discrete line emission for lower temperatures (see Fig. 7). The specific lines that appear depend on the chemical composition and ionization state of the plasma. Radiative recombination is a secondary process only important for lower plasma temperature ($T \leq 8 \cdot 10^5\,\mathrm{K}$), like in the example shown in Fig. 6. In this category of sources, we find:

- **Stellar coronae** where the coronal gas of stars is heated to $T \simeq 10^6\,\mathrm{K}$. The most important heating process for the coronal gas of stars is magnetic reconnection but also heating by shock waves originated in the convective energy transport layer of the star is possible (for details see Charles & Seward, 1995).

- **Supernova remnants.** The environment of a SN is heated into the million K range by the shock generated in the gravitational collapse of the nucleus of the SN.

- **Galaxy clusters.** Galaxy clusters aggregate primordial gas in the intra–cluster medium during their formation phase. This gas has a cross section vs. itself different from zero. Therefore, the gas already aggregated in the cluster is heated by shocks originated by the in–falling gas. With this process, temperatures in the range $2 \cdot 10^7\,\mathrm{K} \leq \mathrm{T} \leq 2 \cdot 10^8\,\mathrm{K}$ are reached (Dekel & Ostriker, 1999). With densities below 10^{-3} cm^{-3}, the time required for the intra–cluster gas to radiate half of its energy is longer than 10^9 years. The cooling is done mainly by line

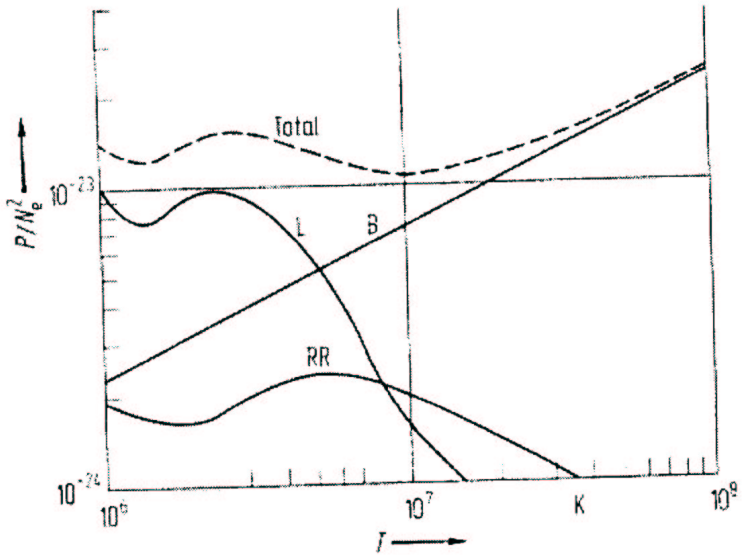

Fig. 7: *Emissivity of an optically thin plasma as a function of temperature. The total emission (dashed line) is shown as the superposition of the contribution of the different thermal emission mechanisms (solid lines). L corresponds to discrete line emission, B to thermal bremsstrahlung and RR to radiative recombination. Image taken from Fink & Trümper (1982)*

emission of highly ionized metals. The heating of the gas is done by galaxy interaction, in the sense that tidal stripping between close–by galaxies in the cluster inserts hot has in the intra–cluster medium. This mechanism also enriches the cluster gas until typical metal abundances about 0.3 to 0.5 solar (Charles & Seward, 1995). Another remarkable characteristic of the hot gas in galaxy clusters is that its total mass is larger than the sum of the optical masses of its galaxy members. Thus, the discovery of X–rays from galaxy clusters (Gursky et al., 1971) doubled the observable mass in the Universe.

- **X–ray halos in galaxies.** The X–ray emission of optically thin plasmas with temperatures about $10^6\,\mathrm{K} \leq \mathrm{T} \leq 10^7\,\mathrm{K}$ has been detected associated to the halo of all types of galaxies (see Fig. 3). In Chap. 5 we will study this emission in detail in the case of the Milky Way. For external galaxies, we can classify the X–ray halos depending on the origin of the hot gas in halos from "normal" galaxies and halos from *starburst* galaxies. These latter are galaxies where the star formation rate is above $10\,M_\odot \cdot \mathrm{year}^{-1}$. This activity generates considerable amounts of X–ray gas which is expelled into the galactic halo. If the mass of the galaxy is small, like $M \simeq 10^{10} M_\odot$ for the case of NGC 253 shown in Fig. 3, the vertical extension of the hot gas can reach up to more than 10 kpc. In the case of "normal" galaxies, the distribution of the hot gas is related to the distribution of Dark Matter halo of the galaxy. With densities of the order of

$n \simeq 10^{-3}\,\mathrm{cm}^{-3}$ the *cooling time* for the X–ray plasma is in the 10^8 years $\leq t \leq 10^9$ years range. The heating of the gas after the formation of the halo can be attributed to stellar activity (stellar winds and SNe). Some spiral galaxies present a "two component" scenario with a hotter plasma concentrated in the disk surrounded by a cooler gas (halo) like in, e.g., M83 with $T \simeq 6 \cdot 10^6\,\mathrm{K}$ and $T \simeq 2 \cdot 10^6\,\mathrm{K}$ respectively (Ehle et al., 1998). Elliptical galaxies present isothermal halos ($T \simeq 10^7\,\mathrm{K}$) with typical metal abundances about 50% solar.

- **Hot gas bubbles in galaxies.** Cavities in the interstellar medium of galaxies which are filled with hot gas heated by SN, stellar winds and/or the radiation of young OB stars (Chu & Mac Low, 1990). If the gravitational potential of the galaxy is too low, the hot plasma can be rapidly expelled to the galactic halo or even the intergalactic medium.

- **The warm/hot intergalactic medium?** (WHIM). Following the predictions of actual cosmological models for structure formation in the Universe, a hot ($10^5\,\mathrm{K} \leq \mathrm{T} \leq 10^7\,\mathrm{K}$ in Kravtsov et al. (2002)) ionized gas in the intergalactic medium should be emitting in the soft X–ray regime. We used the interrogation mark at the beginning of this point because the *emission* that the models predict has not been unambiguously detected yet. However, traces of intergalactic gas with a temperature compatible with that of the WHIM have been reported in absorption line studies of distant sources (e.g. Fang et al. (2002); Nicastro et al. (2002) in the X–ray regime and Richter et al. (2004) in the UV). The X–ray emission of the WHIM will be treated again in Chap. 6.

Since the main topic of this work is the X–ray halo of the Milky Way, the emission of optically thin X–ray plasmas will be of especial importance in the following chapters. There, synthetic spectra of optically thin plasmas will be needed for constructing models of the emission of the Galactic X–ray Halo (and of the Local Hot Bubble). The first successful approach to model the emission of an astronomical optically thin plasma was performed by Elwert (1956) for the study of the solar corona. In the present, the so called *coronal models* for X–ray emission are very accurate in their predictions. This is achieved by using detailed information of a large amount of emission lines and high precision in the calculations. Commonly used examples of this synthetic spectra are the Raymond–Smith (Raymond & Smith, 1977) and the MeKal (Mewe et al., 1985; Liedahl et al., 1995) plasmas (see also Fig. 8).

2.2.2 Optically thick plasma

In optically thick plasmas, the photons that are emitted in the interior are heavily scattered before exiting the plasma. This results in a blackbody–dominated spectrum for such plasmas. Ionization absorption lines/edges originated from the material in the

environment of the source can be also present in the spectra. This kind of emission is related to:

- **X-ray bursts** originated by thermonuclear flashes on the surface of a neutron star (NS) in a binary system (for details Charles & Seward, 1995).
- **Cataclysmic variables and supersoft sources.**(SSS) These are related to binary systems with one white dwarf (WD) as component. The blackbody radiation is produced by thermonuclear fusion on the surface of the white dwarf (review in Kahabka & van den Heuvel, 1997).

A binary system is involved in all three types of sources presented in this section. This stems from the necessity for an accretion process in order to "trigger" the emission in the surface of the compact object (NS or WD).

2.2.3 Accreting systems

The suggestion of accretion as a mechanism for X–ray radiation was introduced by Bondi & Hoyle (1944) (see also Bondi, 1952) for the case of a body traveling through an uniform density medium, such as interstellar space. In their approach, a compact object, such as a WD, a NS or a black hole (BH) is inside a "flow of material". This material can directly fall onto the surface of the compact object producing then X–ray emission. Pringle & Rees (1972) proposed an alternative model without the necessity for a flow of material, which has also evolved until becoming a standard model in the present. In this latter model, a compact object extracts matter from a *donor* object (a star or the interstellar gas in the central regions of a galaxy) along the Roche lobe. Because of conservation of angular momentum, the extracted matter is accumulated in an *accretion disk* around the compact object. Then, the action of dissipative processes (e.g., friction) in the inner part of the accretion disk decelerates the material, which falls towards the compact object. The freed gravitational energy is very efficiently radiated in the X–ray regime. In fact, the most luminous X–ray sources in the sky are related to accreting systems and not to thermal processes (see Tab. 1). Despite this remarkable property of accreting systems, there is a theoretical upper limit for the luminosity of such a system given by the *Eddington luminosity* (L_{Edd}). This limit emerges from the impossibility of accretion of material when the out–coming radiation pressure dominates over the gravitational attraction. The *Eddington luminosity* depends on the total mass of the accreting object M. It is given by (Charles & Seward, 1995):

$$L_{Edd} = 1.2 \cdot 10^{38} \frac{M}{M_{\odot}} \ \mathrm{erg\,s^{-1}} \tag{2}$$

Generally, the X–ray spectra of accreting systems are well described by power law model. However, combinations with other models (e.g. blackbody, discrete line or synchrotron radiation) might be required in practice due to the contribution of the environment of the non–thermal source to the observed spectra. Depending on the type of donor and of compact object present in the system, we find:

- **High mass X–ray binaries** (HMXB). The donor is an early–type massive star with strong stellar wind. In this case, the material from the wind which is captured by the compact object falls directly onto its surface. The potential energy is released in the form of X–rays that are added up to the emission of the accretion disk (for details see Charles & Seward, 1995). When the accreting object is a black hole, the emission is originated outside the event horizon. The Bondi–Hoyle accretion model can be applied quite straightforwardly for this kind of objects.

- **Low mass X–ray binaries** (LMXB). Sco X–1, the first extrasolar X–ray source ever detected (Giacconi et al., 1962), belongs to this group of sources where the donor is a low mass star with no significant stellar wind (see Schulz, 1999). Only the accretion process (Pringle–Rees model) is responsible for the bulk of the emission, which is then associated to the accretion disk. This is in contrast to the *wind induced* part detected in HMXB where the material falls directly onto the surface of the compact object. Finally, we remark that most of the sources mentioned in Sect. 2.2.2 are related to LMXB and not to HMXB systems.

- **Active galactic nuclei** (AGN). The donor is the interstellar medium of a galaxy (it might be of several galaxies in the case of a galaxy merger) and the accreting object is a super–massive black hole. In addition to the continuum power law emission produced by the accretion process onto the BH, there is a large variety of types of emission lines in the spectra form AGNs. The *unified model* for the AGN emission (more details in Charles & Seward, 1995), proposes that those lines are produced by different types of objects located close to the main X–ray source and in the line sight of the observer (e.g., broad and narrow line regions).

Tab. 1: *Summary of the astronomical types of X–ray sources presented in Sect. 2.2. Typical X–ray luminosities of the objects L_X are in* $\mathrm{erg\,s^{-1}}$ *(logarithmic units). The values are taken from:*[1] *Charles & Seward (1995),* [2] *Fabian (1999),* [3] *Dekel & Ostriker (1999),* [4] *Fabbiano (1989),* [5] *Schulz (1999),* [6] *Kahabka & van den Heuvel (1997),* [7] *Chu & Mac Low (1990).*

Source	L_X
AGN[2]	40 – 47
Galaxy clusters[3]	42 – 45
Galatic halos[4]	38 – 43
HMXB[1]	37 – 38
LMXB[5]	36 – 38
Supernova remnants[1]	35 – 38
SSS[6]	36 – 38
Hot bubbles[7]	34 – 37
X–ray bursts in NS[1]	33 – 38
Stellar coronae[1]	26 – 33

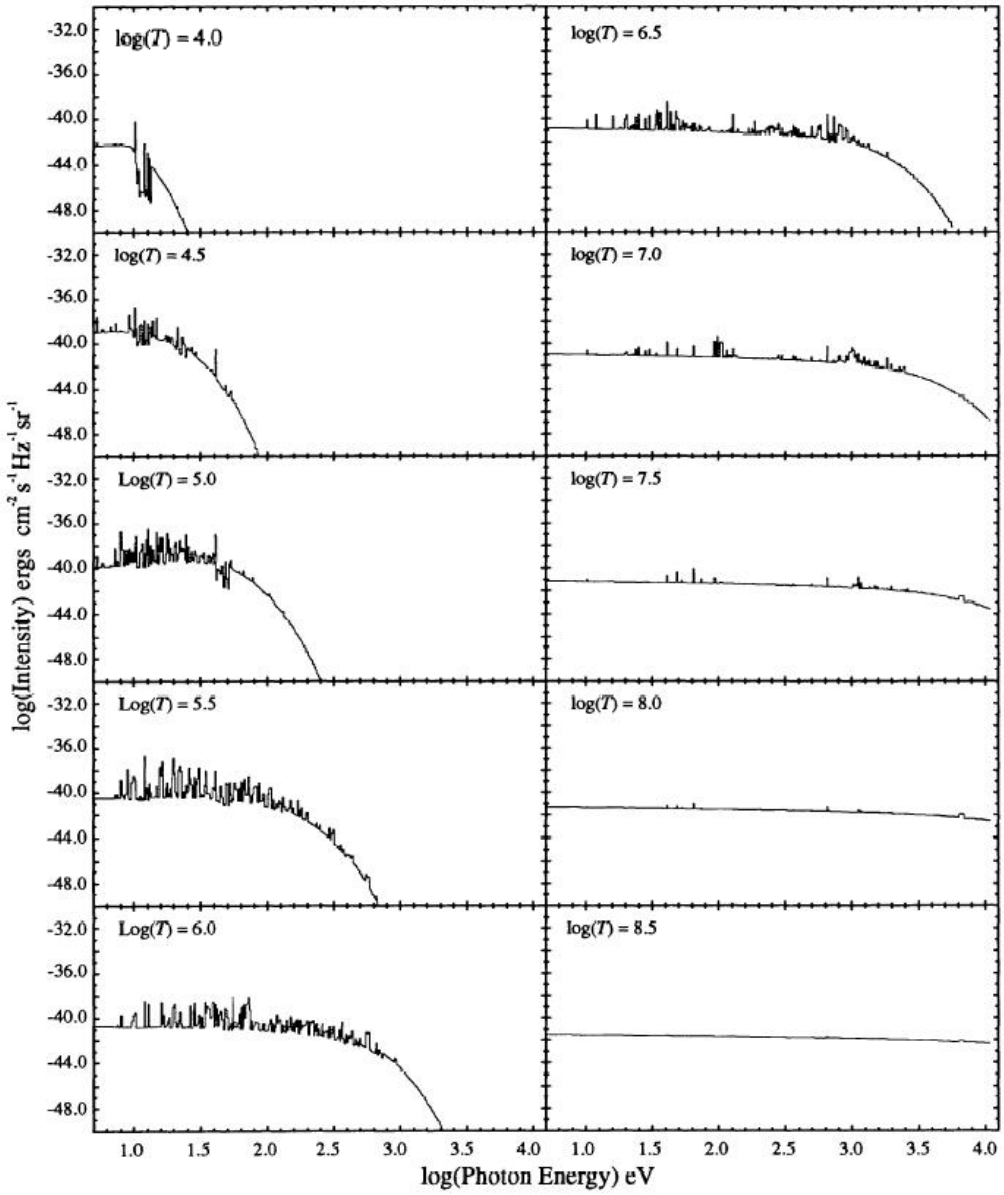

Fig. 8: *X–ray spectra in the range form 5 eV to 11 keV for thin plasmas with solar metalicities, as given by Sutherland & Dopita (1993). Temperatures of* $\log(T) = 4.0 - 8.5$ *in 0.5 steps are shown. For the highest temperature, continuum bremsstrahlung dominates.*

3 Detection of Cosmic X–rays. Observatories

In the preceding chapter, we presented a brief introduction to various emission mechanisms that are observed in X–ray astronomy. But until this point, no statement has been made about what are the techniques which have to be used to detect these astronomical sources. We will treat this topic in the following.

3.1 First X–ray Detectors in Astronomy

As already mentioned in chapter 1, the beginning of X–ray astronomy was delayed until 1948 in which the first observations of X–rays originated in the solar corona were performed. The late birth of this field in astronomy is based, like in the case of radio astronomy, because of technological problems. But different to radio telescopes, the difficulties did not only arise from the construction of efficient detectors and antennas, but in the high altitude required to perform astronomical X–ray observations (see Fig. 9).

The neutral and the partly ionized elements and molecules in the atmosphere are responsible for the photoelectric absorption of cosmic X–rays when they enter the higher layers of the atmosphere of the Earth. Such photoelectric absorption is so efficient that the Earth's atmosphere is opaque for X–rays for altitudes below 100 km. Thus, it is clear that astronomical observations of X–rays must be performed at altitudes higher than 100 km. A technology which permits reaching such altitudes was not developed until the late forties. Only at that time, scientists were able to launch X–ray detectors loaded in rockets and perform the first X–ray observations of the solar corona. The first report on confirmed X–ray emission from the Sun is form Friedman et al. (1951)

In the first years of astronomical X–ray observations, the detectors used were simple photographic plates. These were protected from optical and ultraviolet light (thin Beryllium layers in the case of the solar observations by Friedman). The plates were recovered after completion of the observation to perform the data reduction and analysis. For obvious reasons, the duration of the observations was very short and there was very limited information about the detection time of the X–ray photons. Another important drawback of the photographic plates was its non–linear response to the energy of the incoming photons.

The problems of the registering the detection times of the X–ray *events* (detection of an X–ray photon) and of linearity, were overcomed by the introduction of *proportional*

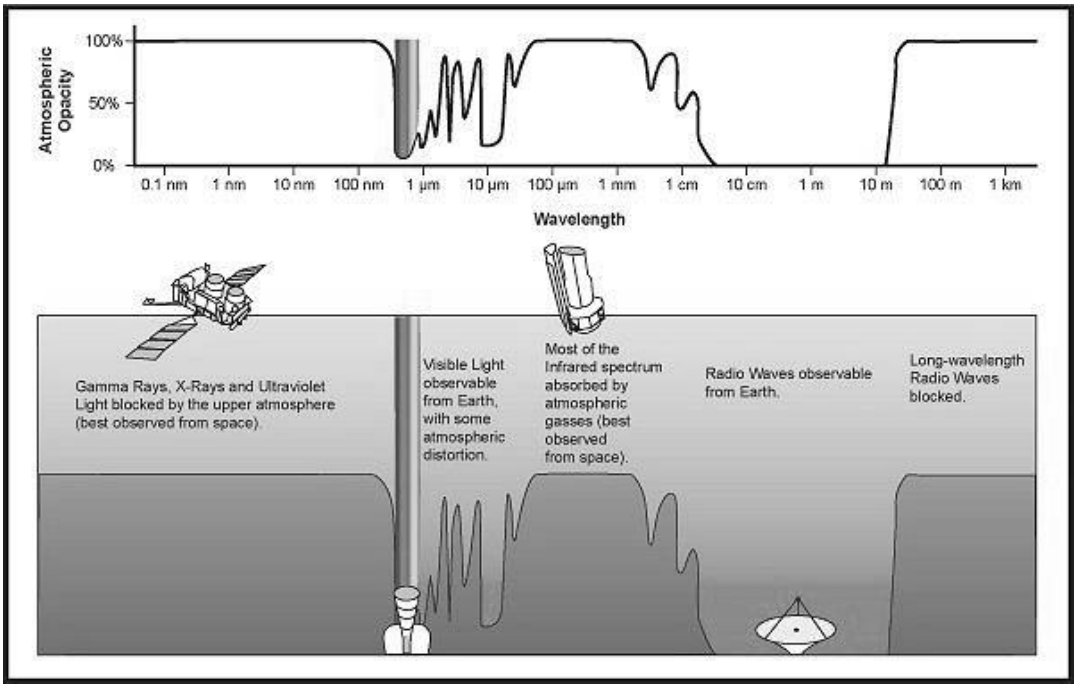

Fig. 9: *Opacity of the Earth's atmosphere. Observations form the surface of the Earth are only possible in the optical and radio windows. X–ray telescopes must be elevated above more than 95% of the atmosphere, at altitudes above about 100 km.*

counters as detectors. The functionality of these instruments is very similar to that of a Geiger–Müller counter. It is schematized in Fig. 10 and a detailed description of a real, but more modern detector can be found in Pfeffermann & Briel (1986). The registration of the event detection time is enabled, quantum efficiency was dramatically increased in comparison to photographic plates and also linearity is the response is achieved. With all these characteristics, proportional counters meant a fundamental step forward in X–ray astronomy. Eventually, it all led to the detection of the first extrasolar X–ray source by Giacconi in 1961.

The next milestone in instrumental X–ray astronomy was the first use of satellites as observatories. The first of those was UHURU, launched in 1970. At that point of time, very long integration times as well as the systematic search for cosmic X–ray sources were possible for the first time. In this context, UHURU performed the first *all–sky survey* in the X–ray regime. The results of this survey were astonishing: 339 new X–ray sources were discovered. Note here, that the first observations of the solar corona performed 20 years before had concluded that, taking into account the very low fluxes detected from the Sun (which would make it undetectable at a distance of only a few pc), X–ray astronomy had only a very limited interest. After the first detection by Giacconi and then with the results of UHURU, it was evident that there must exist

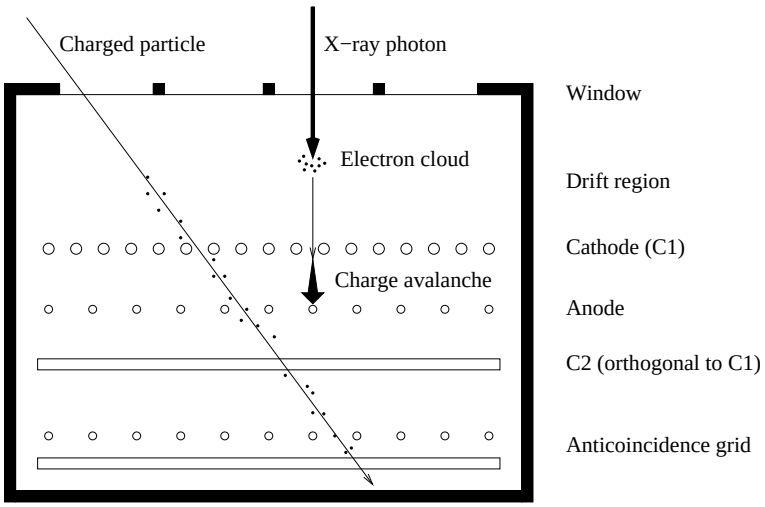

Fig. 10: *Schematic cross–sectional view of a proportional counter. An incoming X–ray photon ionizes by photoelectrically absorption an atom of the gas that fills the detector. The strong electric field generated by the charged wires accelerates the freed electron towards the anode. Further atoms of the gas are ionized by collisions with the primary electron. When consequent charge avalanche arrives to the anode, it produces measurable currents that are proportional to the energy of the original X–ray photon. An appropriate design of the cathodes and the anodes enables the imaging capability (e.g., orthogonal grids). Additional electrodes like in this Fig. can be used to discard charged particle events (e.g., PSPC carried by ROSAT, see Sect. 3.2).*

X–ray sources in the Universe different to the faint stellar coronae, like that of the Sun. Furthermore, these sources seemed to be quite numerous.

Ten years after the UHURU mission the first satellite with *imaging* detectors was launched: HEAO–2 (also known as Einstein). Imaging detectors are not only capable of counting X–ray events occurred inside a field of view, but they produce **maps** of the events inside the field of view. In practice, this is also translated in a more reliable non–X–ray background subtraction from the raw data and, therefore, a better source detection. For example, the major contribution to this contaminating background can be attributed to charged particles in the Earth's upper atmosphere. Since these particles are observed independent of line of sight and can enter the detector from any direction, the corresponding events are wide spread in the map. In contrast the X–rays from a cosmic point source will be concentrated in a small area of the detector. Some more details on the typical contamination effects of X–ray astronomy will be given in Sects. 3.2.3 and 3.3.3.

The observations performed with HEAO–2 resulted in the detection of some thousands of new X–ray sources. High–resolution spectral data were also provided. But it only took ten years until the number of detected sources by HEAO–2 was augmented dramatically by almost two orders of magnitude again.

3.2 The *Röntgensatellit* ROSAT

Launched in 1990, the German–Anglo–American satellite mission ROSAT (Trümper, 1984) has been one of the most successful X–ray observatories until the present. It had two main scientific objectives: the realization of the first all–sky survey with an imaging X–ray telescope and the detailed observation of selected X–ray sources. Its remarkable capabilities in angular resolution and sensitivity permitted the detection of more than 10^5 sources and the completion of the **most sensitive all–sky survey** in the X–ray regime to date. In fact, the sensitivity of the ROSAT all–sky survey (RASS) was comparable to the mean sensitivity of the HEAO–2 pointings!

For the achievement of these objectives ROSAT was equipped with a high–resolution imaging detector (HRI) and two position sensitive proportional counters (PSPC), which also offered imaging capabilities. The latter, with a relatively wide field of view of 2°, was mounted in order to perform the all–sky survey and will be briefly described in Sect. 3.2.2.

The focusing of the X–ray photons was performed in ROSAT by four nested *Wolter I* type mirrors made of ceramic material. The *Wolter I* design, originally developed for an X–ray microscope, was adapted for X–ray astronomy by Giacconi. We will now outline its basic concepts.

3.2.1 X–ray Optics

Because of the high penetrating power of X–rays they can not be reflected using a normal incidence mirror. Using such a geometry X–rays would only scatter or be photoelectrically absorbed in the mirror itself. Reflection of X–rays can be only achieved when they incide with an angle below the *grazing angle* θ given by:

$$\theta \propto \frac{\sqrt{\mathrm{Z}}}{E} \tag{3}$$

where Z is the atomic number of the material of the mirror and E the energy of the incoming photon. Under this critical angle occurs *total reflection*. In the X–ray energy regime, this critical angle is about fractions of degree. This obliges to construct mirrors with surfaces almost parallel to the optical axis of the telescope. Then, the *effective area* of the mirror is reduced by $\sin(\theta)$ with respect to the *geometric area*. More complications arise from the focal distances of even hundreds of meters obtained by using only parabolic mirrors. A telescope with such dimensions could not be launched into orbit.

In order to maximize the effective area and shorten the focal length the mirror system of *Wolter I* type schematized in Fig. 11 can be used.

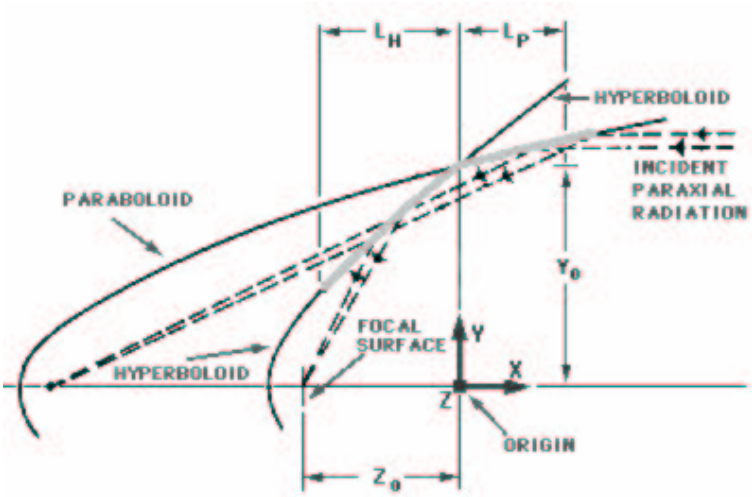

Fig. 11: *Geometry of a Wolter I type telescope. Incoming X–ray photons are reflected under the grazing angle towards the focus of the paraboloid. This focus is also one of the focus of the hyperboloid. Then, when the X–ray coming towards one focus of the hyperboloid are reflected a second time, they are redirected towards the second focus of the hyperboloid. This concept reduces significantly the focal length of the telescope. The effective area is increased by accumulating parallel concentric mirrors (nested mirrors). The image is taken from the XMM–Newton homepage.*

However, complications are still present in the mirrors shown in Fig. 11. The dependency on the photon energy of θ (Eq. 3) implies that the mirrors are chromatic. Furthermore, for the higher photon energies, the focal distance is so large that the reflected photon might not even cross the detector resulting in that the outer mirrors of a nested system might be unusable for high energy photons. In practice, there are two fundamental effects derived from the chromatic nature of the X–ray mirrors that must be taken into account:

- **Dependency of the effective area on photon energy** because θ decreases with photon energy and so does $\sin(\theta)$. Thus, the effective area decreases with increasing photon energy.

- ***Vignetting***, of special importance for the analysis of diffuse radiation. It consists in a decrease in effective area for increasing *off–axis* angle at a fixed energy. Here, off–axis angle means the angular distance form the source to the optical axis of the mirror measured in the focal plane.

3.2.2 Some Technical Specifications of ROSAT

ROSAT was designed to cover the energy regime between 0.1 keV and 2.4 keV. Its four nested mirrors provided a total geometric area slightly above 1000 cm^2 (the effective area at 1 keV was about 200 cm^2). The angular resolutions were $3.5''$ and $30''$ for the HRI and the PSPC respectively, at the 1 keV energy regime. With these characteristics ROSAT was the most sensitive X–ray observatory at its time.

The PSPC detector also measured the photon energy of the detected events. This capability stems from the proportionality between the incoming photon energy and the charge of the electron cloud detected in the anode of a proportional counter (Charles & Seward, 1995). The energy resolution of the PSPC at energy E in keV is given by:

$$\frac{\Delta E}{E} = 0.43\sqrt{\frac{0.93}{E}} \tag{4}$$

Eq. 4 (Pietz, 1997) gives the energy resolution of the instrument at a specific energy. It can be also interpreted as the degradation produced by the instrument in the observed spectrum. By considering the smearing of the individual photon energies across the entire bandpass of ROSAT, it is possible to calculate the so–called *Detector Response Matrix* (DRM). The combination of the DRM with the properties of the mirror reflexion and of the transmission of the detector's entrance window permits establishing the relation between the real emitted spectrum of a X–ray source and the *Pulse Height Distribution* measured by the PSPC (see the *ROSAT User's Handbook*[3] for a detailed description). In addition to the effects mentioned above, also the quantum efficiency of the detector and the chromatic attenuation suffered by the emission of the source when it crosses the interstellar medium (see photoelectric absorption in Sect. 4.2) must be considered to obtain the relation between the real spectrum of the source and the measurements.

The Pulse Height spectrum is formed by 256 channels, with about 10 eV bandwidth each, covering the energy range $0.1\,\mathrm{keV} \leq E \leq 2.4\,\mathrm{keV}$. However, due to the relatively low energy resolution given by Eq. 4, neighboring channels are not statistically independent. The statistical dependency of the energy channels has important consequences for the study of faint X–ray sources, as we will see throughout this work (Chaps. 5 and 7). In order to improve the signal–to–noise ratio of faint sources and eliminate redundant information originated from the statistical dependency of the channels, some independent *broad energy bands* (see Tab. 2) are of common use. Bands R1 to R7 cover almost the entire ROSAT energy regime and the bandwidth is sufficient to assure acceptable photon statistics in each individual band, even for faint diffuse sources. RC, RM and RJ are broader and have a historical motivation (Wisconsin survey McCammon et al., 1983).

[3] *http://wave.xray.mpe.mpg.de/rosat/calibration*

Tab. 2: *ROSAT PSPC commonly used broad energy bands. Name of the band and energy interval covered are given. Taken from the ROSAT homepage*

Band	E_{min} [KeV]	E_{max} [KeV]
R1	0.11	0.284
R2	0.14	0.284
R3	0.20	0.83
R4	0.44	1.01
R5	0.56	1.21
R6	0.73	1.56
R7	1.05	2.04
RC	0.11	0.284
RJ	0.44	1.21
RM	0.73	2.04

3.2.3 The ROSAT All-sky Survey

One of the most important scientific products of ROSAT is its all–sky survey (RASS, see Figs. 12, 13 and 14), which was completed using the PSPC during the first six months of operation the satellite. This was the first use of an X–ray imaging detector to perform an all–sky survey with the consequent improvement in sensitivity with respect to the *scanning* instruments like UHURU (Charles & Seward, 1995). In fact, the RASS is the most sensitive X–ray all-sky survey to date and it will be the data set that we will use for our quantitative study of the SXRB in Chap. 5.

The data acquisition and analysis method used to construct the RASS can be summarized as follows (a detailed description can be found in Snowden et al. (1995, 1997)). During *phase I* of the ROSAT mission, the satellite flew in a synchronous orbit, meaning this one revolution per orbit around the vector towards the Sun. The solar panels of ROSAT were always directed towards the Sun permitting continuous observations. Combined with the motion of the Earth around the Sun, an all–sky scan can be completed in six months. Since the FOV of ROSAT is 2°and the motion of the Earth corresponds to 1°per day, all directions in the sky can be observed in a two day period. The resulting maps, showed in Figs. 12 to 14, can be calculated by using the event lists produced by the scan and the information available on the orbit of the satellite. In other words, since the photon events (see Sect. 3.1) are registered also with detection time, determining the incoming direction of the photon is reduced to knowing which was the satellite pointing direction at detection time (given by the orbital parameters).

The strategy followed to complete the all–sky survey has immediate consequences in the precision of the observations. Concretely, there is a significant dependency of the sensitivity of the survey on the pointing direction, as it can be seen in the so

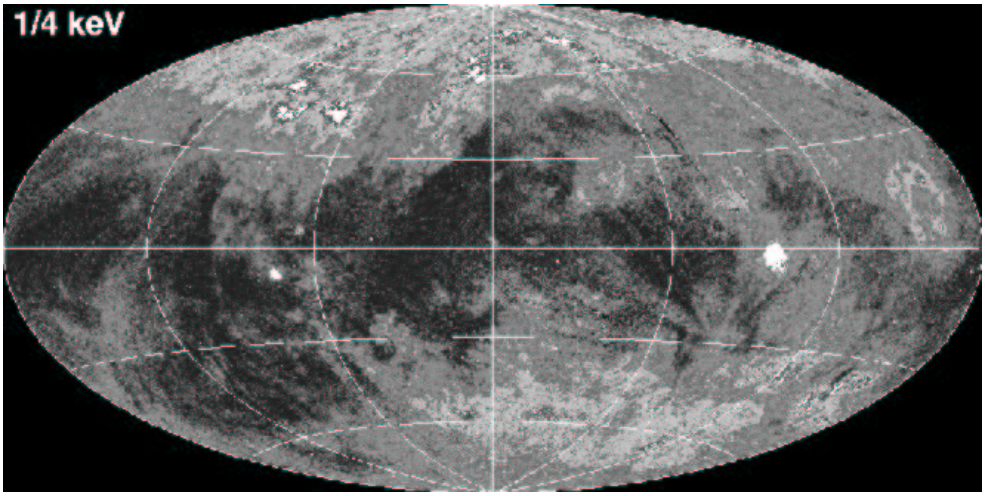

Fig. 12: *RASS sky map in the RC (1/4 keV) band energy range with an Aitoff equal-area projection. The map is centered at the Galactic Center with the North Galactic Pole at the top of the map. In general, the X–ray intensity distribution appears very structured. High X–ray intensity is represented with the bright regions. These are concentrated at high Galactic latitudes in contrast to the low intensities towards the Galactic Plane. All images from Fig. 12 to 14 are taken from the ROSAT homepage.*

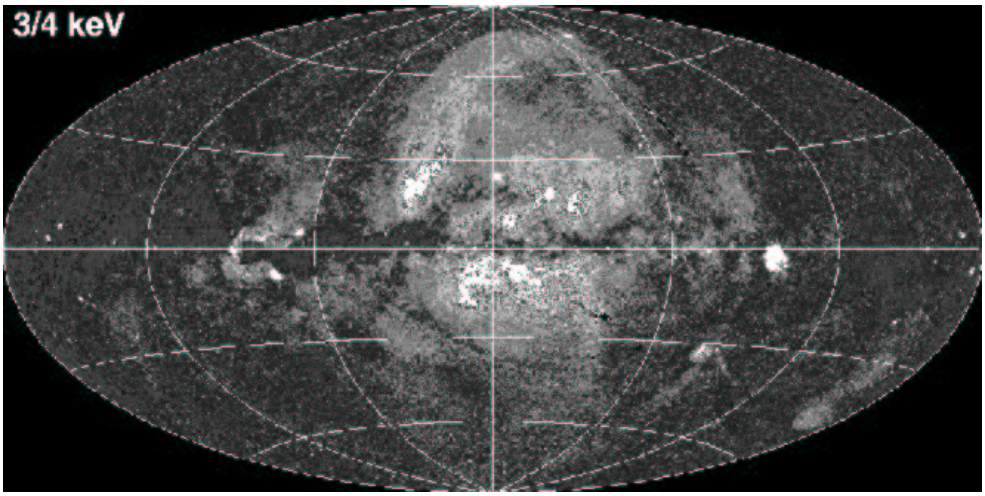

Fig. 13: *RASS sky map in the RC band energy range. Same projection than Fig. 12. The intensity is more isotropically distributed than in the RC band. The exceptions can be identified as SNr like Vela in the Galactic Plane ($l \simeq 250°$) or the North Polar Spur: the extended structure dominating the northern hemisphere towards the Galactic Center.*

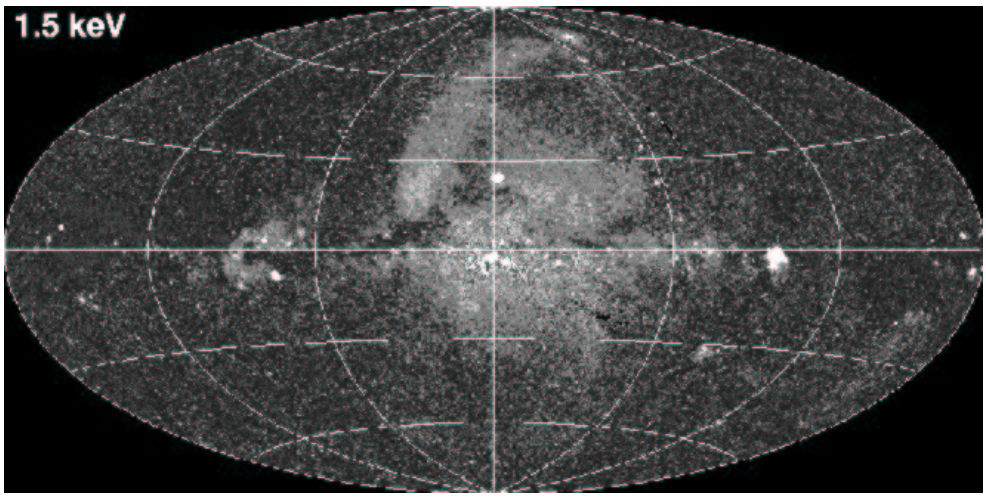

Fig. 14: *RASS sky map in the RC band energy range. The North Polar Spur and Vela are still visible. The remaining of the map is very isotropic. This is because more the 95% of the emission represented in this map is originated in the extragalactic X–ray background (see Sect. 1 and 5.3.4).*

called *exposure map* in Fig. 15. This dependency stems on the differences in the exposure length for different directions in the sky: about 40000 s for the ecliptic poles vs. about 300 s for the ecliptic equatorial regions, whereas shorter exposures yield higher uncertainty in the measured intensities. The RASS exposure maps will be of fundamental importance in Chap. 5 where they will be used to give statistical weights to the models for the SXRB discussed in this thesis.

Before producing the final maps of the SXRB, it is necessary to eliminate the contaminating effects from the raw observations. In this work, we will use the latest release of the maps of the RASS by Snowden et al. (1997). This choice guarantees the best point source rejection (all point sources down to a detection limit of $0.02\,\mathrm{cts\,s^{-1}}$ have been removed) and correction for unrelated diffuse X-ray emission produced by scattered solar X-rays (Snowden & Freyberg, 1993), long–term X-ray enhancements (Snowden et al., 1995) and the particle background (Plucinsky et al., 1993). After data reduction (see Freyberg (1994) for a more detailed description), the final angular resolution of the RASS release used in this work is $12'$. However, the correlation study of the RASS with an HI all-sky survey presented in Chap. 5 requires a regridding of the RASS to a $48'$ angular spacing grid in order to match the resolution of both grids. It is also important to note, that the experience gained in the data reduction for ROSAT has turned out to be of great importance for the development of data reduction methods for present X–ray telescopes (see Sects. 3.3 and 7 and also Charles & Seward (1995)).

From a first visual inspection of the results produced by the RASS, a remarkable difference in the distribution of the SXRB intensity for the different energy regimes is

obvious. While in the low energy regime (Fig. 12) the higher intensities are concentrated towards high Galactic latitudes and significantly structured, the distribution for the higher energy regimes is much more isotropic. This property is closely related to photoelectric absorption caused by the interstellar medium of the Milky Way, as already mentioned in Chap. 1. We will discuss this effect in more detail in Chaps. 4 and 5.

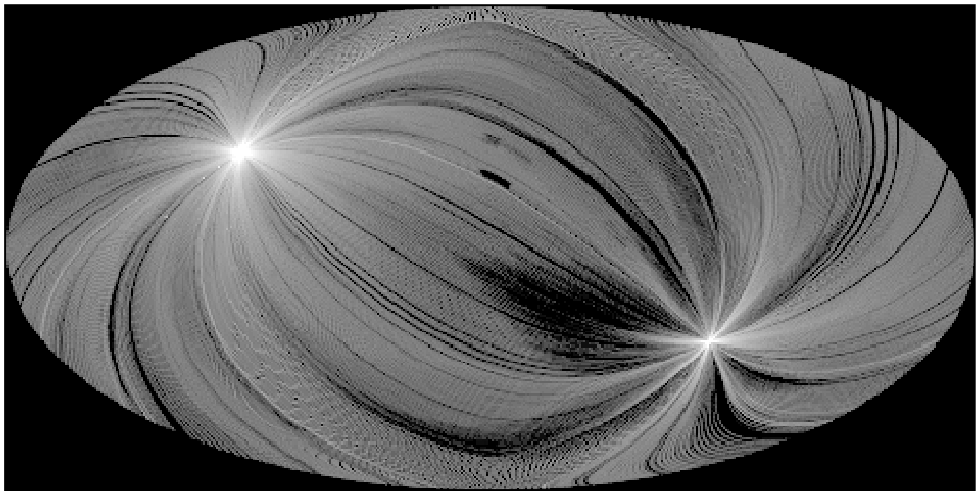

Fig. 15: *RASS exposure map in the same projection the Fig. 12. A logarithmic scale from 100 to 10000 s is used in the grey scale, where white means the longest exposure time. The two bright points correspond to the ecliptic poles. The structure in form of "stripes" is due to the specific scan strategy used for the observations.*

3.3 A Brief Description of a Modern X–ray Satellite: XMM–Newton

The European X–ray telescope XMM–Newton was launched by an Ariane 5 rocket in 1999 and it is still operational. XMM–Newton carries the X–ray mirror assembly with the largest collecting area to date (about four times that of ROSAT), making of it the most sensitive X–ray satellite in orbit. Since we will make extensive use of XMM–Newton observations in Sect. 7, we will outline the most important characteristics of this telescope here.

In Fig. 16 we can see that XMM–Newton is in fact composed of three co–aligned X–ray telescopes and one optical/UV monitor (OM). All telescopes have independent mirrors and can be operated separately. Also independent sets of filters (*thin, medium and thick*) are provided in order to avoid damage to the detectors in pointings with very bright sources in the FOV. The highly eccentric orbit of XMM–Newton, with perigee

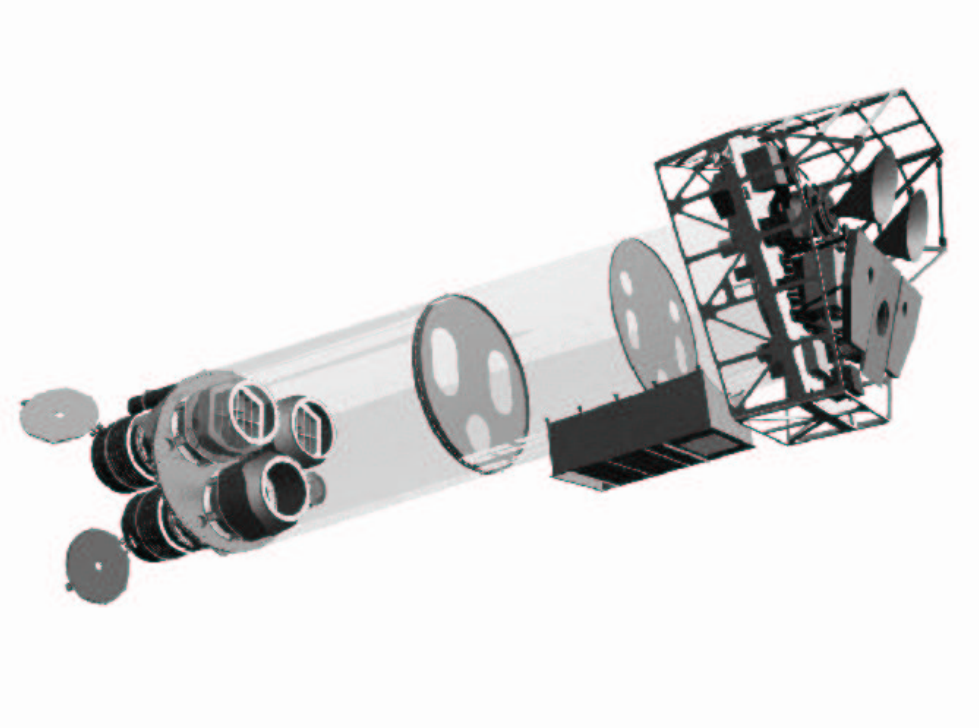

Fig. 16: *Sketch of the XMM-Newton payload. The mirror modules, two of which are equipped with Reflection Grating Arrays, are visible at the lower left. At the right end of the assembly, the focal X-ray instruments are shown: The EPIC MOS cameras with their radiators ("horns"), the radiator of the EPIC pn camera (below the MOS radiators and in the center) and those of the RGS detectors (left and right of the pn radiator). The OM telescope is hidden by the lower mirror module. The circles in the middle part represent The filters of the telescope are mounted in the central wheels. The focal length is 7.5 m. Image taken from the XMM–Newton Users' Handbook*

at $r \simeq 6000$ km and apogee at $r \simeq 150000$ km permits very long exposures without any interruption. For more details on the orbital parameters of XMM–Newton see the *XMM-Newton Science Operations Centre Home Page*[4].

3.3.1 XMM–Newton Mirrors

Each of the three X–ray mirror units of XMM–Newton is made of 58 nested *Wolter I* type mirrors. The 58 individual mirrors are placed in a concentric manner with distances between neighboring "layers" that vary from about 1 mm close to the optical axis to about 4 mm in the outer mirrors. The thickness of the mirrors also varies from 0.47 mm for the inner mirrors to 1.07 mm for the outer part. With a surface accuracy of

[4] *http://xmm.vilspa.esa.es/*

0.4 nm, the energy coverage of the mirrors is approximately $0.1\,\mathrm{keV} \leq E \leq 15.0\,\mathrm{keV}$. Note, that this energy range is significantly broader than that for ROSAT.

The accumulated effective area of the three mirrors is about $4500\,\mathrm{cm}^2$ at 1 keV and $1500\,\mathrm{cm}^2$ at 10 keV. The dependency of effective area on photon energy and off–axis angle of the XMM–Newton mirrors is shown in Fig. 17. However, the predictions for the *vignetting* in XMM–Newton, as shown in the right panel of Fig. 17, have some problems that will be discussed in detail in Sect. 7.3. In fact, deviations between the predictions and the measurements of the *in–flight* effect of vignetting have been reported by several authors (see, e.g. Lumb et al., 2002; Read & Ponman, 2003; Katayama et al., 2004).

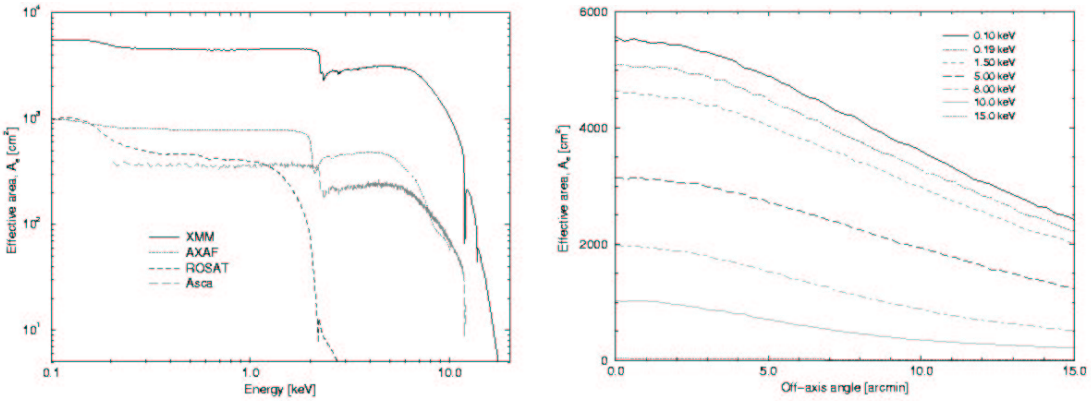

Fig. 17: **Left:** *The on–axis effective area vs. photon energy of all XMM–Newton mirror modules, in comparison with those of other X-ray satellites (logarithmic scale).* **Right:** *The total effective area of all XMM mirror modules, at a few selected energies, as a function of off–axis angle ($0'$-$15'$). Images taken from the XMM–Newton Users' Handbook*

Two of the X–ray mirror assemblies (upper mirrors in Fig. 16) are equipped with the so–called *Reflection Grating Assemblies* (RGA). These reflect about 50% of the photons passing through the respective mirrors onto linear arrays of 9 *charge–coupled devices* (CCDs), each of them situated outside the focal plane of the mirrors. The RGAs together with the sets of CCDs form the so–called *Reflection Grating Spectrometer* (RGS) on–board XMM–Newton. Basically, the CCDs take pictures of the X–rays diffracted in the respective RGAs resulting directly in high quality spectra of the sources. The spectral resolving power, $\frac{E}{\Delta E}$, varies from about 200 to 600 in the energy range covered by the RGS ($0.35\,\mathrm{keV} \leq E \leq 2.5\,\mathrm{keV}$). This is unsurpassed by any other X–ray detector in orbit. Also remarkable sensitivity is offered by the RGS, with a flux limit of $10^{-12}\,\mathrm{erg}\cdot\mathrm{cm}^{-2}\cdot\mathrm{s}^{-1}$ comparable, e.g., to that of the ROSAT Bright Source Catalog (Voges et al., 1999).

3.3.2 On–board X–ray Imaging Detectors

XMM–Newton carries two types of imaging detectors: the EPIC–MOS and the EPIC–pn cameras. In both cases, CCD technology is used for the detection of the X–ray events. The CCDs are capable of determining the energy of the detected photon, providing thus non–dispersive spectrographic information in addition to the imaging. The energy resolution of the MOS and pn cameras is almost identical corresponding to about 70 eV and 150 eV at the 1 KeV and 6.5 keV energy regimes respectively ($\frac{E}{\Delta E} \simeq 50$). Also both types of cameras can be operated in a variety of *modes* like, e.g., the *timing* or the *FullFrame* modes (higher time resolution for variability studies and use of the complete detector area, respectively). Sets of filters with different thicknesses are available for all cameras. A detailed description of all modes and filters can be found in the *XMM–Newton Users' Handbook*[5]. Now, we will outline the differences between these two types of detectors used on–board of XMM–Newton.

- **EPIC–MOS:** There are two cameras of this type in XMM–Newton (MOS1 and MOS2), both placed at the focal planes of the telescopes with the RGAs (upper telescopes in Fig. 16). Each MOS camera consists of 7 single CCDs, arranged as shown in the left panel of Fig. 18. Each single CCD consists of 600x600 pixels with an angular size corresponding to about $1\farcs1$ per pixel (about 40 μm in the focal plane). In order to minimize the effect of the gaps between the individual chips, MOS1 and MOS2 have been mounted perpendicularly. The operational bandpass is 0.15..12 keV, although the quantum efficiency decreases rapidly for energies above 4 keV (see Fig. 19). The angular resolution achieved with the MOS detectors and the corresponding mirrors is described by the *point spread function* (PSF) with a *full width at half maximum* (FWHM) of $6''$and *half energy width* (HEW) of $14''$at 1.5 keV. These values for the angular resolution are given for an on–axis position. They vary little in the 0.1-4 keV regime. For higher energy regimes, slight energy dependent variations are present (Jansen et al., 2001). A detailed description of the MOS cameras and its functioning is presented by Turner et al. (2001).

- **EPIC–pn:** The EPIC–pn detector consists of 12 CCD arranged as shown in Fig. 18. The pixel sizes are about $4\farcs1$. In contrast to the MOS cameras, pn is *back–illuminated* leading to significant differences in the quantum efficiencies of both types of detector (see Fig. 19). In fact, the bandpass of pn is broader than that of MOS, spanning form 0.15 to 15 keV. Also the sensitivity to low energy photons is significantly increased with respect to front–illuminated CCDs. The angular resolution, which is given mainly by the mirror quality, is basically the same than for MOS. The biggest advantage of pn arises form the temporal resolution: 0.03 ms in pn and 1.5 ms in MOS. This is achieved by the use of a different

[5] *http://xmm.vilspa.esa.es/external/xmm_user_support/documentation*

technique in the read–out phase of the CCD. While in MOS the photon events are read "conventionally", every single row of the pn CCDs has its own amplifier and can be read out individually. Further details on the pn camera are in Strüder et al. (2001).

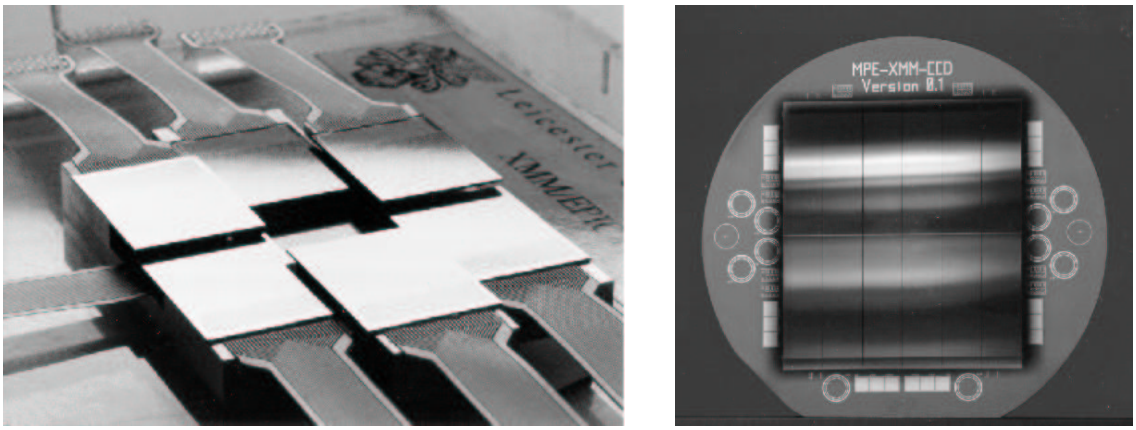

Fig. 18: **Left:** *Layout of the EPIC MOS cameras. These are composed of 7 individual CCD numerated as 1 in the center, 2 at the lower left and increasing anti–clockwise. The CCD have a small offset in their vertical positions (some mm) in order to match the slightly bended focal surface of the telescope.* **Right:** *Layout of the 12 CCDs composing the EPIC pn camera. EPIC pn is mounted in XMM–Newton such that the geometrical center of the camera is slightly displaced with respect of the optical axis of the mirror. This is to avoid that the gap between the central CCD coincides with the point of maximal effective area in the FOV.*

We would like to mention here that there is an intrinsic problem in using CDD detectors for X–rays: The detectors are also sensitive to optical light. In fact, there are quite efficient in the detection of optical photons, yielding in a high "optical contamination"originated in foreground stars. It is in order to overcome this problem that the EPIC instruments in XMM are equipped with a set of Al filters which absorb the optical emission of stars in the FOV. Which thickness has to be used is clearly defined by the magnitude of the stars in the FOV: The *thick* filter up to $m_{\rm V}$ of 1-4 (MOS) or $m_{\rm V}$ of 0-3 (pn), the *medium* filter up to $m_{\rm V}$ of 10 and the *thin* filters up to $m_{\rm V} \simeq 18$. The *open* position (without any filters) is not recommended in any case by the *XMM-Newton Science Operations Centre* (SOC).

Apart from the X–ray detectors, XMM–Newton also carries a small optical telescope called the *optical monitor* (OM) for simultaneous monitoring of optical and UV emission. The limiting magnitude of OM corresponds to about $m_{\rm V} \simeq 24$. The OM permits for example the study of optical counterparts of X–ray bursts form Galactic sources. This optical instrument will not be used in present work.

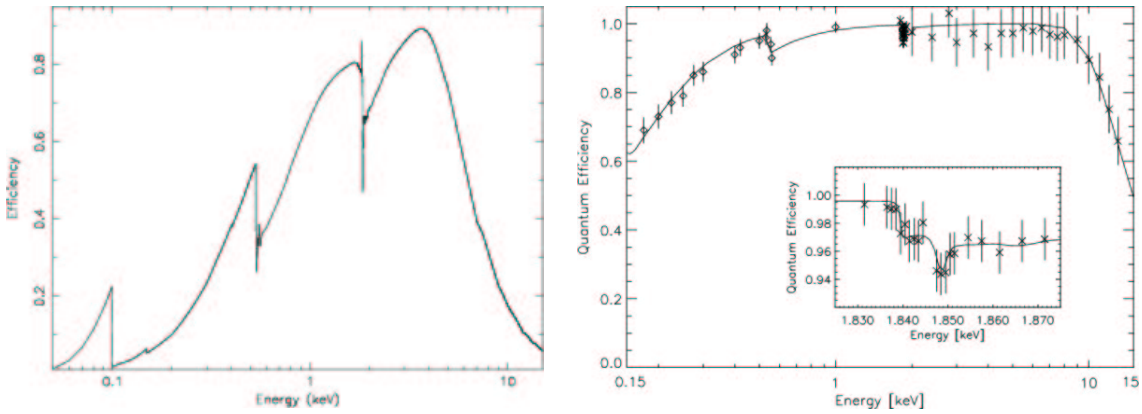

Fig. 19: **Left:** *The quantum efficiency of the EPIC MOS cameras from Turner et al. (2001).* **Right:** *The quantum efficiency of the EPIC pn from Strüder et al. (2001).*

3.3.3 Data Calibration

One of the main advantage of XMM–Newton with respect to other X–ray observatories is its great sensitivity. In principle, XMM is able to detect the fainter parts of extended objects (e.g. SNr or intra–cluster gas) of which only the core has been previously analyzed. But this capability can only be used together with appropriate data calibration and reduction methods which overwhelm the difficulties that arise in the analysis of such faint emission (with very low signal–to–noise ratio). Several authors (Lumb et al., 2002; Marty et al., 2003; Read & Ponman, 2003; Katayama et al., 2004) have addressed this problem for XMM–Newton demonstrating that some of the on–ground calibrations performed do not match with the in–flight performance of the observatory. In Chap. 7 we will deepen in some of these effects like the solar *proton flare filtering* and the correction for *vignetting*. Here, we outline the preliminary steps of reduction and calibration, in which the standard tools are reliable, and list the main contamination effects that have to be taken into account. For complete reports on calibration for the EPIC instruments see, e.g. Gondoin et al. (2000) and Ferrando et al. (2003).

After a successful pointing with XMM–Newton, the observer gets the data products in two different formats:

- **Observational data files** (ODF): The ODF contain the raw data obtained as measured by the detectors, i.e. they contain un-calibrated quantities on a chip-by-chip basis for the X-ray cameras and Optical Monitor. They also contain the telemetry of the observation. The file format used to provide the data is the FITS (flexible image transport system) format. The main advantage of this choice is that there are plenty of excellent packages to examine, modify or analyze FITS files, such as: the FTOOLS/LHEASOFT (FITS file manipulation), SPEX (spectral analysis) SAOIMAGE, SAOTNG or DS9 (image display and analysis).

- **Pipeline products** (PPS): A collection of validated, top-level scientific products including event and source lists, multi–wavelength images and cross-correlation products, generated at the Survey Science Center[6] (SSC). The standard calibration performed at the SSC is performed using the XMM–Newton Science Analysis System[7] software package (SAS). Unfortunately, the standard calibration, which is satisfactory for the investigation of strong point sources, is not adequate to investigate faint extended sources (see, e.g. Lumb et al., 2002; Marty et al., 2003). In Chap. 7, we will present newly developed methods to overcome this insufficiency in the SAS software. These methods will be based mainly in a combination of C program's and FTOOLS tasks.

The *Current Calibration Files* (CCF) included in the XMM–Newton Calibration Portal[8] contain all information necessary to calculate the PPS from the ODF. The CCF are frequently updated with the latest calibration status (e.g.: newest lists of damaged pixels) and, together with the SAS software package, they permit re–calibrating the observations with the improved calibration data at any time. Thus, maintaining the ODF for the user enables the investigation and/or correction of calibration errors which have been detected after the initial delivery of the PPS. The individual steps in the processing of the ODF to obtain the PPS that must be considered in a "manual" calibration of the XMM–Newton observations can be found in the *Calibration Access and Data Handbook*[9] and in the *ABC Guide to XMM–Newton Data Analysis*[10].

Before correcting the data for mirror or detector properties, it has to be taken into account that despite the electronic processing on–board the raw data still contain plenty of non–X–ray events related with, e.g. *badpixels*, the CCD edges (Marty et al., 2003) or photon *pile–up* (Ballet, 1999). The SAS tasks *emchain* (MOS) and *epchain* (pn) sort out most of these events. These tasks produce intermediate data which must be still corrected for mirror and detector properties to enable photometric or spectrographic investigations. In the following, we outline the most important effects that must be considered. We would like to note that the corrections are equivalent to those that had to be performed for ROSAT. Furthermore, the experience gained in the reduction of the ROSAT data has been fundamental in developing the specific XMM–Newton tools.

- **Backgrounds**: There are several types of background affecting the XMM–Newton observations. More details of each type can be found in, e.g. Lumb et al. (2002); Read & Ponman (2003); Marty et al. (2003). The most important are:

[6] *http://xmmssc-www.star.le.ac.uk/*
[7] *http://xmm.vilspa.esa.es/external/xmm_sw_cal/sas_frame.shtml*
[8] *http://xmm.vilspa.esa.es/external/xmm_sw_cal/calib/index.shtml*
[9] *http://xmm.vilspa.esa.es/external/xmm_sw_cal/calib/documentation.shtml#Genera*
[10] *http://heasarc.gsfc.nasa.gov/docs/xmm/abc*

Un–rejected cosmic rays (non–vignetted): Events associated to cosmic rays that have not been filtered by the on–board electronics. Non–vignetted means that this background is not affected by vignetting (see below) in its distribution. In other words, the cosmic rays responsible for these events are not focused by the mirrors and enter the detector from all directions.

Fluorescent emission lines (structured): Emission from the structure of the telescope. The most important lines are the Al K (at about 1.4 keV) line for MOS and the Cu K(at about 8 keV) line for pn. Since this background is related to the physical structures of the telescopes, its intensity distribution is highly structured in the FOV (see Fig. 20)

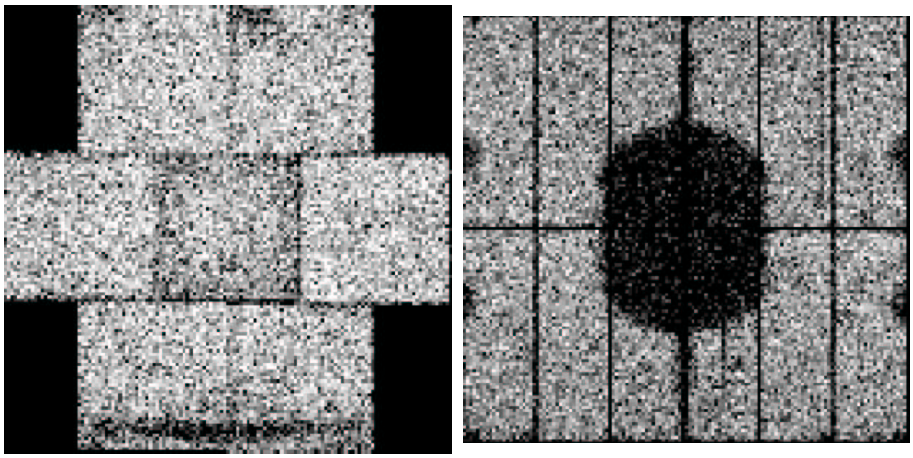

Fig. 20: **Left:** *Distribution of the Al K fluorescence line for the MOS cameras ($E \simeq 1.4$ keV). The gaps between the CCDs are clearly visible. Also the rim areas of the central CCD are significantly dimmer than those of the surrounding CCDs. These effects originate in the structure of the components of the telescope.* **Right:** *Distribution of the Cu K fluorescence line for the pn camera ($E \simeq 8$ keV). Again, significant structure is visible. Images taken from Lumb et al. (2002).*

Electronic noise (non–vignetted): For example, bright pixels or electronic overshoot problems near the read–out nodes of the pn pixel. Electronic noise is negligible for energies below 300 eV.

Solar soft protons (vignetted): This component dominates the periods of high background rates. It consists in a contamination by photon–like events which are thought to be originated from solar protons directly gathered and focused by the mirrors. There is actual debate on the "true" spectral distribution of the so–caller *solar proton flares* as well as on the appropriate methods to eliminate the contribution of this background to the data. We will go in detail in this topic in Sect. 7.2.2.

XRB (vignetted and structured): Already mentioned in Chap. 1, the XRB

is susceptible of being considered not a contamination but an useful signal to investigate the sky. We will do this extensively in Chaps. 5 and 6 using ROSAT data for the soft part of the background. Such systematic studies have not been done with XMM–Newton yet. This is probably because of the technical difficulties for the data reduction of such an investigation with XMM–Newton. In Chap. 7, we present new tools which have been developed to minimize the data calibration problems.

- **Mirror on–axis effective area** $A_{eff}(E)$: Decrease in effective area for increasing photon energy with absorption edges due to the coating of the mirrors (Au M–edges at $\simeq 2$ keV in Fig. 17). For a detailed on–ground investigation of this effect see Gondoin et al. (1998b).

- **Mirror vignetting** $V(\theta, E)$: Decrease in effective area for increasing off–axis angle θ (see right panel in Fig. 17). The vignetting function also varies with photon energy, with a higher slope in radial direction for higher E. Like in the case of $A_{eff}(E)$, vignetting origins in the grazing angle optics of the mirrors (Eq. 3). The vignetting function for a specific energy band and normalized to the exposure time of the observation is also called *exposure map*. These will be discussed in more detail in Chap. 7.

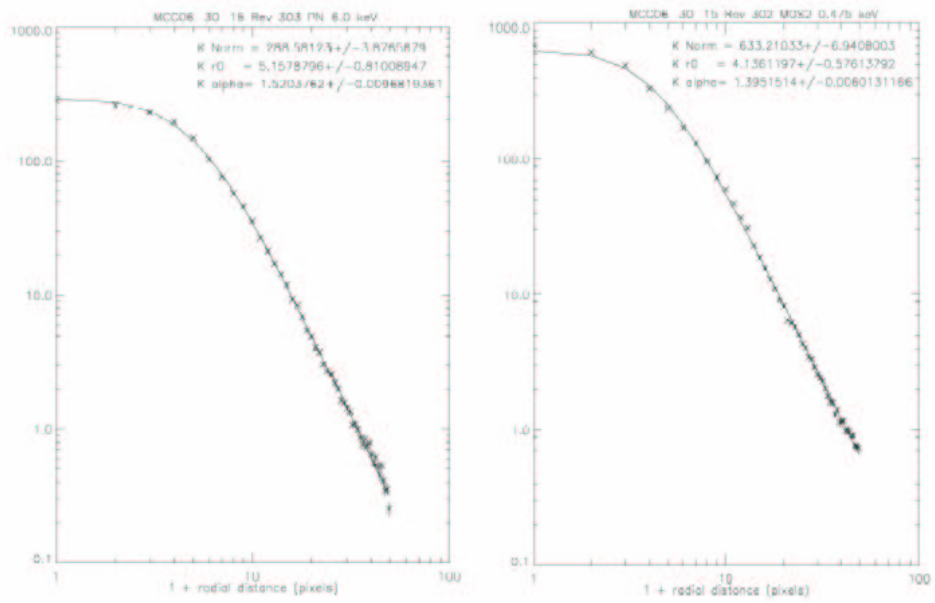

Fig. 21: *Surface brightness radial profiles of the PSF of the MOS2 camera at two different energy regimes: 6 keV to the left and 0.475 keV to the right. The crosses correspond to in–flight measurements realized with the Seyfert 1 galaxy MCG–06–30–15 and the solid lines show the fitted King profiles. Image taken from Kirsch (2004)*

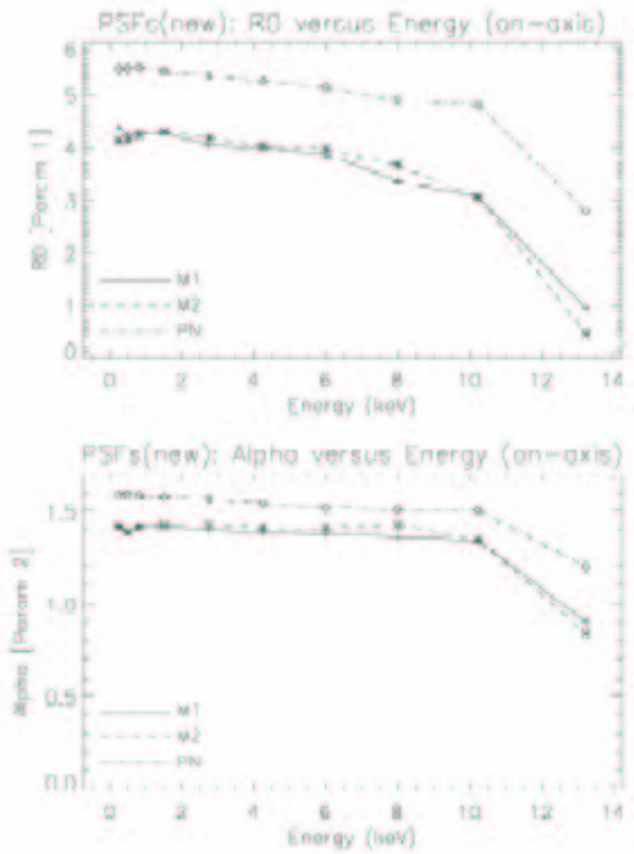

Fig. 22: r_0 *– Energy (top) and* α *– Energy dependencies for the on–axis PSF of the MOS1, MOS2 and pn cameras. Image taken from Kirsch (2004)*

- **Mirror point spread function** $PSF(\theta, E)$: Represents the *smearing* in the image of a point source caused mainly by diffraction and inaccuracies in the mirror surface. On–ground calibrations (Gondoin et al., 1998a) concluded that, although the "true" PSF has a very complex shape, its radial distribution is well fitted by a King profile (see Fig. 21):

$$PSF \propto \left[1 + \left(\frac{r}{r_0}\right)^2\right]^{-\alpha} \tag{5}$$

where r is the radial distance to the center of the source in the image plane. The two parameters r_0 and α can be used to infer the FWHM and the HEW. These (r_0 and α) were found to depend linearly on θ and E. In–flight calibrations with appropriate sources (Lumb et al., 2000) corrected the on–ground results in that the parameters are kept almost constant up to about 8 keV and steepen only for higher energies (see Fig. 22). Of special importance for the source detection

routines is the broadening of the HEW, i.e. of the angular resolution, with off–axis angle (up to a factor of two in the 1.5 keV regime (Gondoin et al., 1998a).

- **Filter transmission** $FT(E)$: Chromatic correction to the measured fluxes which takes into account the absorption corresponding to the thickness of the filter used in the observation. Since low energies are more efficiently absorbed (see also Sect. 4.2), the presence of a filter yields a *hardening* of the observed spectrum.

- **Detector quantum efficiency** $QE(E)$: Not all X–ray photons which go through the mirror and filter are detected by the cameras. There are many ways of losing the signal like, e.g., very energetic photons which cross the CCD without depositing their energy, i.e. low cross section of the detector for high energies. The quantum efficiency of the imaging detectors in XMM–Newton is shown in Fig. 19. Note that in both cases of $FT(E)$ and $QE(E)$ homogeneity has been assumed. In other words, it has been assumed that they are not a function of θ or, more generalized, of x,y (detector coordinates). In the latest status report of the XMM–Newton calibration (Kirsch, 2004), we can find that this assumption might not be completely correct for the QE in the lowest energies $E \leq 0.4$keV (see Fig. 23). However, the errors introduced by neglecting the inhomogeneities would be only marginal and are not taken into account by the SAS. In Chap. 7, we will address this topic in more detail.

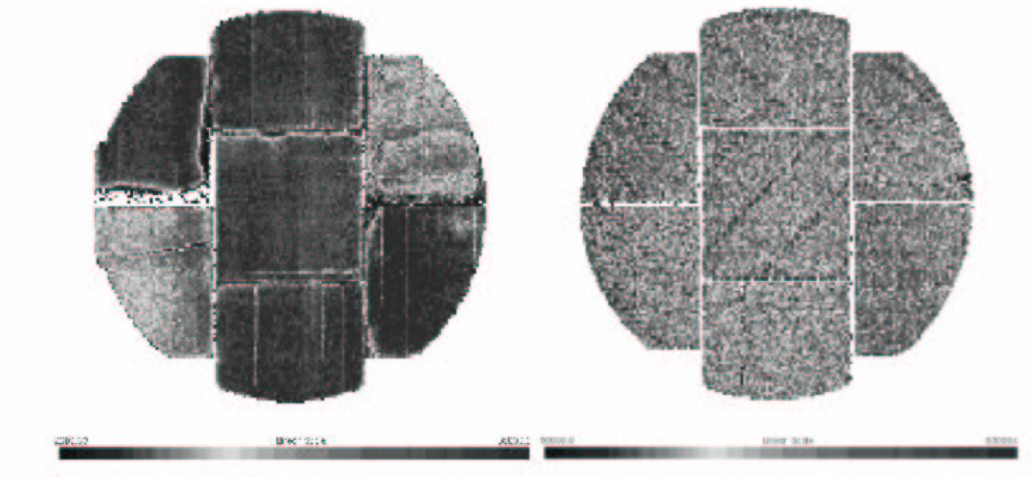

Fig. 23: **Left:** *Distribution of the QE of the MOS1 camera at 150 eV. CCD2 and CCD5 (upper–left and bottom–right) present a lower value than the remaining CCDs. This effect is not taken into account by the SAS calibration tools.* **Right:** *Distribution of the QE of the MOS1 camera at 400 eV. At this energy regime, the inhomogeneities in the left panel are almost completely vanished. Images taken from Kirsch (2004)*

- **Detector redistribution matrix** $RMF(C,E)$: The RMF relates the count rates measured in the instrumental energy channels (C) with the actual flux of the source at energy E. In practice, the incoming photons with energy E will not always be detected in the instrumental channel exactly corresponding to the photon energy but redistributed among the neighboring channels. For example, the so–called *Charge Transfer Inefficiency* (CTI) consists in a loss of charge during the transfer from the detection pixels to the electronic read–out node of the CCD, resulting in a shift to lower energies and a broadening of the lines (Ferrando et al., 2003). Note that the CTI is also relevant for the calculation of the detector quantum efficiency. The RMF is rather complex even for monochromatic beams (see Fig. 24). Also the $FT(E)$ and the $QE(E)$ must be considered to construct reliable models of the RMF. Such models are available in the CCF.

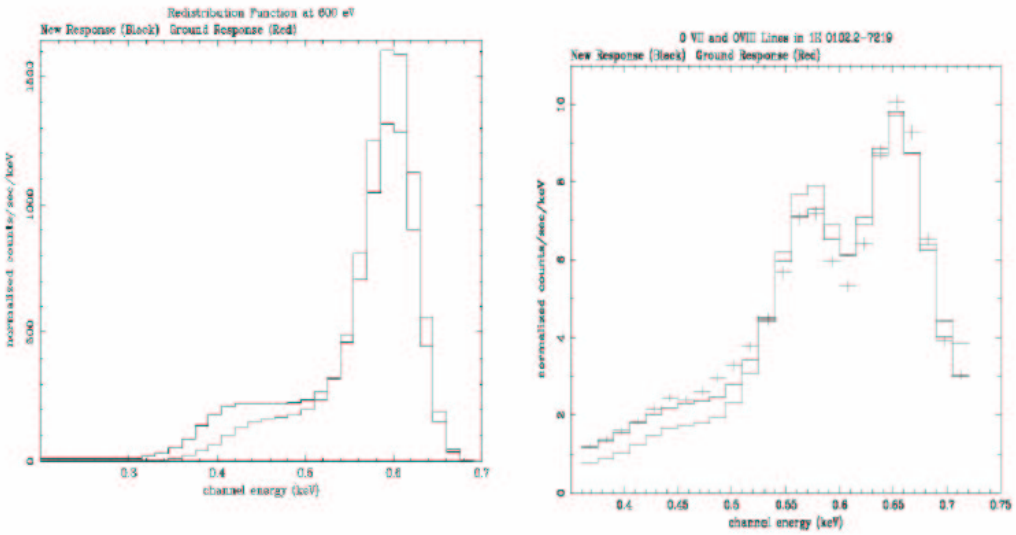

Fig. 24: **Left:** *Redistribution function of the EPIC MOS detectors for a monochromatic source at 600 eV. The grey line corresponds to the on–ground determination of the RMF and the black line corresponds the in–flight best fit to a source. Note the difference in the "shoulder" at the low energies.* **Right:** *Measured spectrum (crosses) and best fit (black line) of a source with strong emission lines (SNR 1E0102.2-7219) compared to the on–ground predictions (grey line). Images taken from Ferrando et al. (2003)*

We can summarize the corrections that have to be performed, after subtracting the background contributions, for imaging or for photometric investigations in the following simplified formula:

$$I(x,y,E) = A_{eff}(E) \cdot QE(E) \cdot FT(E) \cdot V(\theta(x,y),E) \cdot PSF_{x,y}(\theta(x,y),E) * O(x,y,E) \quad (6)$$

where the count rate at position x,y of the detector and energy E ($I(x,y,E)$) is given by the convolution of the "real" flux arriving at the mirrors ($O(x,y,E)$) with the *instrumental response*. The image quality is given mainly by $PSF_{x,y}(\theta(x,y),E)$, where the sub–indices indicate the variation on the parameters of the PSF with position in the camera. Concretely, the core of the King profiles varies little with θ, but the wings are significantly broadened towards the edges of the field of view yielding higher values for the HEW. We can clearly see this effect in the right panel of Fig. 1, where sources close to the edges of the FOV are "smeared" in a larger area.

For non–dispersive spectroscopic investigations with the EPIC cameras, we can write:

$$I(C) = \int RMF(C,E) \cdot S(E) dE \tag{7}$$

where $I(C)$ represents the events measured in channel C and $S(E)$ the spectrum of the source. Note that Eq. 7 and Eq. 6 can not be applied directly since, with the real data, discrete operations must be used. Furthermore, the term $S(E)$ in Eq. 7 must be corrected for the effects of Eq. 6 that are involved in flux determinations.

Because of the absence of cosmic X–ray sources which can be used as in–flight calibration standards, models for all calibration functions involved in Eqs. 6 and 7 were obtained during extensive on–ground campaigns. Unfortunately, the on–ground testing could not be done in fully representative conditions. For example, the tests for the mirror properties performed at the Panter facility (Gondoin et al., 1996) had the problem that the artificial sources were located only in the near field of the mirrors (in contrast to astronomical sources). Furthermore, not all energies could be tested. The CCDs were tested at the Orsay Synchrotron Facility (Pigot et al., 1999).

Several in–flight calibration campaigns (see, e.g. Lumb et al., 2000; Gondoin et al., 2000; Lumb et al., 2003) have been dedicated to check the validity of the on–ground models. Most of the results have been validated and found to be applicable in practically all camera modes (see, e.g. Ferrando et al., 2003, for A_{eff} and RMF). In–flight vignetting is still a matter of debate in the present that will be discussed in Chap 7.

4 The Interstellar Medium: The X–ray/Radio Connection

The space between the stars of a galaxy is not empty. It is filled with material in a large variety of states, from neutral and cold atoms to very hot and highly or even fully ionized matter. All this material is covered with the notion of interstellar medium (ISM), which will be the main actor of this work.

A connection between the ISM and the X–ray radiation is clear by considering that it is the hot ionized gas in the ISM of the Milky Way that is responsible for most of the emission of the SXRB up to 1 keV (see, e.g., Kerp, 1994; Herbstmeier et al., 1995; Pietz, 1997; Kuntz & Snowden, 2000). Furthermore, the X–ray emission of such hot plasmas –halos and bubbles– has also been detected in external galaxies (see Fig. 3). For such a emission, temperatures above 10^6K are necessary (see Sect. 2.2.1).The elements in the gas are partly or even totally ionized. Some general characteristics of this (and other) phases of the ISM will be given in Sect. 4.1.

But before arriving at the observer's position, the intensity of the X–ray emission is modulated by the photoelectric absorption caused by the neutral and partly ionized fraction of the ISM. The quantification of this attenuation effect for the case of the Milky Way will be discussed in Chap. 5 as the scientific focus of this thesis. In Sect. 4.2, we will introduce the physical concepts involved in the radiative transfer of the soft X–ray through the ISM. The goal is to establish the "qualitative" connection between the SXRB and the Galactic HI distribution.

4.1 The Phases of the ISM

The physical conditions of the ISM are controlled by several heating and cooling mechanisms. Radiation field from stars, SNe, stellar winds and cosmic rays are the main contributors to heating, while cooling is performed mainly by line emission from metals (see Wolfire et al., 1995). Then, at a given pressure, thermal equilibrium can be only achieved under certain combinations of the ionization parameter Ξ and temperature T of the ISM. Not all ranges for the two parameters are stable (see Fig. 25) and the ISM is separated into phases.

Theoretical models for the ISM have been developed (see, e.g. Field et al., 1969; Mebold, 1972; McKee & Ostriker, 1977) going into deep detail in diverse topics like

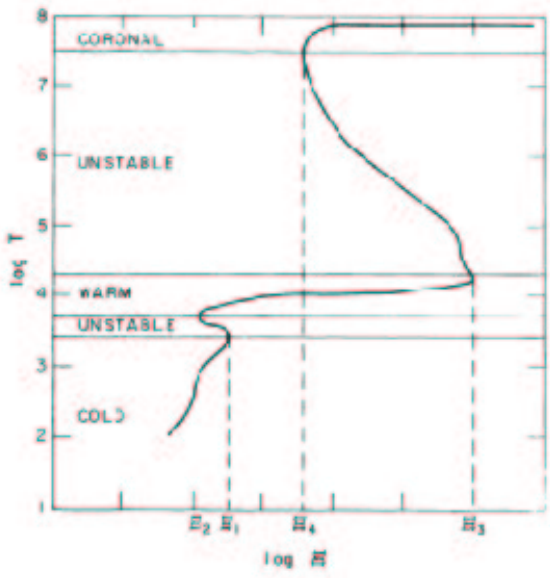

Fig. 25: *Phase diagram of the ISM as a function of ionization parameter* Ξ *and temperature* T *at a fixed pressure* $nT = 10^8\,\mathrm{K\,cm^{-3}}$*. There are some unstable regions (with negative slope) that make the ISM break up into different phases. Here, three of them are represented and noted as* cold*,* warm *and* coronal *according to increasing temperature of the material. Image from Lepp et al. (1985).*

cloud formation and stability or metal distributions. Also numerical models (see, e.g. Kalberla, 2003) have been fitted to observations, taking into account the fundamental contribution of the Dark Matter Halo. Here, we focus on the general characteristics of each phase (see also Tab. 3).

4.1.1 The Molecular Medium

Extreme column densities ($N_{\mathrm{HI}} \gg 1 \cdot 10^{21}\,\mathrm{cm^{-2}}$) characterize the molecular medium (MM). The high column densities enable that even at temperatures below 20 K molecules are formed from the atoms of the ISM. Densities in the order of 10^{10} cm^{-3} are reached. The most abundant molecule is H_2 but more complex molecules are also present.

H_2 is very difficult to be observed directly because it lacks a permanent dipole moment. The H_2 column density can be estimated through measurements of the second most abundant molecule: CO. Already with densities of 100 cm^{-3} and temperature 5 K, CO is collisionally excited by the H_2 molecules and emits discrete lines corresponding to rotational transitions. The practical conversion between the column densities of both molecules (H_2 and CO) is still a matter of debate at the present.

The MM is concentrated very close to the Galactic Plane with $|z| \leq 70$ pc (Bloemen,

Tab. 3: *Properties of the phases of the ISM in the Milky Way. Approximate values are given for: n mid–plane volume density at the position of the Sun, T temperature and h height scale. Values taken from Kalberla (2003).*

	MM	CNM	WNM	WIM	HIM
n [cm]$^{-3}$	0.66	0.30	0.10	0.024	10^{-3}
T [K]	≤ 20	100	5000	8000	$\geq 10^6$
h [kpc]	0.075	0.150	0.400	0.950	4.02

1987). Some exceptions are given in the form of individual clouds at medium or high Galactic latitude like the so–called Draco cloud (see Lilienthal et al., 1991), or cloud complexes associated to star forming regions in the spiral arms of the Galaxy (Efremov, 1989).

4.1.2 The Cold Neutral Medium

The notion of cold neutral medium (CNM) covers the interstellar material in neutral phase with temperatures up to some hundreds K. The most abundant element is HI. In the densest regions molecules like H_2, CO or even ammoniac ($n \geq 10^4$ cm^{-3}) can form.

The distribution of the CNM can be studied with observations of the 21 cm–line emission. A photon with this wavelength is emitted in the transition of a hydrogen atom where the directions of the spins of the proton and of the electron change from parallel to anti–parallel.

Most of the material of the CNM is concentrated in the region within 400 pc of the Galactic Plane. However, 20 % of the mass is located above this limit (See, e.g. Lockman, 1984; Lockman et al., 1984; Dickey & Lockman, 1990). The CNM forms cloud–like structures that remember the cirrus at the Earth's atmosphere. Typical diameters of 5 pc at $T \simeq 80K$ and density 20 cm^{-3} yield a mass of about $30M_\odot$ (Unsöld & Baschek, 1988). Some individual clouds present a molecular component but with no complex molecules. Filamentary structures are also present, as can be seen in Fig. 30 in Chap. 5.

The radio observations of the 21 cm–line provide information on the column density of the material and on the radial velocity of the material respective to the observer. Unfortunately, no information is provided on the distance to the material. All these will be of fundamental importance for our investigation of the SXRB in Chap. 5. This is because the distance to the individual clouds determines whether they produce a "shadow" in the intensity of the SXRB that must be taken into account in the models that we construct.

Finally, it is important to note the existence of the so–called *high-* and *intermediate–velocity clouds* (HVC, IVC). These are clouds whose radial velocity differs in a significant value from that given by Galactic rotation. Commonly, HVC are defined to have a velocity discrepancy $|v_{\mathrm{LSR}}| \geq 100\,\mathrm{km\,s^{-1}}$. IVCs and HVCs cover about 40% of the sky (Lockman, 1999). The HVCs are grouped in the so–called HVC complexes like, e.g., A, C and M (see Fig. 26).

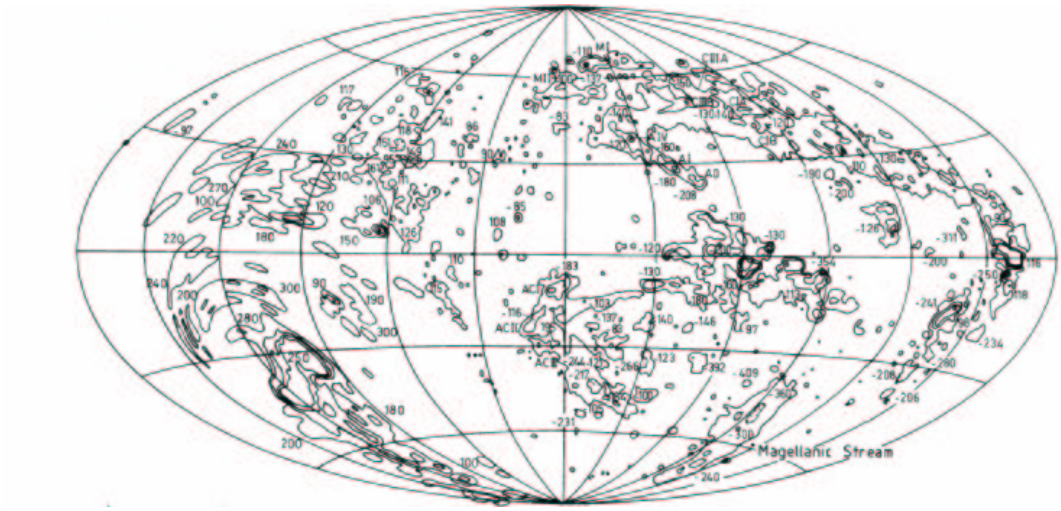

Fig. 26: *Total column density map for the HVC complexes in Aitoff projection (Galactic Anti–center at the center of the map). The contours correspond to column density levels of* $2 \cdot 10^{18}, 5 \cdot 10^{18}, 5 \cdot 10^{19}$ and $10^{20}\,\mathrm{cm^{-2}}$. *Complexes A, M and C are marked as the most prominent structures in the northern hemisphere. Image from Wakker (1991).*

The origin and evolution of the IVC and HVC is not well understood. Some models suggest that the HVC originate in a Galactic "fountain" or in material that is being accreted by the Milky Way (see reviews in Wakker, 1991; Wakker & van Woerden, 1991, 1997). Another possibility is that the HVC are the "missing" satellite galaxies of the Milky Way predicted by galaxy formation models. In this case, HVC should be also found around other galaxies (Westmeier et al., in prep, in the case of M31). One additional problem is the difficulty to find the distance to the HVC. This has been done for discrete directions where appropriate sources (usually suited background stars) with known distances are given. In this situation, it is possible to search for presence or absence of absorption lines corresponding to the gas of the cloud in the spectrum of the star, allowing to give constraints to the distance to the cloud. Woerden et al. (1999) compile the results of this kind of investigations for most of the IVC and HVC complexes (see Tab 4). In Chap. 5, we will propose a method to give constraints to the distance to the HVC complexes on a larger scale.

Tab. 4: *Approximate galactic coordinates of the center and mean radial velocities with respect to the local standard of rest for the HVC complexes listed in the left column. Also the constraints for the distance, height above the Galactic Plane and mass found in the literature are shown. Values from Wakker & van Woerden (1991, 1997); Woerden et al. (1999).*

HVC name	Center coordinates		d	$\|z\|$	v_{LSR}	$\log\left(\frac{M_{\mathrm{HI}}}{M_{\odot}}\right)$
	$l\,[^{\circ}]$	$b\,[^{\circ}]$	[kpc]	[kpc]	$[\mathrm{km}\cdot\mathrm{s}^{-1}]$	
A	150	30	$4-10$	$2.5-7$	-160	$5-6$
C	90	40	≥ 5	≥ 3.5	-120	≥ 6
M	180	60	≤ 4	≤ 3.5	-110	≤ 4.4

4.1.3 The Warm Neutral Medium

Also detected with the 21 cm–line emission, the warm neutral medium (WNM) differs substantially from the CNM. The material of the WNM has a temperature of several thousand K as deduced from the high velocity dispersion of the 21 cm–line emitted by this phase of the ISM. A further fundamental difference is the diffuse nature of the WNM, in contrast to the clouds formed in the MM and the CNM. This is crucial to determine the instrumental techniques that must be used to observe the WNM: single dish radio telescopes are the choice, instead of interferometers which are not sensitive to diffuse emission

In rough numbers, the column density of the WNM varies in the range $4\cdot 10^{19}\,\mathrm{cm}^{-2} \leq N_{\mathrm{HI}} \leq 4\cdot 10^{20}\,\mathrm{cm}^{-2}$ with generally higher values in the southern Galactic sky. The WNM is detected along all lines of sight.

For our study of the SXRB, the WNM plays a fundamental role because it is a makes fundamental contribution to the photoelectric absorption caused by the ISM in the soft X–rays (see Sects. 4.2 and 5.2). In rough numbers, the range in column density for the WNM corresponds to opacities $0.7 \leq \tau \leq 4$ in the energy regime below 1 keV.

In this work, we will use a new all–sky survey of the 21 cm–line to trace the photoelectric absorption in the SXRB: The Leiden/Dwingeloo/Argentinian Institute of Radioastronomy/University of Bonn survey (Hartmann & Burton (1997); Arnal et al. (2000) and Kalberla et al., in prep). This survey, presented in Sect. 5.1.2 (upper panel of Fig. 30), traces both the CNM and WNM and will be used to calculate the attenuation of the soft X–rays form distant sources when they cross the ISM in Sect. 5.2.1.

4.1.4 The Warm Ionized Medium

The most abundant element of the warm ionized medium (WIM) is ionized hydrogen HII. With a temperature about 10000 K, other elements are also ionized. The WIM is concentrated in a layer, the "Reynolds layer" (Reynolds, 1990), with a scale heigh of about 1 - 1.5 kpc from the Galactic Plane. The structure of the WIM can be best studied by means of the H_α line, in the optical part of the spectrum. There is a survey of this line for the northern sky, but no all–sky survey is available in the present. In the results of the *Wisconsin H_α mapper* (Haffner et al., 2003), rich filamentary structure is observed in high Galactic latitudes. This is in addition to a diffuse component that is exponentially distributed (Reynolds, 1990).

In advance to the next Sect., we have to note that the contribution of the WIM to photoelectric absorption can amount up to some 30% in the north Galactic hemisphere and to 15 % in the south. Furthermore, Kappes et al. (2003) proposes that this contribution could be even of 40% for the extreme case of the Lockman window.

4.1.5 The Hot Ionized Medium

The existence of the also called coronal phase was already postulated by Spitzer (1956). In that work, the hot ionized medium (HIM) was necessary to stabilize neutral clouds that had been observed at high Galactic latitudes. With a scale heigh of about 4.4 kpc (Kalberla, 2003), the HIM is the phase of the ISM that extends further away from the Galactic Plane. It has been detected in X–ray and UV investigations and can be observed in all directions it the sky. With a temperature in the million K regime, the bulk of the emission of the HIM occurs in the soft X–ray regime, approximately from 0.1 to 1 keV. Thus, the HIM is responsible from about 50% of the diffuse emission observed in the RASS in bands RC and RM (Figs. 12 and 13).

As already mentioned in Chap. 1, the distribution and temperature of the X–ray halo of the Milky Way are still a matter of debate in the present. Kuntz & Snowden (2000) propose a two layer distribution with different temperatures for each layer. The distribution in intensity would be patchy. A smooth isothermal halo is presented by Pietz et al. (1998). In this work, we will test both models and compare the distribution of the X–ray gas in the Milky Way with that corresponding to the gravitational potential obtained with models for the Galactic Dark Matter Halo (Kalberla, 2003).

4.2 Photoelectric Absorption in the Soft X–ray Regime

Before the X–ray photons, emitted by a distant source, arrive at the detector, they must travel through the ISM and are attenuated by the material. Photoelectric absorption, in

which an atom is ionized by the absorption of a photon with sufficient energy, is the most important attenuation process in the soft X–ray regime (Gorenstein, 1974).

In order to calculate the absorption caused on the X–ray emission by a certain material, it is necessary to know the quantity of the material as well as its *cross section*. The cross section is proportional to the atomic number, but also depends on the energy of the photon involved. Because the cross section presents a energy dependency of the form E^{-3} (Wilms et al., 2000), photoelectric absorption produces a hardening in the observed spectrum of a source in comparison to the "real" emitted spectrum (see Fig 27). In other words, hard X–rays are not so efficiently absorbed as soft X–rays.

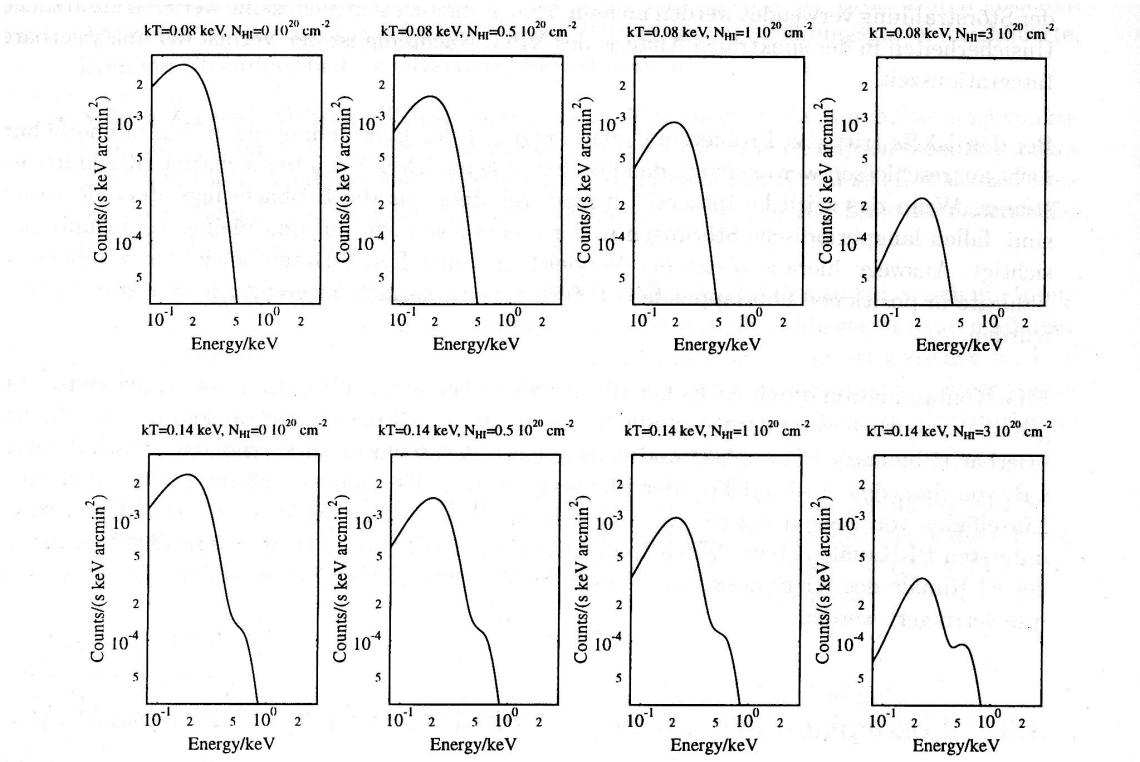

Fig. 27: *Effect of photoelectric absorption in the ROSAT spectra of two optically thin plasmas with different temperatures ($T \simeq 0.9 \cdot 10^6$ K upper and $T \simeq 1.6 \cdot 10^6$ K lower). The absorbing column density increases to the right as indicated. Larger column densities result in a clear hardening of the spectrum (the peak emission is displaced towards higher energies).The discrete emission lines, proper of plasmas with the temperatures presented here, vanish due to the rough spectral resolution of the instrument (smoothing by folding with the instrumental transmission function). Image taken from Pietz (1997).*

Since the cross section also depends on the atomic number of the elements involved in the absorption, some assumptions on the abundances of the Galactic ISM have to

be made. We will use the cross sections calculated for solar abundances by Morrison & McCammon (1983) shown in Fig. 28. The use of this set of cross sections requires knowledge only of the HI column density. Note that this does not mean that HI is the main contributor to absorption. In practice, the HI is used to trace the remaining elements and thus calculate the cross section of the ISM. In their work Morrison & McCammon (1983) also state that: *The effects of abundance enhancements, dust grains, molecules and ionization states are either too small or too uncertain to be useful for general applications.*

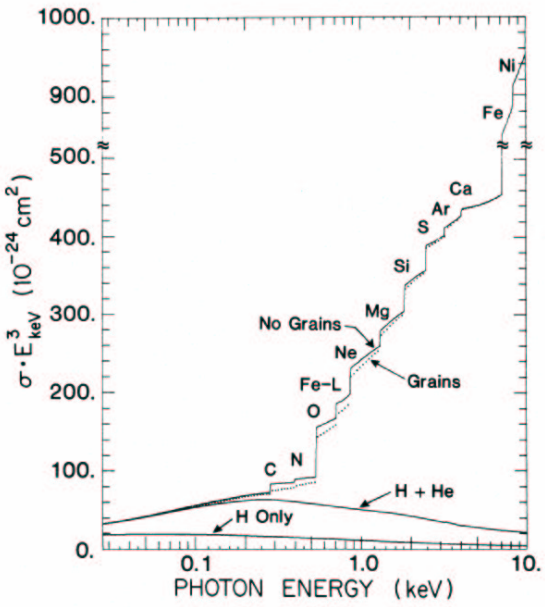

Fig. 28: *Net photoelectric absorption cross section per hydrogen atom as a function of energy, scaled by* $(E/1\text{keV})^3$ *from Morrison & McCammon (1983). The solid line corresponds to solar metalicity with all elements in the gas phases and in the neutral atomic form. The relative contributions of the different elements are also shown. In the regime up to about* 0.5keV*, He is the dominant absorber.*

4.3 The Effective Photoelectric Absorption Cross Section for ROSAT

ROSAT measured the XRB intensity distribution in the rather broad energy bands R1 to R7 (Snowden et al., 1995). Under these conditions, the cross sections for individual photon energies by Morrison & McCammon (1983) cannot be used directly and have to be averaged for a cross section accounting for the instrumental response at the corresponding energy bands. This leads to define the so-called *effective photoelectric*

absorption cross section $\sigma(N_{\rm HI})$, which represents an X-ray band–averaged photoelectric absorption cross section. $\sigma(N_{\rm HI})$ is defined as:

$$\sigma(N_{\rm HI}) = -\frac{1}{N_{\rm HI}} \ln \left\{ \frac{\int S(E) \cdot R(E) \cdot \mathrm{e}^{-\sigma'(E) \cdot N_{\rm HI}} \cdot \mathrm{dE}}{\int S(E) \cdot \mathrm{e}^{-\sigma'(E) \cdot N_{\rm HI}} \cdot \mathrm{dE}} \right\} \tag{8}$$

Here $R(E)$ denotes the telescope and detector response function, $\sigma'(E)$ the Morrison & McCammon (1983) photoelectric cross section, $N_{\rm HI}$ the observed HI column density and $S(E)$ the spectrum of the X-ray source (for details see Kerp et al. (1999)). Because of $S(E)$ in Eq. 8 we need some *initial guess* on the spectrum of the source in order to calculate the effective photoelectric absorption cross section. In the context of our study of the SXRB (Chap. 5), this yields a dependence of $\sigma(N_{\rm HI})$ on the temperatures of the LHB and the Galactic X-ray Halo which are not determined *a priori* but are free parameters in the models that we fit to the observations (see Sect. 5.3.3). In the case of the extragalactic X-ray background, the photon index describing its power law spectrum is independently determined and accordingly a fixed parameter (Hasinger et al., 2001).

To summarize, a quantification of the photoelectric absorption by the ISM for the ROSAT broad energy bands involves not only $N_{\rm HI}$ but also some assumptions on the spectrum of the observed source as can be seen in the example shown in Fig. 29 for the ROSAT RC band.

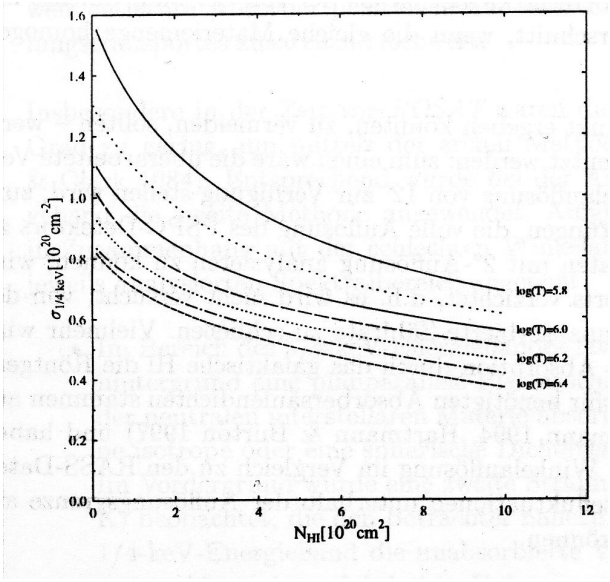

Fig. 29: *Effective cross section (Eq 8) for the ROSAT RC band as a function of* $N_{\rm HI}$*. The spectrum of the source has been modeled by MeKal plasma models with the marked temperatures. Image from Pietz (1997).*

5 Correlation of the SXRB and the HI Emission

In this chapter we will quantify the correlation between the SXRB and the Galactic absorbing HI column density. This will allow the construction of precise models of the diffuse X–ray emission and attenuation which can be used on one hand to investigate the properties of the Galactic X–ray Halo (this Chap.) and, on the other hand, to search for very faint signals in the RASS that cannot be detected without a total background subtraction (next Chap.).

As mentioned in Sect. 1, the origin of the SXRB has been investigated and today there is a general agreement that we can distinguish at least two sources of diffuse X–ray emission: Galactic (Snowden et al., 1991; Herbstmeier et al., 1995; Kerp et al., 1996; Pietz et al., 1998) and extragalactic emission (Hasinger et al., 2001). The Galactic component can be considered to be subdivided into the Galactic X–ray Halo and a local component (McCammon & Sanders, 1990), frequently called Local Hot Bubble (LHB). It is evident that all these components must be considered in our analysis. Here, we also focus for the first time on the **entire** HI sky and across the **full ROSAT energy window** ($0.1\,\mathrm{keV} \leq \mathrm{E} \leq 2.1\,\mathrm{keV}$).

The work in the present chapter is based in a manuscript submitted to Astronomy and Astrophysics by Pradas, Kerp & Kalberla, where one of the main scientific topics is to make use of the newest and best quality data available in order to distinguish which type of the actual models for the Galactic X–ray Halo fits better the ROSAT observations. In a rough separation of the possible scenarios, we have:

- A single temperature and smooth plasma distribution (Kerp et al., 1999; Pietz et al., 1998). In other words, an isothermal X–ray halo plasma in thermal equilibrium conditions. The shape of the X–ray Halo is defined by the gravitational potential of the Dark Matter Halo of the Milky Way (see Sect. 5.4.1).
- One plasma component with a smooth gradient in temperature, which increases towards the Galactic Center (Almy et al., 2000),
- A multi–temperature and patchy intensity distribution (Kuntz & Snowden, 2000; Snowden et al., 1998), where, in general, each direction on the sky could have a different temperature and emissivity. More concretely, in Kuntz & Snowden (2000) we find: *... the data are sufficient to characterize only two components, thought a greater number may exist, and the temperature of this components may vary with position.*

In the first case, neutral atomic hydrogen located in front of the Galactic X-ray Halo emission attenuates the X-ray emission and allows the quantitative modeling of the radiative transfer. The second approach is very similar to the first one at high Galactic latitudes, where the gradient in temperature is negligible (see Fig. 5 in Almy et al. (2000) and Sect. 5.3.7). In the last case, we do not expect to find any detailed quantitative correlation between X-rays and $N_{\rm HI}$, in particular not on angular scales of tens of degrees. Earlier results by Kerp et al. (1996); Pietz et al. (1998); Kerp et al. (1999) indicate that the soft X-ray radiative transfer can be evaluated across the whole sky and point to the single temperature plasma solution.

To perform our analysis of the SXRB, we correlate the ROSAT all–sky survey with the combined Leiden/Dwingeloo (Hartmann & Burton, 1997) and Argentinian (Arnal et al., 2000) HI 21 cm–line surveys. The combined HI 21 cm–line surveys form the first all–sky stray–radiation corrected survey and with the highest angular and velocity resolution available (Kalberla et al., in prep.). Neutral hydrogen is used as *the* quantitative tracer of the total photoelectric absorption produced by the ISM (see Sect. 4.2). Additionally, and once reliable models for the Galactic X–ray Halo have been derived, the Doppler–velocity information of the HI radiation will be used as a tool to discriminate between local and more distant clouds like the intermediate– and high–velocity clouds (see Sect. 6.1). Searching for soft X-ray shadows of individual clouds will allow us to test this 3–D hypothesis if we supplement the radial velocity criterion with lower and upper distance limits derived from stellar absorption line studies (see Fig. 4 and Wakker et al., 2003). It is important to note that we have to focus on the high latitude sky ($|b| \geq 25^\circ$), where the ISM is sufficiently transparent to permit soft X-rays originating in the Milky Way Halo and beyond to reach the solar neighborhood.

Previous investigations of the SXRB used only the very soft energy regime ($\leq 0.3\,$keV) and concluded, that the diffuse Galactic X-ray radiation originates from multiple, independent coronal gas phases (Snowden et al., 1994). This interpretation supports the idea of a patchy Milky Way Halo gas. Kuntz & Snowden (2000) extend their investigation to E $\leq$ 2.0 keV, but performing *quasi–independent* fits for the soft and hard energy regimes respectively (see Fig. 8 in their work). With this method, they eventually suggest a two–thermal–component X–ray Halo. In contrast, we use all data available across the *entire* ROSAT energy band ($0.1\,\text{keV} \leq \text{E} \leq 2.1\,\text{keV}$) *simultaneously*. This approach allows to find a self–consistent model of the observed X-ray intensity and temperature distribution, because the temperature dependent plasma emissivity is closely related to the observed X-ray intensity within the individual ROSAT energy bands and their ratios (Kerp et al., 1999; Kappes et al., 2003). At the same time, the precision of the model gives us the opportunity to disclose the faintest source of emission contributing to the SXRB, the warm/hot intergalactic medium (see Sect. 6.3).

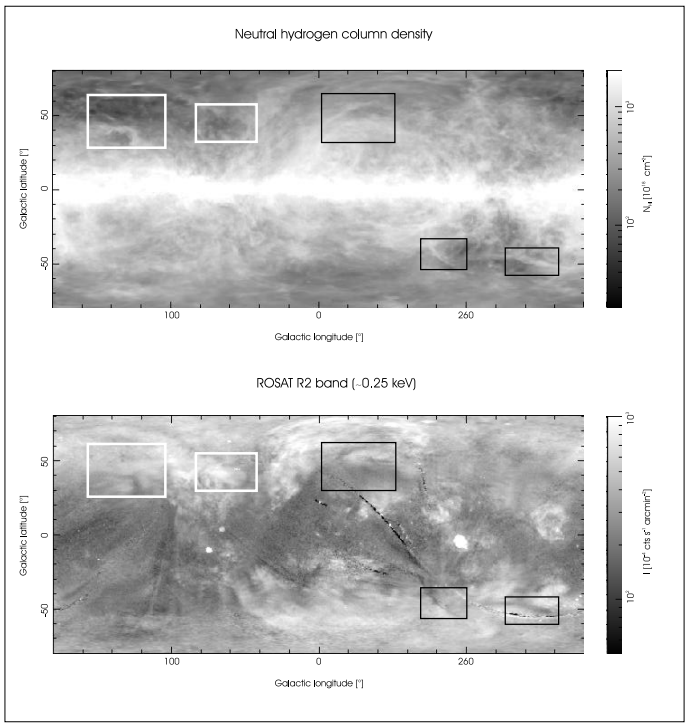

Fig. 30: **Upper panel:** *Map of the $N_{\rm HI}$ distribution for the* whole *sky ($|v_{\rm LSR}| < 25\,{\rm km\,s^{-1}}$). The highest* HI *emission is observed toward the Galactic Plane. Toward high Galactic latitudes, the map shows a rich structure in form of clouds and filaments in both, the northern and the southern hemisphere.* **Lower panel:** *Intensity distribution of the RASS in the energy regime within the R2 band. Apart from some individual extended X-ray sources (SNr) in the proximity of the Galactic Plane, the diffuse soft X-ray emission is clearly concentrated toward high Galactic latitudes. At first sight, the X-ray map shows up as the negative pattern of the $N_{\rm HI}$ image. Most of the* HI *clouds and filaments have their counterpart as shadows in the X-ray image (see examples indicated with the black boxes). This visual anti–correlation is because* HI *is a good tracer of the total photoelectric absorption by the ISM (see Sects. 4.2 and 5.2.3). The white boxes indicate the approximate areas of fields A and B in Sect. 5.3.*

5.1 The Data

5.1.1 X-ray Data

As we mentioned in Sect. 3.2.2, the ROSAT data are divided up into several independent energy bands (Snowden et al., 1997). All energy bands together cover the whole ROSAT Position Sensitive Proportional Counter (PSPC) energy range between 0.1 and 2.1 keV (Pfeffermann & Briel, 1986). The seven ROSAT standard energy bands are denoted as R1 to R7, from soft to hard X-ray photon energies (see Tab. 2). The width of each individual energy band depends mainly on the coating of the PSPC entrance window and the composition of the detector gas. We use the information of these seven energy bands to cover *all* diffuse X-ray emission components: the LHB (dominant in

the R1 and R2 regime), the Galactic X-ray Halo (R2, R3, R4, R5) and the contribution of the extragalactic X-ray background (R5, R6, R7), originating in the superposition of non–resolved distant point sources (see Sect. 5.3.4 and Fig. 1). The correlation analysis of the individual X-ray energy bands will provide a sensitive method to determine the temperatures and emissivities of the plasma and the contribution of the extragalactic XRB (see Sect. 5.3.3).

In order to improve the signal–to–noise ratio of the data for positional correlation studies of the HI and the X-ray intensity distribution, we also analyzed the merged ROSAT energy bands denoted as RC (R1+R2, $E \simeq 0.25\,\mathrm{keV}$), RM (R4+R5, $E \simeq 0.75\,\mathrm{keV}$) and RJ (R6+R7, $E \simeq 1.5\,\mathrm{keV}$) (see Tab. 2 and Snowden et al., 1995).

A measure for the accuracy of the X-ray data is given by the RASS exposure maps shown in Fig. 15 (Snowden et al., 1997), which only account for photon event statistics, but not for systematic uncertainties. These exposure maps will be used to weight the observations for statistical purposes, giving a higher statistical weight to areas with better photon statistics.

5.1.2 HI Data

Because of its abundance atomic hydrogen is *the best* tracer for the strength of the photoelectric absorption by the Galactic ISM. To quantify the amount of absorbing interstellar matter, HI 21 cm–line measurements with single dish radio telescopes are used (see also Sect. 5.2.3).

The Leiden/Dwingeloo survey of Galactic neutral hydrogen (Hartmann & Burton, 1997) is the prime source for the HI 21 cm–line intensity distribution toward the northern sky ($\delta \geq -30^\circ$). To include the southern sky, Arnal et al. (2000) performed a survey of the HI 21 cm–line emission with $\delta \leq -25^\circ$ at the Villa Elisa site. Both surveys have been corrected for stray–radiation (Kalberla et al., 1980; Hartmann et al., 1996), to warrant accurate HI column densities down to the significance level of $\Delta N_{\mathrm{HI}} \simeq 5 \cdot 10^{18}\,\mathrm{cm}^{-2}$. The major advantages of the new combined HI survey (Kalberla et al., in prep.) to earlier HI surveys for the whole sky are the large velocity coverage $-450\,\mathrm{km\,s}^{-1} \leq v_{\mathrm{LSR}} \leq 400\,\mathrm{km\,s}^{-1}$, the high velocity resolution $\Delta v_{\mathrm{LSR}} \simeq 1.0\,\mathrm{km\,s}^{-1}$ and the high angular resolution of $0.^\circ 6$.

The angular sampling of both HI surveys corresponds to a true-angle spacing of $0.^\circ 5$ in both l and b. For our cross-correlation of the RASS data with the HI data we calculated velocity integrated maps of the HI column density distribution. We re–projected these HI maps to the RASS grid to enable a pixel–by–pixel correlation. The pixel size is finally set to $48'$, four times that of the ROSAT all-sky survey and about $\sqrt{2} \times \mathrm{FWHM}$ of the Leiden/Dwingeloo and Villa Elisa beam size.

5.2 Radiative Transfer in the ROSAT Energy Regime

Figure 30 shows in the top panel the $N_{\rm HI}$ distribution extracted from the combination of the Leiden/Dwingeloo and Argentinian surveys (Kalberla et al., in prep.) and the X-ray intensity map in the ROSAT R2 band in the bottom panel, where both maps show the entire sky centered on the Galactic Center. Qualitatively there is an obvious negative correlation between both intensity distributions. Also individual HI structures can be found as deep soft X-ray shadows (marked by the black boxes in Fig. 30). In general, the X-ray image appears as a negative pattern of the HI column density, in agreement with the expectations for a "photoelectric absorption model".

5.2.1 The Model

To model quantitatively the SXRB, it is necessary to evaluate the contribution of the different individual components (LHB, Galactic X-ray Halo and the extragalactic background) to the total observed X-ray radiation (see Sect. 5). It is also necessary to account for photoelectric absorption produced by the ISM distributed along the line of sight. All these parameters have to be evaluated in the SXRB *radiative transfer equation*. We will use the approach introduced by Kerp et al. (1999):

$$I = I_{\rm LHB} + I_{\rm HALO} \cdot {\rm e}^{-\sigma_{\rm h} \cdot N_{\rm HI,h}} + I_{\rm EXTRA} \cdot {\rm e}^{-\sigma_{\rm e} \cdot N_{\rm HI,e}} \tag{9}$$

According to Eq. 9, the observed intensity of the SXRB is the superposition of three independent X-ray source components: the Local Hot Bubble ($I_{\rm LHB}$), a Galactic Halo component ($I_{\rm HALO}$) and the extragalactic background ($I_{\rm EXTRA}$). The amount of photoelectric absorbing matter inside the LHB is assumed to be negligible – with $N_{\rm LHB} \leq 10^{18}\,{\rm cm}^{-2}$ (Welsh et al., 2004) – Thus, and within the uncertainties of the data, there is no necessity to model the distribution of the photoelectric absorbing ISM within the LHB. $N_{\rm HI,h}$ represents the fraction of the total HI column density situated in front of the Galactic X-ray Halo which attenuates the emission represented by ($I_{\rm HALO}$). $N_{\rm HI,e}$ represents the HI column density attenuating the contribution of the extragalactic X-ray background. This is essentially the total HI column density measured. The photoelectric absorption cross sections are $\sigma_{\rm h}$ and $\sigma_{\rm e}$ which represent the *effective photoelectric absorption cross sections* (see Sect. 4.3) for the Galactic X-ray Halo and the extragalactic background respectively.

5.2.2 Coupling of the Energy Bands

Because Eq. 9 depends on the observed band, we have seven relations for the seven energy bands ($I^{\rm Ri}$, i = 1..7). These, however, are not independent. The intensities for

$I^{\mathrm{Ri}}_{\mathrm{EXTRA}}$ are defined by a power law. This means that, for each pair of bands Ri and Rj, we can write:

$$I^{\mathrm{Ri}}_{\mathrm{EXTRA}} = \mathrm{PL}(\Gamma, \mathrm{Ri}, \mathrm{Rj}) \cdot I^{\mathrm{Rj}}_{\mathrm{EXTRA}} \tag{10}$$

where $\mathrm{PL}(\Gamma, \mathrm{Ri}, \mathrm{Rj})$ is the band ratio Ri to Rj of a power law spectrum with index Γ and can be calculated using the instrumental parameters. For the intensities $I^{\mathrm{Ri}}_{\mathrm{LHB}}$ and $I^{\mathrm{Ri}}_{\mathrm{HALO}}$, we assume that these can be described by an optically thin Raymond-Smith plasma (Raymond & Smith, 1977). The energy dependences of the intensities are in this case defined by the plasma temperature and its abundances (see Sect. 2.2.1). Assuming that the abundance of the plasma is constant (Morrison & McCammon, 1983), we obtain fixed coupling constants between different energy bands where the band ratios depend strongly on plasma temperature:

$$\begin{aligned} I^{\mathrm{Ri}}_{\mathrm{LHB}} &= \mathrm{RS}(\mathrm{T}_{\mathrm{LHB}}, \mathrm{Ri}, \mathrm{Rj}) \cdot I^{\mathrm{Rj}}_{\mathrm{LHB}} \\ I^{\mathrm{Ri}}_{\mathrm{HALO}} &= \mathrm{RS}(\mathrm{T}_{\mathrm{HALO}}, \mathrm{Ri}, \mathrm{Rj}) \cdot I^{\mathrm{Rj}}_{\mathrm{HALO}} \end{aligned} \tag{11}$$

We can insert Eqs. 10 and 11 in the radiative transfer equation Eq. 9 for each energy band. In this manner, we normalize the equations in all bands to include the intensities of the three components in only *one* energy band. For example, if we use R2 for this normalization, we obtain for each Ri ($\mathrm{i} = 1, 3..7$):

$$\begin{aligned} I^{\mathrm{Ri}} &= \mathrm{RS}(\mathrm{T}_{\mathrm{LHB}}, \mathrm{Ri}, \mathrm{R2}) \cdot I^{\mathrm{R2}}_{\mathrm{LHB}} + \\ &+ \mathrm{RS}(\mathrm{T}_{\mathrm{HALO}}, \mathrm{Ri}, \mathrm{R2}) \cdot I^{\mathrm{R2}}_{\mathrm{HALO}} \cdot \mathrm{e}^{-\sigma_{\mathrm{h}} \cdot N_{\mathrm{HI,h}}} + \\ &+ \mathrm{PL}(\Gamma, \mathrm{Ri}, \mathrm{R2}) \cdot I^{\mathrm{R2}}_{\mathrm{EXTRA}} \cdot \mathrm{e}^{-\sigma_{\mathrm{e}} \cdot N_{\mathrm{HI,e}}} \end{aligned} \tag{12}$$

In Eq. 12, we have set up a model which includes the ROSAT observations in all energy bands with, in principle, eight free parameters:

$$I^{\mathrm{R2}}_{\mathrm{LHB}}, I^{\mathrm{R2}}_{\mathrm{HALO}}, I^{\mathrm{R2}}_{\mathrm{EXTRA}}, T_{\mathrm{LHB}}, T_{\mathrm{HALO}}, \Gamma, N_{\mathrm{HI,h}}, N_{\mathrm{HI,e}}$$

All these eight parameters will be discussed individually in the following sections. There, we will see that some of the parameters –like Γ or $I^{\mathrm{R2}}_{\mathrm{EXTRA}}$– are well known and can be safely considered to be fixed parameters.

5.2.3 Neutral Hydrogen Column Density

We use single dish 21 cm–line observations, which trace the total amount of neutral atomic hydrogen, in contrast to radio interferometers, which are not sensitive to the diffuse HI gas distribution. Of special importance is the warm neutral interstellar medium (WNM) which is smoothly distributed across the sky and undetectable by radio interferometers. In contrast, the cold neutral medium (CNM) is organized in individual filaments and clouds of a few degrees in angular extent. The CNM objects are directly associated with the infrared cirrus (Low et al., 1984) and reveal a smooth transition with increasing HI column density into the molecular medium (MM). Toward the high Galactic latitude sky the area filling factor of the individual gaseous phases is of most importance for the soft X-ray astronomy. The area filling factor of the MM is negligible at high Galactic latitude (Hartmann et al., 1998). The CNM is observable in about 30% of all directions (Haud et al., in prep.) while the WNM is detected across the whole sky. There is no single line of sight without WNM. Toward the northern Galactic hemisphere the WNM shows up with minimum column densities of about $N_{\rm HI} \simeq 4.5 \cdot 10^{19}\,{\rm cm}^{-2}$ (Lockman et al., 1986) and a factor of two to four higher minimum column densities toward the southern sky. The smooth distribution of the WNM across the whole sky is completely resolved by moderate size radio telescopes.

In the soft X-ray energy domain below the carbon K–edge ($E < 0.28\,{\rm keV}$) neutral hydrogen and helium are the dominant photoelectric absorbers (Wilms et al., 2000). Heavier elements become relevant only at higher photon energies. The imprint of the heavier elements above the carbon K–edge is below the level of precision of the ROSAT data (about 10%), and accordingly negligible in the present work. Because of the strong energy dependence of the photoelectric absorption cross section ($\sigma \propto E^{-\frac{8}{3}}$) (Morrison & McCammon, 1983) the X-ray attenuation produced by WNM and CNM are most significantly detectable in the ROSAT RC band. Within the ROSAT RC band the typical size of the absorption cross–section is about $\sigma({\rm RCband}) = 0.7 \cdot 10^{-20}\,{\rm cm}^2$ corresponding to a WNM of $N_{\rm HI} = 1.3 \cdot 10^{20}\,{\rm cm}^{-2}$. Both quantities together indicate that the large scale (sizes up to tens of degrees and higher) intensity distribution of the SXRB produced by the Milky Way Halo plasma and the extragalactic XRB is modulated mainly by the column density distribution of the WNM.

Because of the very good radial velocity resolution of the HI data ($\Delta v_{\rm LSR} \simeq 1\,{\rm km\,s}^{-1}$) (Kalberla et al., in prep.) we can distinguish individual velocity regimes like the intermediate–velocity clouds (IVCs) $100\,{\rm km\,s}^{-1} \geq |v_{\rm LSR}| \geq 50\,{\rm km\,s}^{-1}$ or the high–velocity clouds (HVCs) $|v_{\rm LSR}| \geq 100\,{\rm km\,s}^{-1}$ (Wakker & van Woerden, 1997), the Milky Way Gas ($-50\,{\rm km\,s}^{-1} \leq v_{\rm LSR} \leq 50\,{\rm km\,s}^{-1}$) and the whole measured column density distribution $|v_{\rm LSR}| \leq 400\,{\rm km\,s}^{-1}$. This is a very important capability in order to distinguish between the amount of X-ray absorbing gas in front of the Milky Way Halo X-ray plasma ($N_{\rm HI,h}$) and the total amount of gas in front of the extragalactic background ($N_{\rm HI,e}$), which is a crucial point in our investigation (see Sect. 6.1). From Eq.9 it is obvious that the extragalactic component is absorbed by the total observed

HI column density, while $N_{\mathrm{HI,h}}$ has to be lower because it accounts only for the HI in front of the Galactic X-ray Halo, which would have a scale height of about 4 kpc (Pietz et al., 1998). Thus, some HI gas observed in the combined 21 cm–line surveys could be located outside the Galactic X-ray Halo, i. e. the HVCs (Wakker & van Woerden, 1997). In this case, these clouds would not attenuate the radiation from the Milky Way corona. In a first approximation (see Sect. 5.3), we freeze this parameter to cover $|v_{\mathrm{LSR}}| \leq 125\,\mathrm{km\,s^{-1}}$, which includes all intermediate and most of the high velocity clouds. In Sect. 6.1 we present a method to evaluate $N_{\mathrm{HI,h}}$ as a free parameter.

5.3 First Approach with Two Individual Fields of Medium Angular Size

To illustrate our method, applied to the whole sky in latter sections, we selected two fields which have different sky locations and HI velocity structures. These differences give us the opportunity to explore – in a very sensitive way – the impact of N_{HI} as a function of v_{LSR} on the SXRB intensity distribution.

The fields analyzed are centered on Galactic coordinates (*l*,*b*) = (65°, 35°) (Field A) and (*l*,*b*) =(135°, 45°) (Field B) and have sizes of $40° \times 25°$ and $50° \times 40°$ respectively (see white boxes in Fig. 30). The size of each individual field is sufficiently large to cover a significant high HI column density contrasts (about -14 dB in field B). This high column density contrast allows a consistent analysis of the correlation between X-rays intensities and HI column densities (see, e.g. Kuntz & Snowden, 2000). In particular, toward the high column density regions in each field the distant XRB radiation is strongly attenuated and I_{LHB} can be well determined while toward the low column density regions I_{HALO} and I_{EXTRA} can be evaluated best.

Field A (see Fig. 31) reveals a large column density contrast above a factor of nineteen. The lowest HI column density $N_{\mathrm{HI}} = 0.6 \cdot 10^{20}\,\mathrm{cm^{-2}}$ while the maximum is $N_{\mathrm{HI}} = 11.5 \cdot 10^{20}\,\mathrm{cm^{-2}}$. The lowest column density region is nearly as transparent as the "Lockman window" (see next paragraph) while the high column density part is totally opaque for distant soft X-ray photons originating from the Galactic X-ray Halo or extragalactic sources. The distribution of the HVC and the IVC toward the field is highly complex as shown in Fig. 2 from Kerp et al. (1999).

Field B covers the "Lockman window", which is the region with the lowest HI column density on the whole the sky (Lockman et al., 1986). Recently Kappes et al. (2003) found that the measured HI column density is not sufficient to account for the total X-ray attenuation observed, as shown in Fig. 5 in their work. This finding influences the determination of the field averaged quantities I_{LHB}, I_{HALO}, I_{EXTRA} and T_{LHB}, T_{HALO} by only a few percent because of the small area covering factor of the Lockman window region vs. the field extent. Toward this field of interest, Kerp et al. (1999) also claimed the detection of excess X-ray emission associated with the HVC complex C.

Moreover, toward the northern tip of the ecliptical Pole Loop excess X-ray emission is detected by Kerp et al. (1999) and Kappes et al. (2003). Kappes et al. (2003) suggest that the computed excess X-ray emission reported by Kerp et al. (1999) is accidentally produced by the extragalactic HI gas associated with the tidal gas of the M81/M82–group of galaxies. The radial velocity of the neutral M81/M82 intergroup gas is about $v_{\rm LSR} \sim 50\,{\rm km\,s^{-1}}$, well within the Milky Way gas velocity regime. Kerp et al. (1999) assumed that all $N_{\rm HI}$ within the velocity interval $|v_{\rm LSR}| < 100\,{\rm km\,s^{-1}}$ is located in front of the Milky Way Halo plasma. Only toward the M81/M82–group of galaxies this hypothesis is incorrect. Accordingly, toward this direction Kerp et al. (1999) overestimated the amount of the X-ray absorber and the modeled X-ray intensity distribution is too faint, leading to an excess in the difference map between the observed and modeled SXRB intensity distribution.

In the remaining of this Sect., we present the constraints and assumptions that can be made on the different parameters involved in Eq. 9, as well as the fit method and goodness–of–fit tests used.

5.3.1 The Local Hot Bubble

The contribution of the LHB to the SXRB is represented in Eq. 9 by the term $I_{\rm LHB}$. This corresponds to the X-ray emission of a hot plasma within the local environment of the Sun, the existence of which was already established by rocket experiments (McCammon et al., 1983). The published results for the shape of the LHB based on X-ray observation are derived from the ROSAT all–sky survey data, where the intensities are in the range $I_{\rm LHB} = (250 \ldots 820) \cdot 10^{-6}\,{\rm cts\,s^{-1}\,arcmin^{-2}}$ (Snowden et al., 1998). There is still controversy on the temperature, shape and extension of the LHB plasma (Sfeir et al., 1999; Lallement et al., 2003). We will see in Sect. 5.5.1 that an approximation using a single LHB intensity value which varies by about 30% across the whole sky is sufficient to model the SXRB within the precision of the RASS.

Only a few local clouds are intermixed with the hot X-ray emitting plasma of the LHB (e.g. Kerp et al., 1993; Snowden et al., 1993) with a negligible area filling factor, allowing to simplify Eq. 9 to use the unabsorbed $I_{\rm LHB}$ value.

5.3.2 The Milky Way X-ray Halo

The hot coronal gas within the Milky Way Halo and outside the LHB was one of the major discoveries of the ROSAT mission (see Chap. 1 and Fig. 2). This diffuse X-ray emission is represented in the radiative transfer equation by $I_{\rm HALO}$. The number of independent plasma components responsible for this SXRB emission is a matter of debate, as well as their respective temperatures (see Kuntz & Snowden, 2000; Pietz et al., 1998).

In this work we will demonstrate that Eq. 9 with a *single and constant temperature* Milky Way Halo plasma in addition to the LHB emission and the extragalactic X-ray background is sufficient to construct a consistent model of the SXRB (see Sect. 5.3.7). The exponential factor accompanying I_{HALO} in Eq. 9 represents the photoelectric absorption caused by the ISM with a scale height below that of the Milky Way X-ray Halo. The amount of absorbing gas is represented by $N_{\mathrm{H\,I,h}}$ in Eq. 9.

5.3.3 Temperatures of the Galactic Components

The temperatures of the LHB and Galactic Halo X-ray emitting plasma are not explicitly included in Eq. 9. However, they are of key importance for studies of the SXRB. Because of the usage of broad energy bands (see Sect. 4.3), the exact values of the effective photoelectric cross sections are a function of the *a priori* assumed plasma temperature, hidden in the source spectrum term $S(E)$ in Eq. 8.

Plasma temperatures also determine the relative fraction of the observed SXRB intensities within the different energy bands. Given an observed intensity in one energy band and the plasma temperature, it is possible to calculate its contribution to all the other energy bands. This causes the temperatures of the LHB and Galactic X-ray Halo to be very sensitive parameters in a model that accounts for all ROSAT energy bands simultaneously (see Figs. 32 and 34).

5.3.4 The Extragalactic Background

The extragalactic component of the SXRB stems from the superposed emission of point sources, in particular AGNs (e.g. Tozzi et al., 2001). Following Hasinger et al. (2001) we can approximate the spectrum of this superposed emission by a power law ($E^{-1.5}$). The ROSAT RC band intensity has been determined by Barber et al. (1996) with a value of $I_{\mathrm{EXTRA}} = (230 \pm 90) \cdot 10^{-6}\,\mathrm{cts\,s^{-1}\,arcmin^{-2}}$. Like in the case of the LHB and Galactic X-ray Halo, the knowledge of the intensity for one band and of the spectrum of the extragalactic component allows to extrapolate the corresponding intensities for all other ROSAT energy bands. In this work, we allow the value for I_{EXTRA} to vary in a range compatible with the one by Barber et al. (1996) in order to find the best fit value for *all energy bands simultaneously*. In contrast to the I_{LHB} and I_{HALO} (see Sect. 5.4), once we obtain the best fit the value for I_{EXTRA}, we assume this value to remain constant along all lines of sight. The absorption of the extragalactic component is represented by the factor $\mathrm{e}^{-\sigma_{\mathrm{e}} \cdot N_{\mathrm{H\,I,e}}}$ in Eq. 9.

5.3.5 Method

The sizes of fields A and B are sufficiently large to cover a large dynamic range in $N_{\mathrm{H\,I}}$. They are however small enough to approximate I_{LHB}, I_{HALO}, T_{LHB} and T_{HALO} with

Tab. 5: *Contribution of the different diffuse X-ray emission components to the observed X-ray intensities. These absolute values ([$10^{-6}\,\mathrm{cts\,s^{-1}\,arcmin^{-2}}$]) are calculated based on the best–fit model for field A, with* $T_{\mathrm{LHB}} = 10^{5.9}\,\mathrm{K}$, $T_{\mathrm{HALO}} = 10^{6.2}\,\mathrm{K}$ *and* $\Gamma = -1.5$ *(see Sect. 5.2.2).*

component	*R*1	*R*2	*R*4	*R*5	*R*6	*R*7
I_{LHB}	209	144	0	0	0	0
I_{Halo}	713	1080	98	49	0	0
I_{EXTRA}	48	56	9	15	25	17

single values independent of the Galactic coordinates. In case of I_{LHB} this approach can be justified by inspecting the shape of the LHB published by Snowden et al. (1998). The maximum variation for the medium and high Galactic latitude sky is about a factor of three, corresponding to about $\Delta I_{\mathrm{LHB}} = 570 \cdot 10^{-6}\,\mathrm{cts\,s^{-1}\,arcmin^{-2}}$ in the ROSAT RC band. The angular separation between the I_{LHB} intensity maximum and the minimum is approximately 100° (see Fig. 10 in Snowden et al. (1998)). These values yield mean gradients below $57 \cdot 10^{-6}\,\mathrm{cts\,s^{-1}\,arcmin^{-2}\,degree^{-1}}$. Therefore, in case of areas with an angular of radius $\simeq 20°$ – like fields A and B – the variation in I_{LHB} for the different lines of sight generally keeps below $100 \cdot 10^{-6}\,\mathrm{cts\,s^{-1}\,arcmin^{-2}}$. For field A and B respectively, we find intensity ranges $400 < I_{\mathrm{LHB}} < 500$ and $450 < I_{\mathrm{LHB}} < 600$ ($[10^{-6}\,\mathrm{cts\,s^{-1}\,arcmin^{-2}}]$). Such a variation is below the level of precision of the ROSAT RC band data. Additionally, the directions of both fields A and B have been chosen to avoid the maximum gradients of I_{LHB} presented in Snowden et al. (1998). Thus, we can safely consider I_{LHB} to stay constant across each field of interest. Using similar considerations, the other parameters, in particular both plasma temperatures, are also fixed to locally constant values.

Toward both fields of interest the number of free parameters in the radiative transfer equation Eq. 9 is now four ($I_{\mathrm{LHB}}, I_{\mathrm{HALO}}, T_{\mathrm{LHB}}$ and T_{HALO}). Note that the X-ray intensities and temperatures are not independently determined for each individual ROSAT energy band, but one set of the free parameters, for example for the ROSAT R2 band, determines the corresponding intensities in all other ROSAT energy bands (see Sect. 5.2.2). To illustrate this, we give in Tab. 5 the best fit solution for field A subdivided into the contribution of both plasmas and the extragalactic background radiation.

According to Tab. 5, I_{LHB} is only detectable within the ROSAT R1 and R2 band, while I_{HALO} dominates the X-ray emission within the R4 and R5 energy band. I_{EXTRA} can be determined without any confusing emission in the R6 and R7 energy bands. The relative contribution of the different diffuse emission components is given by the product of the instrumental response $R(E)$ and the X-ray spectrum of each individual source $S(E)$ in Eq. 8. Accordingly we can extrapolate the contribution of each component, determined within any ROSAT energy band, to the other energy bands of interest (see Sect. 5.2.2). We make use of this behavior by fitting the ROSAT R2 energy band and

monitoring in parallel the deviation of the fit results in all other bands (see Sect. 5.3.6).

The method that we use to find the best fit values is based on the following concept. We search for conditions where we can be evaluate one free parameter as independent as possible of the other free parameters. For example, we can constrain the study of the I_{LHB} term best toward those lines of sight with very high $N_{\mathrm{H\,I,h}}$. This high column density implies high photoelectric absorption of the distant components of the SXRB (I_{HALO} and I_{EXTRA}). Accordingly the observed X-ray intensity can be attributed only to the LHB and the determined R1 intensity can be used to infer a first approximation for I_{LHB}. Similar considerations allow us to evaluate the remaining free parameters (for details see Kappes et al. (2003)). Given such initial estimates, we finally start the iteration process for all energy bands simultaneously. For this purpose, we freeze the values of three free parameters with the best known initial values for them, and find a new best fit value for the remaining free parameter. Repeating this procedure for I_{LHB}, I_{HALO}, T_{LHB} and T_{HALO} successively yields improved values for the next iteration step. An additional constraint arises from that we can not obtain a higher precision of the intensity parameters than that of the uncertainties of the X-ray data. Thus, we can reduce the parameter space of our search to a discrete set of points in each iteration step. The distance between these points is given by the precision of the data. For example, the mean precision of the ROSAT RC band in field A amounts to some $100 \cdot 10^{-6}\,\mathrm{cts\,s^{-1}\,arcmin^{-2}}$. In this case, we searched for best fit solutions for the X-ray intensities among a set with linear separations of $50 \cdot 10^{-6}\,\mathrm{cts\,s^{-1}\,arcmin^{-2}}$.

For each set of parameters we calculated so–called *model images* of the X-ray distributions in each ROSAT energy band. In the following section, we present a method to quantitatively compare the modeled images with the ROSAT data which is used as criterion to estimate the goodness of each set of parameters.

5.3.6 Statistical test of the SXRB models

In order to test the goodness of each new set of parameters derived from the iteration, we use a random variable δ for which the distribution parameters (measures of central location and dispersion) are a measure for the correlation between the modeled and observed SXRB intensity distribution. This is done in a pixel–by–pixel approach. For each set of parameters, we calculated *difference maps* (observation *minus* model) in all ROSAT energy bands. Then, we normalize this difference image with the exposure map of the ROSAT observation. With this normalization, we weight the sample, attributing a higher significance to pixels corresponding to a longer exposure time. Moreover, this procedure normalizes the statistical variable δ to follow a normal distribution $N(0,1)$, in the case of a perfect quantitative correlation. With this description, the definition of δ is:

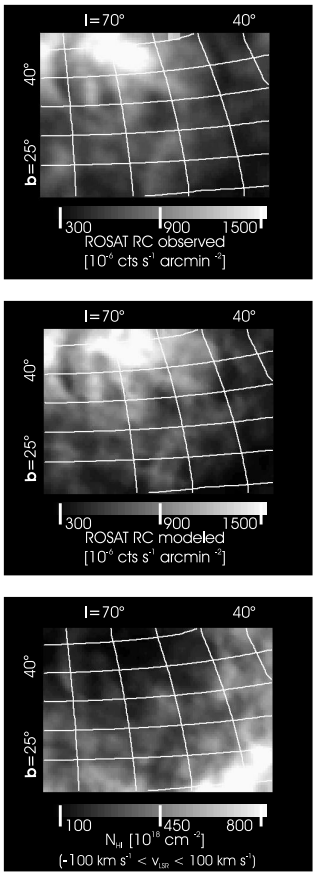

Fig. 31: **Top:** *RASS image map of field A in the RC energy band. The Galactic coordinates of the region are shown to the top and to the left.* **Middle:** *Best fit model for field A as obtained with the method presented in Sect. 5.3. All structures observed in the upper panel are well reproduced by the model image.* **Bottom:** HI *column density distribution for the field A region. Like in Fig. 30, this map shows as the negative pattern of the upper panels. Unfortunately, no distance information is given with the* HI *and here we only see the projection on the celestial sphere of the real 3–D distribution.*

$$\delta = \frac{I_{\text{observed}} - I_{\text{modeled}}}{\sigma_{\text{observed}}} \tag{13}$$

The set formed by the values of δ for all lines of sight across each individual field of interest is considered as a statistical sample for which we determine the mean value (mean μ) and the degree of dispersion (standard deviation σ). In order to evaluate the goodness of a specific set of parameters, we compare the statistical estimators obtained for the corresponding sample of δ with that of a $N(0,1)$ distribution. Is is important to note again, that we perform these calculations for all ROSAT energy bands simultaneously and independently, while the intensity and temperature values are derived only for the ROSAT RC band. Therefore, we have one pair (μ, σ) for each

energy band to be fitted at the same time.

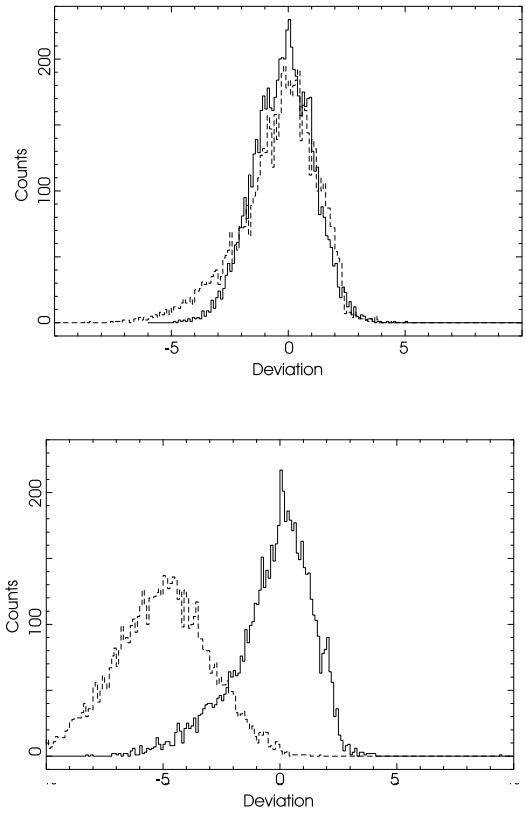

Fig. 32: **Top:** *Histograms of the model deviation δ for the ROSAT energy bands RM (solid line) and RC (dashed line). The histograms are accumulated in the field A region for a model with a one–component X-ray Halo.* **Bottom:** *Equivalent histograms obtained with a two–temperature X-ray Halo following Kuntz & Snowden (2000) ($T_{\mathrm{LHB}} = 10^{6.15}\,\mathrm{K}$, $T_{\mathrm{HALO_1}} = 10^{6.40}\,\mathrm{K}$ and $T_{\mathrm{HALO_2}} = 10^{6.00}\,\mathrm{K}$). We obtain a better fit for each band individually by fitting one temperature to every band independently but the histogram shows that this model fails when we consider the contributions of* all *components to fit* all *ROSAT energy bands* simultaneously.

After ten iteration steps the derived values converge within the uncertainties of the data and no further improvement can be achieved. We give here as an example the best fit values obtained for μ and σ in ROSAT RC and RM bands for field A: $\mu_{\mathrm{C}} = 0.1, \sigma_{\mathrm{C}} = 1.5$ and $\mu_{\mathrm{M}} = -0.4, \sigma_{\mathrm{M}} = 1.1$ (see Fig. 32). We will see in Sect. 5.5 that the higher accuracy obtained for the higher energy regime is related to a good modeling of the Galactic X–ray Halo. The RASS map for field A in RC band and the corresponding best fit model map are shown in Fig. 31 to visually illustrate the goodness of the fit.

The best fit parameters for the intensities and temperatures obtained with the method described above for field A and field B in the ROSAT RC band are:

Field A :

$$
\begin{aligned}
I_{\mathrm{LHB_A}} &= (350 \pm 80) \cdot 10^{-6}\,\mathrm{cts\,s^{-1}\,arcmin^{-2}} \\
I_{\mathrm{HALO_A}} &= (1950 \pm 100) \cdot 10^{-6}\,\mathrm{cts\,s^{-1}\,arcmin^{-2}} \\
I_{\mathrm{EXTRA_A}} &= (170 \pm 70) \cdot 10^{-6}\,\mathrm{cts\,s^{-1}\,arcmin^{-2}} \\
T_{\mathrm{LHB_A}} &= 10^{5.9\pm0.1}\,\mathrm{K} \\
T_{\mathrm{HALO_A}} &= 10^{6.2\pm0.1}\,\mathrm{K}
\end{aligned}
$$

Field B :

$$
\begin{aligned}
I_{\mathrm{LHB_B}} &= (350 \pm 90) \cdot 10^{-6}\,\mathrm{cts\,s^{-1}\,arcmin^{-2}} \\
I_{\mathrm{HALO_B}} &= (1400 \pm 120) \cdot 10^{-6}\,\mathrm{cts\,s^{-1}\,arcmin^{-2}} \\
I_{\mathrm{EXTRA_B}} &= (170 \pm 70) \cdot 10^{-6}\,\mathrm{cts\,s^{-1}\,arcmin^{-2}} \\
T_{\mathrm{LHB_B}} &= 10^{5.9\pm0.1}\,\mathrm{K} \\
T_{\mathrm{HALO_B}} &= 10^{6.2\pm0.1}\,\mathrm{K}
\end{aligned}
$$

Within the uncertainties I_{EXTRA}, T_{LHB} and T_{HALO} are identical in both fields. This supports our model assumption of only two isothermal plasma in Eq. 9.

5.3.7 Other models for the Halo emission

In Sect. 5, we mentioned other approaches to model the diffuse emission of the Galactic X–ray Halo which we will now briefly discuss. We tested a model with a multi–temperature Halo according to Kuntz & Snowden (2000) using our iterative method. The best fit results with this model are shown in the lower panel of Fig. 32 –with $\mu_{\mathrm{C}} = -4.5, \sigma_{\mathrm{C}} = 2.0$ and $\mu_{\mathrm{M}} = 0.1, \sigma_{\mathrm{M}} = 1.7$ for the multi–temperature model–, where we see that the level of precision of the single–temperature model is not achieved. If we adjust to each ROSAT energy band an individual Halo plasma temperature, independently of all other energy bands, we obtain better fits for each energy band individually. But if we compute the contribution of all these independent components to the neighboring energy regimes, a completely simultaneous fit of all ROSAT energy bands is not possible even for the angular scale of our fields of interest.

Almy et al. (2000) present an adiabatic polytrope scenario in which the temperature of the X–ray Halo increases around the Galactic Plane and the temperature gradient is maximized in the low Galactic latitude regions and towards the Galactic Center. In our work, we focus on the high Galactic latitude sky (see Sect. 5.4) where the temperature gradient suggested by Almy et al. (2000) is small. Considering the uncertainties in calculating the radiation transfer at low Galactic latitudes, we find that the verification or refutation of such a moderate temperature gradient is not possible with the method presented here.

5.4 Full–sky Application of the Fit Procedure

The difference between both I_{HALO} values derived for the two distant regions A and B in Sect. 5.3.6 implies that I_{HALO} is constant across tens of degrees but varies appreciable across the sky as already suggested by (Kerp et al., 1999; Pietz et al., 1998). In contrast to the intensity, the plasma temperature of T_{HALO} remains constant between both fields of interest. This finding is in disagreement with the multi–phase Halo model of Kuntz & Snowden (2000). According to their model, the plasma located beyond the LHB in field A and the one in field B would be physically different, with different temperatures and emission measures. For such a model, the patchy nature of a multi–temperature Milky Way X-ray Halo would prevent us from finding a simple satisfactory model of the SXRB for all ROSAT energy bands simultaneously in which the Galactic Halo is represented by *only one* X-ray plasma component.

To finally differentiate between a patchy or a smooth Milky Way X-ray Halo, we extend our study to the whole sky. We focus on high Galactic latitudes with $|b| > 25^\circ$ to avoid the Galactic Plane, opaque to soft X-rays (see Figs. 35 and 36). Using the X-ray and HI data, we study the so–called *unabsorbed Halo intensity* $\tilde{I}_{\mathrm{HALO}}$ which can be calculated for each individual line of sight (l,b) according to:

$$\tilde{I}_{\mathrm{HALO}}(l,b) = \frac{I(l,b) - (I_{\mathrm{LHB}}(l,b) + I_{\mathrm{EXTRA}}(l,b) \cdot \mathrm{e}^{-\sigma_{\mathrm{e}} \cdot N_{\mathrm{HI,e}}})}{\mathrm{e}^{-\sigma_{\mathrm{h}} \cdot N_{\mathrm{HI,h}}}} \tag{14}$$

$I(l,b)$ is the observed ROSAT intensity. $I_{\mathrm{LHB}}(l,b)$ and $I_{\mathrm{EXTRA}}(l,b)$ are the intensities of the LHB and of the extragalactic background at coordinates (l,b), where the latter can be safely approximated with a constant function (see Sect. 5.3.4). Thus, we can interpret $\tilde{I}_{\mathrm{HALO}}(l,b)$ as a measure of the emission of the Galactic X-ray Halo before it is attenuated by photoelectric absorption.

In the first approach to investigate the variation of the X-ray Halo intensity with Galactic coordinates ($I_{\mathrm{HALO}}(l,b)$), we approximate the contribution of the LHB with a constant function $I_{\mathrm{LHB}}(l,b) = 350 \cdot 10^{-6}\,\mathrm{cts\,s^{-1}\,arcmin^{-2}}$ in ROSAT RC band, a value compatible with the one in Snowden et al. (1998). For the plasma temperatures, we

use as an initial estimate the best fit values derived in Sect. 5.3.6, which are identical for both fields A and B ($T_{\rm LHB} = 10^{5.9}\,{\rm K}$ and $T_{\rm HALO} = 10^{6.2}\,{\rm K}$).

5.4.1 The Shape of the Halo

The distribution of $\tilde{I}_{\rm HALO}$ shown in Fig. 33 suggests that toward the Galactic Center the path length through the X-ray Halo plasma reaches its maximum, while toward the anti–center region a local minimum is observed. This anti–center symmetry flattens toward higher Galactic latitudes (upper panel in Fig. 33). Both findings are consistent with other observation parameters as compiled in Kalberla & Kerp (1998). According to their isothermal gaseous Halo model, the vertical scale height is 4.4 kpc while the radial scale length is 15 kpc.

Kalberla & Kerp (1998) used the data published by Pietz et al. (1998) to fit their model. Here, we use the latest model published by Kalberla (2003) to approximate the shape of the Galactic X-ray Halo. There is also a significant improvement in the data, both X–ray and HI, used here in comparison with those used by Pietz et al. (1998). The normalization of the X-ray emissivity of the model by Kalberla (2003) is in good agreement with the ROSAT observations (see thick lines in Fig. 33). Equipped with such a model of the Milky Way X-ray Halo intensity distribution, we introduce a modified radiative transport equation:

$$I(l,b) = I_{\rm LHB} + I_{\rm HALO}(l,b) \cdot {\rm e}^{-\sigma_{\rm h} \cdot N_{\rm HI,h}} + I_{\rm EXTRA} \cdot {\rm e}^{-\sigma_{\rm e} \cdot N_{\rm HI,e}}. \qquad (15)$$

Here, the variation of $I_{\rm HALO}(l,b)$ as a function of (l,b) is determined by the Halo model of Kalberla (2003). We use the iterative approach presented in Sect. 5.3.5 to optimize the values of the parameters $I_{\rm LHB}$, $I_{\rm HALO}(l=0^\circ, b=90^\circ)$, $T_{\rm LHB}$ and $T_{\rm HALO}$ in Eq. 15. The application of this procedure yields in very accurate models for the whole SXRB, with statistical deviations between the observation and the model of $\mu \simeq 0$ and $\sigma \simeq 1.7$ (see Sect. 5.3.6 for interpretation) in *all* ROSAT energy bands simultaneously.

The precision and the sensitivity to the plasma temperatures of our method are shown in Fig. 34. The predictions of our best fit model are in good agreement with the ROSAT observations in all energy bands. With a small variation in the temperature of the plasma components this good agreement cannot be further achieved (like in the dotted line of Fig. 34).

After completing our iterative procedure, a single–plasma Galactic X-ray Halo with $T_{\rm HALO} = 10^{6.15\pm0.1}\,{\rm K}$ turns out be sufficient to explain the SXRB in all energy regimes, with a very accurate determination of its temperature. In Sect. 5.5 we will see how to use this model to investigate the 3–D structure of the absorber and obtain the final results shown in the upper right panels of Figs. 35 and 36.

5.5 Deviation maps

To investigate the 3–D structure of the X-ray emitting and absorbing medium we use the spatial distribution of the variable δ introduced in Sect. 5.3.6. The values of δ for different lines of sight can be used to calculate *deviation maps*, which show the deviation of the modeled to the observed data toward each individual position (see Figs. 35 and 36). An appropriate modeling of the SXRB would yield the highest and lowest values of δ to be randomly distributed across the whole sky, representing only the uncertainties of the data. This implies, that sky portions that systematically show high positive or high negative deviations (i. e., $|\delta| > 3$), are associated to *systematic deviations* of the model in comparison to the data. The very bright and very dark areas in the middle and lower panels of Figs. 35 and 36 are examples of these *deviation regions*, corresponding to positive and negative values of δ respectively. A positive value of δ (δ*-positive* region) means that the modeled intensity is too low compared to the observed one, and a negative value (δ*-negative* region) indicates an excess of emission in the model with respect to the ROSAT observation.

Following this interpretation of δ, we produce and analyze deviation maps for our best fit model in all ROSAT energy bands. First, we focus on the high and medium energy regime. The deviation maps corresponding to the south Galactic sky (Fig. 36) in this regime are dominated by the structure in the RASS exposure maps and we cannot identify any significant δ*-positive* or δ*-negative* regions. In the north Galactic sky (Fig. 35) we detect only a few point–like δ*-positive* regions in the R7 deviation map, which can also be traced in the softer energy bands (R4 and R5). We identify this regions with residuals from the point source subtraction associated with the Virgo Cluster .In the medium energy regime, we detect the contribution of the North Polar Spur which is also present in the deviation maps for the softer energy regimes R1 and R2.

The deviation maps in the soft energy regime (R1 and R2) show a richer structure in intensity than those for higher energies (see middle panels in Figs. 35 and 36). This is an expected result because of the exponential increase of the photoelectric absorption cross section with decreasing photon energy (see Sect. 5.2.3). In this manner, the photon energy regime from R4 to R7 provides mainly information about the Milky Way Halo and the extragalactic background, because of the "harder" spectrum of these components in comparison to that of the LHB. Thus, the results obtained for the higher energy regimes indicate good accuracy in our models of the Milky Way Halo and the extragalactic background while the structure observed in the case of the soft energy regime is related to our models of: 1) the LHB and 2) the amount of photoelectric absorption. In the following and in Sect. 6.1, we will focus on the R1 and R2 bands and analyze these two possibilities.

5.5.1 The shape of the Local Hot Bubble

The extragalactic X-ray background emission and the shape of the Milky Way X-ray Halo intensity distribution might be considered as well determined quantities. Their contribution to the soft energy regime can be safely subtracted from the RASS. In addition, the temperature of the LHB has been precisely determined (see Sect. 5.4) but no considerations on the variation of I_{LHB} with Galactic coordinates have been made until this point. Following previous works, Sfeir et al. (1999) in Fig. 4 or Snowden et al. (1998) in Fig. 10, the variation for I_{LHB} across the region of interest ($|b| > 30$) keeps below the level of 50 %. This corresponds to $\Delta I_{LHB} \simeq 150 \cdot 10^{-6}\,\mathrm{cts\,s^{-1}\,arcmin^{-2}}$ in the ROSAT RC band which is about one and a half the precision of the RASS in this energy regime. Therefore, the error introduced by considering a spherical LHB for the medium and high Galactic latitude sky stays below a two sigma level and becomes undetectable with our approach. In fact, there are no large extended structures with high mean deviation ($|\delta| \geq 2$) in the maps in Figs. 35 and 36 that can unambiguously be related to variations in I_{LHB}. As we will see in Chap. 6, we associate all remaining *δ-positive* and *δ-negative* regions with origins different from the LHB. This is compatible with the picture of a LHB with a relatively smooth intensity distribution towards the Galactic Poles and consistent with the scenario of a hot gas expanding through a medium with lower density towards the higher Galactic latitudes.

Toward the Galactic Plane, the sources of contamination in the R1 and R2 regime dominate over the true SXRB. This prevents us from obtaining reliable models of the LHB for this region based only on ROSAT data.

5.6 Conclusions of the correlation

Our analysis of the SXRB and its correlation with the new HI survey for the whole sky leads to a consistent model of the radiative transfer for the SXRB through the ISM. The contribution of the Galactic X-ray Halo to the SXRB can be explained by an isothermal plasma with a spatial distribution in agreement with the predictions of the Dark Matter Halo by Kalberla (2003). A patchy X–ray Halo can be ruled out since there is no evidence for local variations in the temperature of the Galactic X-ray plasma on a large scale.

Our results are for the X–ray Halo are more in agreement with an isothermal Halo model for high Galactic latitudes like in Pietz (1997). It is important that we can extend the conclusion for the northern sky to the southern sky, apart for the significantly better quality of the data used: $12'$ angular resolution and all energy bands for the X–ray data in comparison to $24'$ and only the broadest energy bands. The improvement in the precision of the models for the X–ray Halo, allows to investigate the RASS in much more detail, as we will see in the following chapter.

A spherical approximation of the LHB for the regions with $|b| > 25^\circ$ is sufficient to explain the contribution of the local plasma with the precision of the data given (see Sect. 5.5.1). The local variations in intensity of the LHB never exceed a factor 2 higher or lower than the best fit value given in Sect. 5.3 and are only marginally present in the deviation maps (Figs. 35 and 36) of our models of the SXRB. In order to achieve higher precision in the determination of the shape of the LHB, it is necessary to make use of other techniques like measures of absorption lines in the optical and UV range (Sfeir et al., 1999). The temperature of the local plasma ($T_{\mathrm{LHB}} \simeq 10^{5.9}\,\mathrm{K}$) is found to be constant toward high Galactic latitudes and significantly lower than the temperature of the Galactic X-ray Halo ($T_{\mathrm{HALO}} \simeq 10^{6.15}\,\mathrm{K}$).

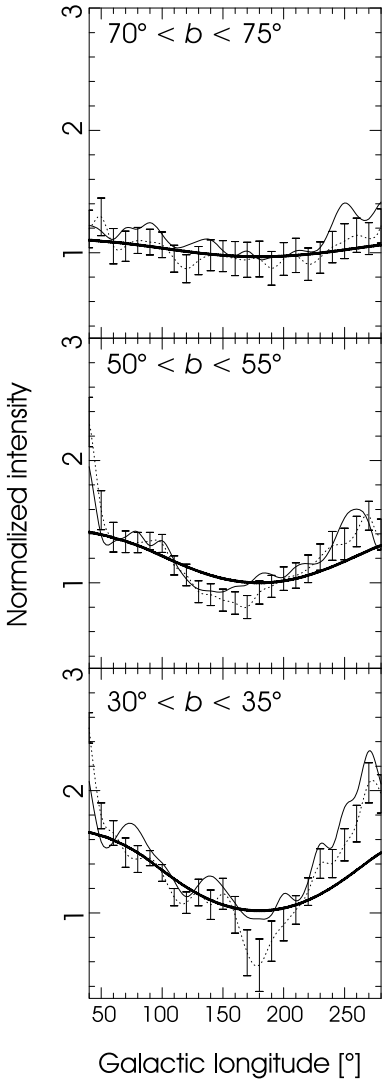

Fig. 33: *Distribution of the normalization of unabsorbed Halo intensity in different regions of the northern sky. These regions are stripes with Galactic latitude belonging to the interval shown in the upper part of the three diagrams. The constraint in Galactic longitude (*$280\circ > l > 40\circ$*) is given to avoid the contamination produced by the North Polar Spur. The dotted line shows the data of the ROSAT R4 band with the corresponding error bars. For clarity, we omit the error bars for R2 (thin solid line) which are about 50% of those of R4. The thick solid line represents the prediction for the normalized X-ray intensity of the Dark Matter Halo by Kalberla (2003) for the region of interest. The deviation present in the lower diagram at* $240^\circ \geq l \leq 280^\circ$ *is a* δ-positive *region (see Sect. 5.5) associated with the outer parts of Loop I. The influence of the underestimation of the absorber column density towards the Lockman window (Kappes et al., 2003) shows up at* $l \simeq 135^\circ$ *in the middle diagram (see also* δ-negative *regions in Sect. 5.5)*

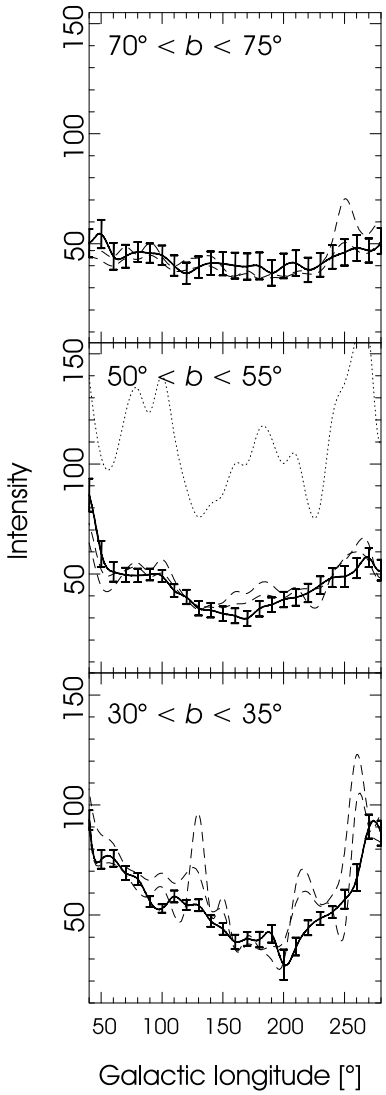

Fig. 34: *ROSAT R4 intensity in the same manner as in Fig. 33. The solid line is the observed* unabsorbed Halo intensity *(see Sect. 5.4). The dashed lines are the predictions calculated for the other energy bands with* $T_{\mathrm{HALO_A}} = 10^{6.15}\,\mathrm{K}$. *For clarity, we show only the predictions of R1 and R2 and only the error bars corresponding to R4. In order to illustrate the sensitivity to plasma temperature of the method applied, we show the results for* $T_{\mathrm{HALO_A}} = 10^{6.3}\,\mathrm{K}$ *with the dotted line in the middle panel. We see, that a small variation in temperature yields major changes in the predictions of the models.*

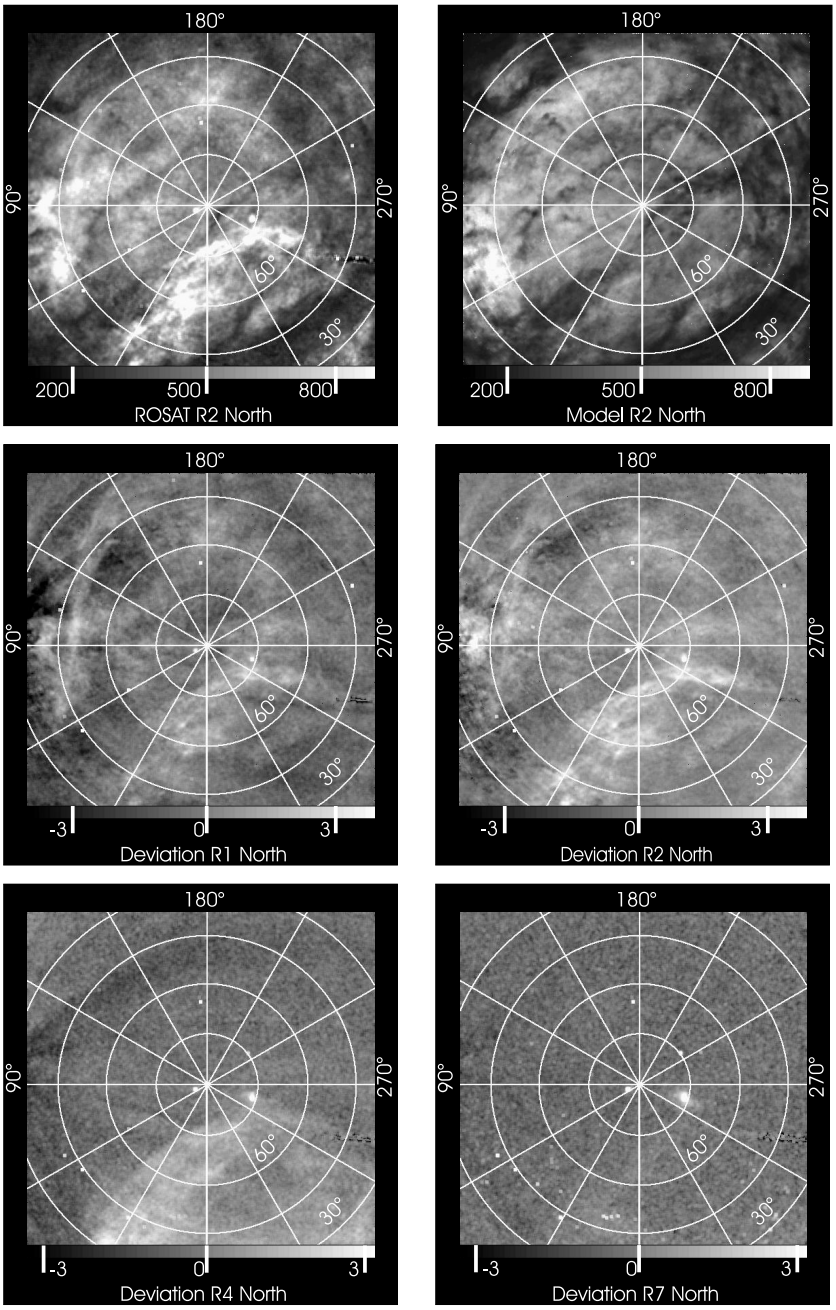

Fig. 35: **Top:** *The RASS in the R2 energy regime (left) and model image (right) for the northern sky omitting the Galactic Plane which is opaque to soft X-rays. The units are in both cases* $10^{-6}\,\mathrm{cts\,s^{-1}\,arcmin^{-2}}$*. The model is built using the best fit parameters found with the method presented in this work. There is a good agreement between model and observation. Only one prominent structures in the left panel is not present in the model at* $(l,b) \simeq (0°, 65°)$*. This can be immediately identified with an additional extended X-ray source: the North Polar Spur.* **Middle and bottom:** *Maps of the deviation of our model with respect to the ROSAT observations in four different energy bands.* δ-positive *regions are in white and* δ-negative *regions in black (see Sect. 5.5). In the intermediate and high ROSAT energies (bottom), we can identify the two significant deviation regions detected as the North Polar Spur and the Virgo cluster (*$(l,b) \simeq (0°, 65°)$ *and* $(l,b) \simeq (265°, 75°)$*, respectively). The deviation maps of the low energies (top), show a richer structure due to the imprecision in our knowledge of the shape of the LHB (see Sect. 5.6), additional sources and, in some cases, associated to uncertainties in the position of IVCs and HVCs like at* $(l,b) \simeq (180°, 50°)$ *or* $(l,b) \simeq (90°, 45°)$ *(see Sect. 6.1).*

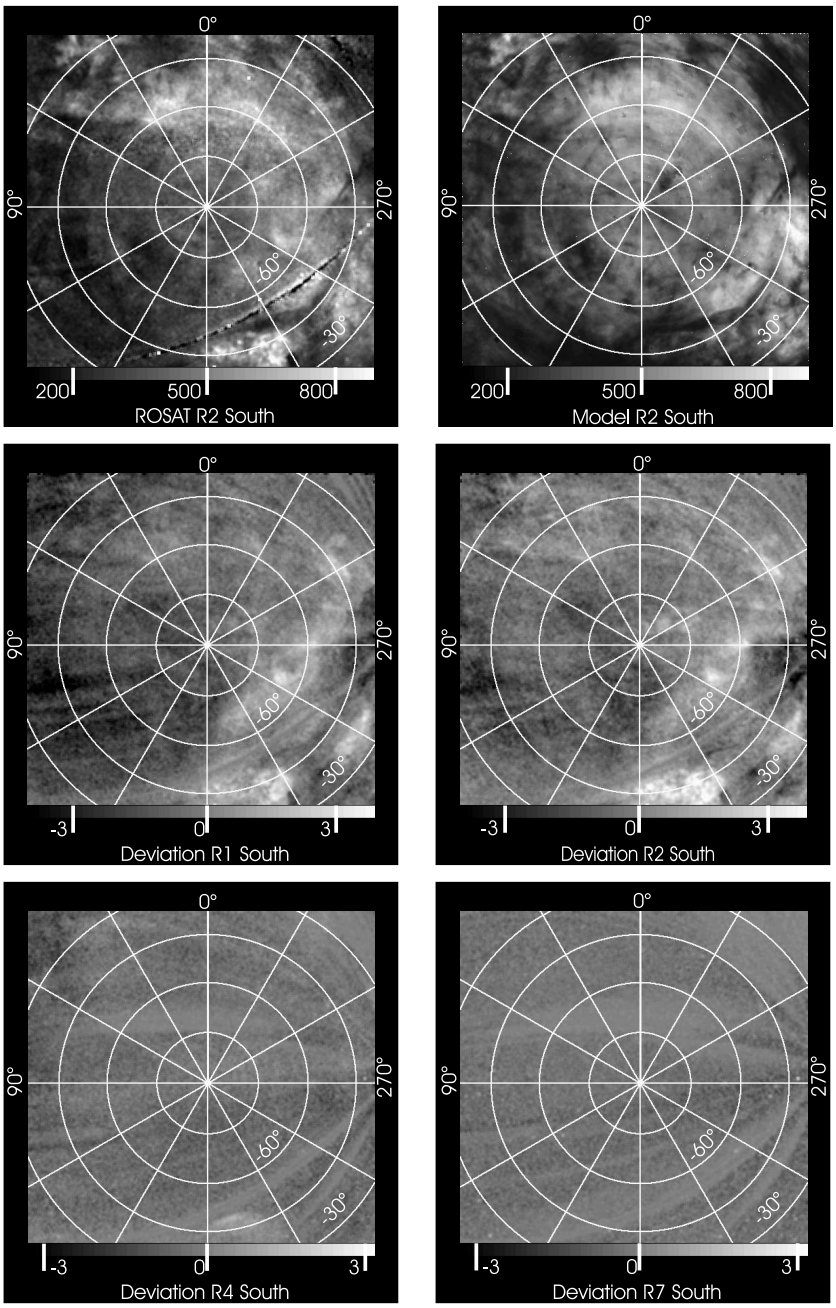

Fig. 36: **Top:** *Observation (left) and best fit model (right) in the same units as in Fig. 35 for the south Galactic sky. Only the excess emission of the Orion star forming region at* $(l,b) \simeq (200°,-40°)$ *can be detected as a significant difference between both maps by a visual inspection.* **Middle and bottom:** *Deviations of our model with respect to the ROSAT observations in the same manner as in Fig. 35. The effect of the Orion star forming region is clearly visible in the deviations for R1 and R2 and points to a hot gas with temperature* $T \simeq 10^{6.05}\,\mathrm{K}$*. In the higher energies (bottom), we identify the influence of the RASS exposure maps as "stripes" converging at* $(l,b) \simeq (270°,-30°)$*.*

6 Applications of the Model for the SXRB

In Chap. 5 we presented a model for the SXRB with very good precision for the emissions of the Galactic X–ray Halo and the extragalactic background. We also have seen that the accuracy of the ROSAT data does not permit a very detailed investigation of the shape of the LHB. Here we will assume the validity of the previous results and search for alternative origins for the δ*-positive* and δ*-negative* present in Figs. 35 and 36. Some cases of those can be easily identified as additional sources (e.g., the North Polar Spur) but most of them are related to inadequate assumptions on the structure of the material involved in the photoelectric absorption of the SXRB.

6.1 $N_{\rm HI}$ as variable

Up to now, the amount of photoelectric absorption caused by the ISM was determined using a fixed radial velocity interval ($|v_{\rm LSR}| < 125\,{\rm km\,s^{-1}}$) for the HI. This selection assumes *a priori* that all intermediate–velocity and a significant fraction of the high–velocity gas is located *in front of* the Galactic X-ray Halo. Thus, this gas would attenuate the X–ray emission of the Halo (see Sect. 5.2.3). This assumption is also not entirely consistent with the constraints found in the literature for the distances to some HVC complexes – for A, C and M see Tab. 4 – which, making use of absorption line studies, locate this high–velocity gas outside the Galactic X-ray Halo, at distances of several kpc (Wakker & van Woerden, 1997; Woerden et al., 1999). Here, we present an independent method to constrain the distances to the HVC complexes based on our models of the SXRB.

It is important to note that we can make this kind of study only for a large angular scale. This is because the precision of the data (both angular resolution and sensitivity) do not permit detailed investigations towards the edges of the individual HVCs. In other words, if an HVC produced an attenuation in the X–ray Halo emission, the borders of the shadow would not be very "sharp" in our dataset. Therefore, only a rough approximation of the (l,b) distribution of the HVC complexes will be used in this Chapter. We obtain these distributions by subtracting from the total $N_{\rm HI}$ map: 1) The gas whose $|v_{\rm LSR}|$ is in agreement with the velocity given by the Galactic rotation and 2) The gas whose radial velocity is in clear disagreement with the values given in the literature (see Tab. 4) for the corresponding HVC complex. For example, in the direction towards complex M ($l \simeq 180^\circ$) we eliminate the gas with a velocity of $|v_{\rm LSR}| < 25\,{\rm km\,s^{-1}}$

corresponding to Galactic rotation and, due to the negative radial velocity of complex M, we also eliminate from the total $N_{\rm HI}$ map the gas with $v_{\rm LSR} > 25\,{\rm km\,s^{-1}}$.

Also the limitations in the precision of the data affect the fields chosen for the HVC complexes shown in Figs. from 37 to 40. We have to consider that, on one hand, the field must include a significant "clean " area (outside the HVC complex) in order to get good normalizations for the models and, on the other hand, the corresponding HVC complex has to cover a significant part of the field to ensure acceptable statistics when changing the conditions for the complex in the models. Additionally, to achieve a fine tuning of the models reduced angular sizes for the fields are desirable (see Sect. 5.3 for the investigation local fields) because smaller sizes minimize the effect of the uncertainties in the shape of the LHB and the intensity distribution of the Galactic X–ray Halo ($I_{\rm HALO}(l,b)$). In practice, we select fields with angular radius of about 20° and towards the borders of the HVC complexes where at least 60% of the field is not covered by the gas of the HVC complex. With an appropriate choice of the fields, we can begin the individual investigation of each HVC complex using our models for the SXRB.

In the case of the field towards HVC complex A (see Fig. 37), the velocity of the HVC complex gas ($-200\,{\rm km\,s^{-1}} \leq v_{\rm LSR} \leq -130\,{\rm km\,s^{-1}}$) is not included in the radial velocity interval ($|v_{\rm LSR}| < 125\,{\rm km\,s^{-1}}$) that we have used for our models until this point. This means that the neutral gas belonging to HVC complex A has been supposed to be located outside the Galactic X-ray Halo in the construction of our models, in agreement with previous works that conclude $4\,{\rm kpc} \leq d \leq 10\,{\rm kpc}$ (Woerden et al., 1999). In order to test this conclusion, we constructed models in which it is assumed that HVC complex A is located inside the Galactic X-ray Halo. The corresponding deviation maps show δ-*positive* regions of the order of $\delta \simeq 1$ (contours in the upper panel of Fig. 37) that are well aligned with the structure of HVC complex A. Since these regions disappear for the models with complex A located outside the X-ray Halo, our results are in agreement with the lower limit for the distance by Woerden et al. (1999). However, we have to note that due to the relatively low column densities of complex A (see Tab. 6), the δ-*positive* region created by considering complex A inside the Galactic X–ray has a low statistical significance. Because of that, we do not present the histograms of δ for this region in contrast to the cases of complex C and M (see Fig. 40).

In Fig 38 and in the lower panel of Fig. 40, we see the results for the region toward HVC complex C ($-140\,{\rm km\,s^{-1}} \leq v_{\rm LSR} \leq -100\,{\rm km\,s^{-1}}$). Of the three cases investigated here, complex C has the largest area filling factor and its investigation consequently yields the best statistical significance of all. In fact, we can see in the corresponding histogram that the positive *wing* ($\delta \simeq 1.5$, solid arrow) present in the model when the gas of complex C is considered to be inside the X-ray Halo, is not present anymore when we calculate the model under the assumption that complex C is located outside the Halo. With this assumption we achieve an improvement of about 15% in the dis-

persion of the model with respect to the observations. This means that, like in the case of HVC complex A, our model for the complex C region is consistent only in the case that the high–velocity gas is situated outside the Galactic X-ray Halo. This result is also confirmed by the graphical approach illustrated in Fig. 38. There, the δ*-positive* regions obtained with the gas inside the Halo of the upper panel coincide in general with the position of the gas (white contours). Most of the δ*-positive* regions vanish by assuming that the gas is outside the X–ray Halo and does not "shadow" the Galactic X–ray emission.

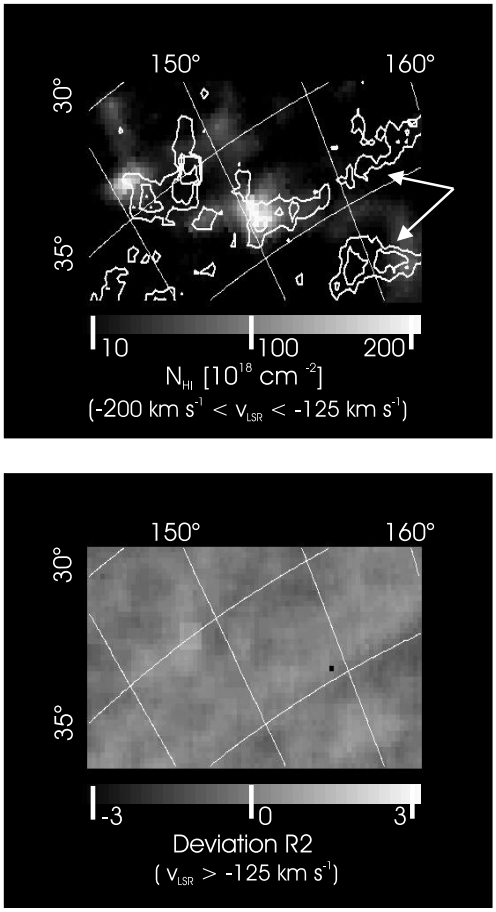

Fig. 37: **Upper:** *Detail of the* HI *column density distribution of the high–velocity material belonging to HVC Complex A. The white contours show the levels of deviations* δ *0.4, 0.8 and 1.2 in a model constructed with HVC complex A located* inside *the Galactic X-ray Halo. The white arrows indicate the* δ-positive *regions still present in the models with complex A* outside *the Halo. The structures at* $(l,b) \simeq (143°, 37°)$ *correspond to the outer regions of complex C.* **Lower:** *Deviation map of the same region in the upper panel calculated with the material corresponding to complex A and C located outside the X-ray Halo of the Milky Way. The square structure at* $(l,b) \simeq (148°, 35°)$ *originates from an insufficient source subtraction for this position in the RASS. The map shows a good agreement between model and observation.*

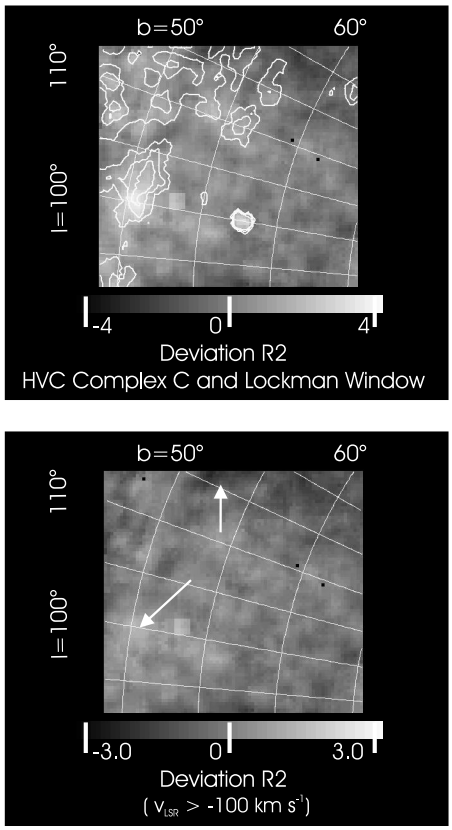

Fig. 38: **Upper:** *Deviation map of a model for the R2 band where the material belonging to HVC complex C has been assumed to be located inside the Galactic X–ray Halo. The white contours mark the gas of complex C and correspond to 4, 6 and 8*$\cdot 10^{19}\,\mathrm{cm}^{-2}$ *in* HI *column density. The* δ-positive *regions and the material of complex C are well aligned.* **Lower:** *Deviation map of the same region in the upper panel calculated with the material corresponding to complex C located outside the Galactic X-ray Halo. Both maps have been chosen to include the eastern part of the Lockman Window (*δ-negative *region marked with the upper arrow). The lower arrow marks an excess emission region reported by (Kerp et al., 1999)*

After finding the best fit HI distribution for the complex C region, we still detect an excess of emission ($\overline{\delta} \simeq 1.4$) in some small regions. These are marked by the lower white arrow in Fig. 38 and the solid arrow in the upper histogram of Fig. 40. This excess emission detected in our study, may be associated to shocks in the high–velocity material as it has been noted by Kerp et al. (1999).

The results of our models for the region toward HVC complex M are illustrated in the upper panel of Fig. 40 and in Fig. 39. Like in the cases of complex A and C, the inclusion of the material of complex M ($-120\,\mathrm{km\,s}^{-1} \leq v_{\mathrm{LSR}} \leq -90\,\mathrm{km\,s}^{-1}$) in the absorbing column density of our models generates *δ-positive* regions in the deviation maps that vanish if the material is located outside the Galactic X-ray Halo. One interesting feature in the histogram of Fig. 40 corresponding to complex M is

the δ-*positive* region around $\bar{\delta} \simeq 1.3$ (solid arrow). As we will see in Sect. 6.3, this deviation region may be related to the emission of the WHIM.

Finally, it is important to note that the presented method to give constraints to the distances to the HVC complexes can be used iteratively with the method of Chap. 5 to investigate the Galactic Halo X–ray emission in order to improve the statistics of our models. In fact, the best fit results presented in this work have been obtained by applying such an iterative method. This becomes even more important for the investigation of smaller scale regions, like in Sect. 5.3. In that case, a much better statistical quality can achieved by the fits, mainly because of the smaller uncertainties in the spatial variations of the intensities of the LHB and the Galactic X–ray Halo.

6.1.1 Lower Limits to the Distances to the HVC Complexes

In this Section, we present some simple calculations to derive *numerical* constraints to the distances to the individual HVC complexes. This are based in calculating the proportion of the X–ray Halo that must be located behind a cloud in order to produce an intensity contrast with respect to an *off* position larger than the precision of the X–ray data. In other words, we search for the distance from the Sun in a given line of sight, at which a certain $N_{\rm HI}$ (from a HVC complex) would produce a shadow in the Galactic X–ray Halo emission that can be detected with the precision of ROSAT. For these calculations, the intensity distribution of the X–ray Halo is given by the model by Kalberla (2003) while the mean intensity contrast can be approximated using the mean $N_{\rm HI}$ of the corresponding cloud. A stricter limit can be calculated using the highest column density for the complex (see also Tab. 6). In case of using the highest column density, the obtained limit is restricted to relatively small regions ($r \leq 1^\circ$) in the sky and not to the entire HVC complex. We now develop all these concepts more rigorously.

If X represents the fraction of emission originated behind a ISM cloud compared to the total emission in the corresponding line of sight ($\mathrm{X} = I_{\rm behind}/I_T$, where $I_{\rm behind}$ is the intensity originated behind the cloud and I_T the total intensity of the X–ray Halo in that direction), after correcting for extragalactic background and foreground LHB emission we can write the X–ray intensity observed towards the cloud I_C as:

$$I_C = (1-\mathrm{X}) \cdot I_T + \mathrm{X} \cdot I_T \cdot \mathrm{e}^{-\sigma \cdot N_{\rm HI}} \tag{16}$$

where σ is the effective cross section in the direction of the cloud and $N_{\rm HI}$ its column density. Since the precision of the RASS in the RC band is approximately 10%, the contrast in intensity between the on and off positions of the cloud has to be bigger than 10% for the shadow of the cloud to be detected. Then, using Eq. 16, we obtain:

Tab. 6: *This Table shows the observed maximal (max) and typical (mean) column densities of the HVC complexes A, C and M together with the fraction of hot gas X that has to be situated behind the absorbing material for the cloud to produce a shadow detectable by ROSAT in the RC band (see Sect. 6.1.1). d and $|z|$ represent respectively the lower limits for the distance and height above the Galactic Plane obtained with our method. Note that $|z|$ is unambiguously determined by d and (l,b). The values for d and $|z|$ found in Woerden et al. (1999) (also in Tab. 4) are shown in parenthesis.*

HVC name		$N_{\rm HI}$ $[10^{19}\,{\rm cm}^{-2}]$	X	$d \geq$ [kpc]	$\lvert z\rvert \geq$ [kpc]
A	mean	3	0.43	$2.1\ (4-10)$	$1.1\ (2.5-7)$
	max	5	0.29	3	1.5
C	mean	6	0.26	$3.6\ (\geq 5)$	$2.3\ (\geq 3.5)$
	max	8	0.21	4	2.7
M	mean	4	0.34	$\mathbf{2.1}\ (\leq \mathbf{4})$	$\mathbf{1.8}\ (\leq \mathbf{3.5})$
	max	6	0.26	2.7	2.3

$$\mathrm{X} \geq \frac{0.1}{1-\mathrm{e}^{-\sigma \cdot N_{\rm HI}}} \tag{17}$$

which gives the minimal fraction of the Galactic X–ray Halo that must be located behind an ISM cloud in function of its column density in order to be detectable with the RASS in the RC band. The results of Eq. 17 can be compared with the models for the X–ray emissivity by Kalberla (2003) used in Chap. 5 to obtain the constraints shown in Tab. 6. Concretely, given (l,b) for a cloud, the model for the emissivity distribution provides X as a function of distance. Here, we use the model by Kalberla (2003) in the opposite direction, by searching which distance corresponds to the X obtained with Eq. 17 for the column density of the specific cloud. Following the argumentation presented in this Section, the value obtained for d is a lower limit for the distance to the cloud.

We can summarize this Section as follows: With the method presented in this Section to disentangle the 3-D structure of the Galactic X-ray, we calculate lower limits for the distances to the HVC complexes A and C that are in agreement with the values obtained with line absorption studies, locating both outside the Galactic X–ray Halo.

Our result for complex M (see bold type row in Tab. 6) complements the upper limit to the distance given by (Woerden et al., 1999) and also situates this complex outside the Galactic X–ray Halo but close to its border. This result is also in agreement with the conclusions by Danly et al. (1993) which, by means of absorption line studies towards Halo stars, give a lower limit to the distance to complex M of $d \geq 1.5$ kpc.

6.2 δ-*negative* Regions

There is only one δ-*negative* region of significant size in the north Galactic sky (Fig. 35) that is centered at $(l,b) \simeq (150^\circ, 50^\circ)$. This region points in the direction of the Lockman window, and towards this region the modeled intensity of the SXRB is systematically higher than the observed one. The dashed arrow in the lower histogram of Fig. 40 (with $\delta \simeq -1.5$) shows the effect of the eastern part of the Lockman window on the statistics of the models across the field of towards HVC complex C. This region is also identified in Fig. 38 as the δ-*negative* region marked with the upper white arrow. According to Kappes et al. (2003), an important fraction of the absorber in the Lockman window region (up to 40%) is weakly ionized and, thus, not traced by the HI surveys. This argumentation implies that we have underestimated the absorbing column density in this region and explains the δ-*negative* region in the results of our models. Consequently, in order to construct a model for the radiative transfer in the Lockman Window region, the distribution of the WIM must be also taken into account.

Apart from the Lockman Window, several δ-*negative* regions with a smaller angular size than that of the Lockman Window are present across the deviation maps for the R1 band in both the northern and the southern Galactic sky. In contrast to the Lockman Window, these δ-*negative* regions are in general only detected in the lowest energy bands R1 and R2.

In some cases, these "smaller" δ-*negative* regions may are related to clouds of the MM (see Sect. 4.1.1) like in the Draco Nebula region (see also Fig. 2). In other cases, they may be related to local maxima of the ratio between ionized and neutral absorbing medium. Concretely, if the fraction of ionized medium is large, the value $N_{\rm HI}$ used here may be underestimated like in the case of the Lockman Window. Both possible scenarios indicate that for very detailed investigations of relatively small regions ($r < 10^\circ$), the contribution of the MM and/or of the WIM to the photoelectric absorption may be significant (considering the accuracy of the ROSAT data) and should be taken into account in order to construct reliable models for the radiative transfer of the SXRB through the ISM. For these special regions, the IRAS 100 μm survey and the *Wisconsin H_α mapper* can be used to trace the contributions of the MM and the WIM respectively. However, the systematic use of the IRAS 100 μm data for the entire sky as proposed by Kuntz & Snowden (2000) cannot be accepted because this IRAS survey does not trace the diffuse part of the Galactic absorber. As we have seen in Sect. 4.1 (see, e.g., also Pietz, 1997), this leads to an underestimation of the photoelectric absorption caused by the ISM up to 50% in the high Galactic latitude sky.

6.3 One δ-*positive* Region

One interesting δ-*positive* region in the north Galactic sky is situated close to HVC complex M and marked by the white arrows in Fig. 39. The region is composed of two

local maxima in the deviation map of the R2 band that can also be easily identified at the corresponding coordinates in the R1 deviation map and in the R2 RASS map shown in Fig. 35. For the higher energy regimes, no deviation is detected in this region.

The quantification of the detected excess emission can be better done by determining the intensity of the region directly in the RASS and subtracting the background intensity measured in its vicinity, instead of assuming any configuration for the Galactic X–ray emission and absorption, i.e. using any model for the radiative transfer. This approach is also supported by the very homogeneous SXRB intensity distributions observed in Fig. 35 for all energy bands around the region that we discuss. Also the $N_{\rm H\,I}$ is rather homogeneous (see Fig. 30). With these assumptions, we find an approximate excess intensity of $\Delta \mathrm{I}_{\rm R1} \simeq 80 \cdot 10^{-6}\,\mathrm{cts\,s^{-1}\,arcmin^{-2}}$ and $\Delta \mathrm{I}_{\rm R2} \simeq 150 \cdot 10^{-6}\,\mathrm{cts\,s^{-1}\,arcmin^{-2}}$ in the energy bands R1 and R2 respectively.

Making use of the *band–ratios* that were presented in Sect. 5.2.2 in connection to the coupling of the ROSAT energy bands, we can use the estimates for Δ of the two bands with successful detection and, after correction for photoelectric absorption (the absorbing column density amounts to $N_{\rm H\,I} \simeq 11 \cdot 10^{19}\,\mathrm{cm^{-2}}$ in the region), give some rough approximations for the temperature assuming that the emission originates from a thin plasma. We obtain $T \simeq 10^{6.3}$ K. However, the statistical significance of this result is relatively low because: Firstly, the exposure of the RASS towards this direction is about 30% shorter than the mean value, yielding in a larger standard deviation. Secondly, only two energy bands can be used for the analysis which is equivalent to doing spectroscopy only with two data points. A further constraint for the temperature is given by the non–detection in the higher ROSAT energy regimes. With a similar calculation to that used for R1 and R2 above, we infer that at $T \leq 10^{6.5}$ K and with the $N_{\rm H\,I}$ of the region, the R2 intensity observed would imply $\mathrm{I}_{\rm R4} \leq 35 \cdot 10^{-6}\,\mathrm{cts\,s^{-1}\,arcmin^{-2}}$. This is not detectable with an accuracy of $\sigma_{\rm R4} \simeq 40 \cdot 10^{-6}\,\mathrm{cts\,s^{-1}\,arcmin^{-2}}$ towards this region. The same argumentation can be applied to R5, R6 and R7. To summarize, the observed band–ratios indicate a temperature below $10^{6.5}$ K with a more probable value around $10^{6.3}$ K.

Kravtsov et al. (2002) present simulations for the structure formation and evolution in the Local Universe in which the emission of the WHIM is modeled via the positions and masses of nearby galaxies. In order to search for an explanation for the *δ-positive* region discussed here, we compared our results with the predictions by Kravtsov et al. (2002). In Fig. 6 of their paper, a normalized X–ray intensity map of the WHIM is shown, where two of the local maxima are coincident in direction and size with the deviation structure presented here. The temperature for these two maxima is given if Fig. 5 of Kravtsov et al. (2002) and corresponds to an interval $10^{6.3}\,\mathrm{K} \leq T \leq 10^{6.5}\,\mathrm{K}$, which is in agreement with the approximate value obtained with the X–ray data.

But why is be the X–ray emission of the WHIM detected only in this direction, when there are other local X–ray intensity maxima with higher “peaks” and temperatures in the Figs. shown by Kravtsov et al. (2002)? This is based in several facts. First, the

observed intensities are beyond the sensitivity of the RASS in some regions of the sky (see Fig. 15 of the RASS exposure map), and in others they are clearly dominated by additional sources of contamination, like towards the North Polar Spur. Second, among the remaining directions, the δ-*positive* region discussed here ($(l,b) \simeq (180^\circ, 50^\circ)$) is located very close to the absolute minimum of Galactic Halo intensity. Since the contribution of the extragalactic background can be safely considered infinitely isotropic, the region corresponds to a minimum in background intensity, enabling the detection of fainter sources. Third, other local X–ray intensity maxima present in the Figs. by Kravtsov et al. (2002) which are close to the region of interest, are associated to a higher temperature ($10^{6.8}$ K $\leq T \leq 10^{7.0}$ K). Therefore, their bulk emission would be in a higher energy regime where the sensitivity of the RASS is significantly lower. This would prevent a successful detection.

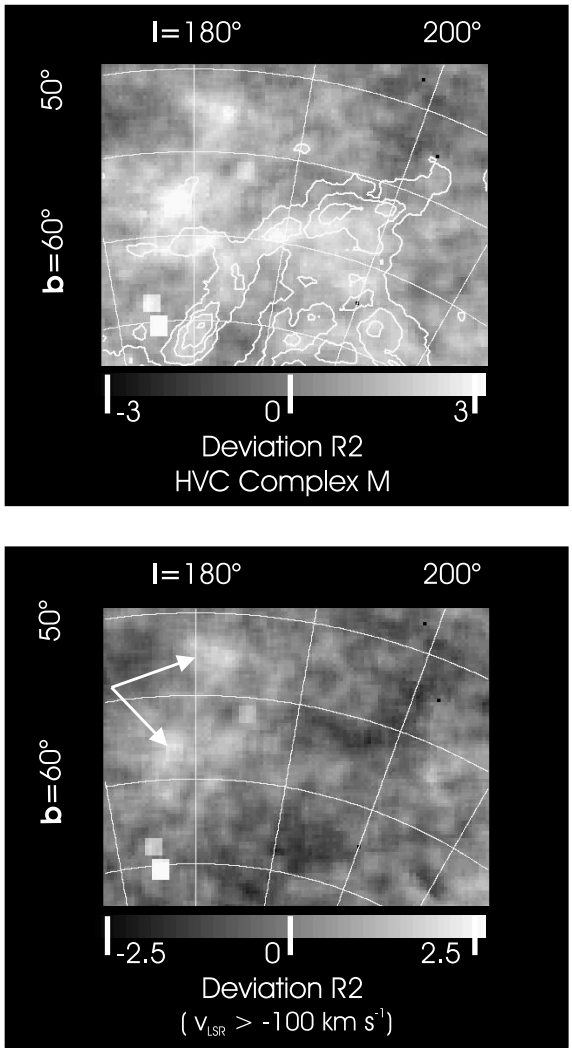

Fig. 39: **Upper:** *Deviation map of towards the complex M region in a model where the high–velocity material is located inside the Galactic X–ray Halo.* $N_{\rm HI}$ *contour levels at 2, 4 and* $6 \cdot 10^{19}\,{\rm cm}^{-2}$ *are also shown. Like in Figs. 37 and 38, the* δ-positive *regions and the material of HVC complex M are, in general, well aligned.* **Lower:** *Deviation map of the best fit model with the gas of complex M assumed to be outside the X–ray Halo. Note, than this map seems more structured than the previous ones (Figs. 37 and 38) because here we have chosen the lowest cut levels for the deviation. This is in order to identify more easily the excess emission regions marked with the arrows and which may be related to the X–ray emission of the WHIM (see also Sect. 6.3).*

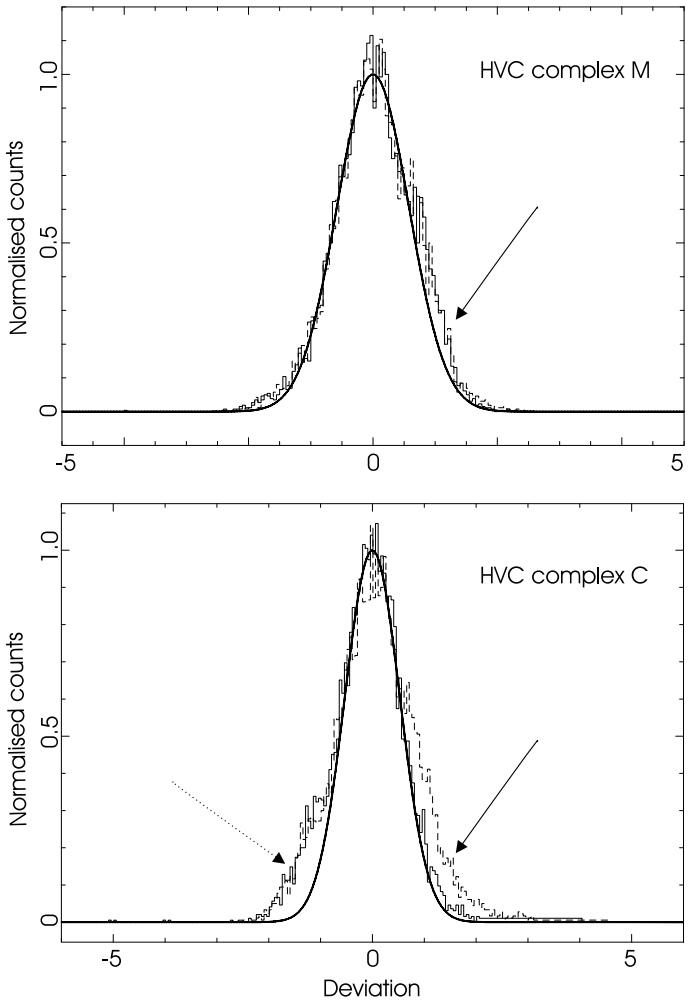

Fig. 40: *Normalized histograms of the model deviation δ toward the regions of the HVC complexes indicated in the upper–right part of the diagrams. The thin solid lines correspond to the best fit models where the high–velocity material is located* outside *the Galactic X-ray Halo, while the dashed lines are obtained with models with this gas* inside *the X-ray Halo. The thick lines show the density function of $N(0, 0.56)$ and $N(0, 0.53)$ distributions for complex M and C respectively. The solid and dashed arrows indicate the effect of δ-*positive *and δ-*negative *regions respectively (see Sects. 6.3 and 6.2).*

7 Data Reduction for Observations of the ISM with XMM–Newton

The investigation of low surface brightness sources in X–ray astronomy requires very precise data reduction methods, as already discussed in Chap. 3. In the case of the XMM–Newton observatory, several authors (Lumb et al., 2002; Marty et al., 2003; Read & Ponman, 2003; Katayama et al., 2004) have addressed the data reduction problem originated in that some of the standard data analysis tools, which are suitable for the study of bright X–ray sources, are not sufficient for faint and extended sources. Most of the effort to improve the standard data reduction tools has been focused on the development of temporal filters for the mitigation of the so–called *solar proton flares* and minimizing the instrumental noise with high accuracy (see, e.g. Lumb et al., 2002). Read & Ponman (2003) published *background maps* to correct the observations for *vignetting*, which is of special importance for the analysis of extended sources. But the contribution of the cosmic X–ray background, originating from the Local Hot Bubble, the Galactic Halo and the extragalactic X–ray background, has not been systematically treated for XMM–Newton as it has been in case of the ROSAT mission (see, e.g. Chap. 5 Kerp et al., 1999; Snowden et al., 1998; Pradas et al., 2003). Because XMM–Newton is, in principle, able to detect very faint signals significantly, all systematic effects must be well understood and reliable methods to eliminate their contributions have to be developed. All this effort should lead to an *absolute calibration* of the X–ray data which could be applied to allow the study in detail of very weak extended sources (e.g., warm/hot intergalactic medium (WHIM), X–ray halos of nearby galaxies).

In this Chapter, we present our newly developed data reduction method for the analysis of diffuse X–rays observations with the XMM–Newton EPIC MOS detectors. In order to develop this method, we made extensive use of the XMM–Newton Science Archive[11] and carried out the *in–flight* background analysis for XMM–Newton with largest accumulated exposure time at present (about 1.4 Ms). In this work, we focus on the EPIC–MOS instruments on board XMM–Newton, in the *FullFrame* mode and with the *medium* filter (see Sect. 3.3), although the developed method can be straightforwardly applied to the remaining instruments, filters and modes.

We also report on an overestimation in the measured X–ray intensity in the softest energy regime ($0.2\,\mathrm{keV} \leq \mathrm{E} \leq 0.5\,\mathrm{keV}$) for CCDs 2 and 5 of the EPIC–MOS 1 camera. These two CCDs occasionally show up with up to a factor of two higher X–ray background intensity than the other CCDs. In Sect. 7.4 of the present Chapter, we will

[11] *http://xmm.vilspa.esa.es/external/xmm_data_acc/xsa/index.shtml*

see that about 15% of the observations in our database are affected by this effect in CCD 5. In case of CCD 2, more than 50% of the observations present contamination detectable with a first visual inspection of the data.

7.1 XMM-Newton Raw and Calibrated Data

The database that we have used for this investigation is separated in two types of observations. On one hand, we make use of as many public XMM–Newton Science Archive observations as possible (see Tabs. 7 and 8) in order to have a significant sample of the general response of the instruments in a large variety of configurations (e.g,. high and low background levels). On the other hand, we make use of a set of own observations (see Tab. 9) in selected directions in the sky for which there is a special importance of the contribution of the XRB. For example, a high contrast region towards the Draco Nebula area presented in Fig. 2 is included in observation 0110660801.

7.1.1 Observations from the XMM–Newton Science Archive

Using the XMM–Newton Science Archive, we searched for all observations available in which the EPIC MOS cameras worked in the *FullFrame* mode. This choice is based on our interest to develop tools for investigating the diffuse soft X–ray emission ($E \leq 2\,\mathrm{keV}$) which requires the use of the largest detector area possible. Also the Medium filter was chosen because the study of the XRB involves the use of *bright* observations in the sense that they present a high level of X-ray background intensity (Kerp et al., 1999; Kappes et al., 2003).

In order to maximize the background signal of the sample, observations with very bright point sources, which are detectable by first visual inspection of the data, were excluded from our data selection. We also excluded observations with less than 8 ks exposure time. This criterion assures an expected background rate of at least $1\,cts\,arcmin^{-2}$ for the soft energy regime, defining a set with acceptable statistical significance. The derived value of 8 ks is based on the ROSAT all–sky survey data, taken as a first estimation of the XRB level towards the fields of interest. In fact, the minimal X–ray intensity for the XRB among the observations in Tab. 7, 8 and 9 of $119 \cdot 10^{-6} cts\,s^{-1} arcmin^{-2}$ observed by ROSAT in the R2 energy band corresponds to $\simeq 120 \cdot 10^{-6} cts\,s^{-1} arcmin^{-2}$ in one EPIC MOS detector ($E \leq 2\,\mathrm{keV}$) with the *medium* filter ($1\,cts\,arcmin^{-2}$ expected in about 8 ks). Note, that the differences in effective area between both observatories must be taken into account for this calculation.

Tab. 7: *Summary of the observations extracted from the XMM–Newton Science Archive for our investigation of the XMM–data reduction. The fourth column shows the total column densities derived from the newest all–sky stray–radiation corrected 21–cm line surveys (Kalberla et al., submitted). The total integration time is* $t_{\rm total} \simeq 1.4\,$Ms *(sum of Tabs. 7, 8 and 9) and the effective time after solar proton flare filtering amounts* $t_{\rm eff} \simeq 1.1\,$Ms

Observation ID	Galactic coordinates		$N_{\rm HI}$	MOS1		MOS2	
	l [°]	b [°]	$[10^{20}\,{\rm cm}^{-2}]$	$t_{\rm tot}$ [ks]	$t_{\rm eff}$ [ks]	$t_{\rm tot}$ [ks]	$t_{\rm eff}$ [ks]
0000110101[2,5]	149.23	4.13	36.0	32.3	13.6	32.3	13.4
0007420701	311.10	-0.41	210.4	12.1	14.8	12.1	9.6
0007420801	310.89	-0.00	207.2	13.0	9.9	13.0	10.3
0007421001	310.89	0.83	182.1	12.0	21.8	12.0	19.1
0007421901[2]	311.31	0.83	177.0	10.6	8.4	10.6	8.1
0007422001	311.52	1.24	145.6	10.0	9.8	10.0	6.9
0007422101	311.31	1.66	118.8	11.8	9.0	11.8	6.5
0007422201	311.52	2.08	83.4	11.8	13.6	11.8	10.4
0007422301	311.31	2.49	91.2	15.0	13.4	15.0	12.5
0021740101[2,5]	188.46	48.65	0.9	34.3	21.1	34.3	23.5
0022140101[2]	336.42	-0.21	196.6	15.9	15.7	15.9	14.9
0022740101[2,5]	149.34	53.14	0.6	83.4	45.3	83.4	45.8
0022740201[2,5]	149.34	53.14	0.6	63.9	64.0	64.0	63.2
0022740301[2,5]	149.34	53.14	0.6	38.0	32.3	37.9	34.7
0026340201[2,5]	246.22	39.89	3.8	19.1	10.6	19.1	10.7
0026340301	140.27	43.60	3.1	24.0	19.9	24.0	20.6
0032140201	82.72	-45.57	3.8	12.5	8.3	12.5	7.5
0032940101	357.27	-4.87	25.9	18.3	15.1	18.3	17.5
0046940401[2,5]	216.42	45.50	2.7	15.0	14.5	15.0	14.4
0050940101	1.10	-3.87	29.3	24.0	16.1	24.0	16.1
0050940301[2]	0.62	-8.00	13.7	13.5	8.6	13.5	8.9
0051610101[2]	345.03	-27.74	3.9	22.0	17.5	22.0	17.5
0052140201[2,5]	174.77	68.49	2.1	40.6	34.4	40.6	34.1
0058940101	137.58	35.54	1.7	27.8	27.8	27.8	27.8
0058940301[2]	319.80	26.44	5.5	19.3	18.6	19.3	19.1
0067340201[2]	350.06	-10.00	9.5	14.6	10.8	14.6	10.7
0070340301[2]	185.26	65.49	2.9	31.4	9.5	31.5	9.9

[2,5]: intensity enhancement in EPIC MOS1 CCD 2 and 5 respectively (see Sect. 7.4)

Tab. 8: *Table 7 continued*

Observation ID	Galactic coordinates		$N_{\mathrm{H\,I}}$	MOS1		MOS2	
	l [°]	b [°]	$[10^{20}\,\mathrm{cm}^{-2}]$	t_{tot} [ks]	t_{eff} [ks]	t_{tot} [ks]	t_{eff} [ks]
0070341201	97.09	42.60	1.6	22.2	21.5	22.2	17.4
0079570201[2,5]	234.55	-10.14	19.1	47.6	33.7	47.6	33.2
0082140301	241.39	64.21	2.0	32.9	31.0	32.9	30.9
0083950101[2]	161.47	-13.63	13.7	27.3	19.6	27.3	18.6
0085640201[2,5]	152.53	42.89	3.1	34.4	26.3	34.4	30.6
0092800201	165.81	36.23	4.2	93.8	66.4	93.7	69.1
0092970201	279.17	-64.53	1.8	13.6	10.8	13.6	10.4
0093640701[2]	348.20	-65.23	1.4	20.0	15.2	20.0	15.8
0093640901	138.23	10.58	32.3	9.8	9.9	9.8	7.3
0093670501	347.33	-0.49	148.1	14.1	14.7	14.1	13.3
0100640101[2,5]	122.83	22.47	6.2	43.3	34.7	43.3	35.4
0102640201	133.80	-30.99	13.4	17.1	15.6	17.1	14.2
0104460301[2]	20.06	0.00	162.0	12.0	9.0	12.0	9.6
0109110101[2]	297.62	0.33	132.0	76.0	66.1	76.0	62.6
0111120201[2]	353.07	16.55	12.3	32.8	22.7	32.8	23.1
0112190101	162.85	-34.83	8.8	13.4	11.7	13.4	24.0
0112190201	155.21	75.31	2.6	14.0	11.2	14.0	11.6
0112190401[2]	6.68	43.09	4.4	14.4	13.8	14.4	13.6
0112220101[2]	309.16	14.97	8.2	40.0	35.1	40.0	36.8
0112500101	111.64	31.93	4.1	25.4	24.7	25.4	25.4
0112970201[2]	0.93	0.08	122.2	17.4	16.3	17.4	16.0
0112970701	359.61	-0.04	124.1	23.9	21.4	23.9	23.6
0129320801	270.21	-51.63	1.1	10.0	7.8	10.0	2.1
0135740901[2]	21.06	0.34	188.2	11.9	9.4	11.9	8.9

Tab. 9: *Summary of of our sample of pointings performed with XMM–Newton (see also Tab. 7). The directions of the pointings have been specifically selected to study the contribution of the SXRB as seen by XMM–Newton.*

Observation ID	Galactic coordinates		N_{HI}	MOS1		MOS2	
	l [°]	b [°]	$[10^{20}\,\mathrm{cm}^{-2}]$	t_{tot} [ks]	t_{eff} [ks]	t_{tot} [ks]	t_{eff} [ks]
0110660301[T]	125.05	30.50	8.2	8.9	6.7	9.0	6.8
0110660401	165.17	66.58	3.3	13.2	10.7	13.2	13.1
0110660601[2]	95.03	38.98	2.6	16.1	20.1	16.1	19.6
0110660801[2]	91.31	37.03	2.3	12.2	18.7	12.2	18.7
0110661601[T]	125.05	30.50	8.2	10.0	6.7	10.0	6.9
0110661701[2]	153.29	39.33	6.4	11.2	3.1	11.2	9.8
0110662401[2]	87.95	36.33	2.5	8.7	10.8	8.7	12.0
0110662501[2]	90.99	41.99	1.8	12.6	10.6	12.6	9.7
0110662601[2,T]	90.81	37.97	1.7	11.4	8.8	11.4	8.9
0110662701[2]	88.93	37.12	1.9	9.7	13.8	9.7	14.5

[2,5] like in Tab. 7

[T] *marks observations performed with the Thin filter*

7.1.2 Selected Fields for the Investigation of the XRB

Tab. 9 shows a selection of fields of interest where the RASS revealed large intensity contrasts in the SXRB (X–ray shadows of Chap. 5). Some additional fields, where no attenuation of the Galactic X–ray Halo emission by the HI distribution was detected by the RASS (e.g. HVC complexes), are also included in the sample in order to test the validity of the methods results. All fields were observed with an accumulated integration time of at least 10 ks to assure good photon statistics (see above). These fields are also included in our study of the *proton flare filtering* and *vignetting* of in XMM–Newton (see following Sects.).

With the two subsets presented in this Section, we accumulated the largest database to the present for the kind of investigations presented here (see Tabs. 7, 8 and 9). The observations were calibrated with respect to the calibration database synchronized on October 24, 2002. For that purpose, we use the standard SAS 5.3.3 tasks grouped in the *pipeline* procedure called *emchain* (see Sect. 3.3.3). Further processing of the so produced *calibrated event lists*, was performed using a combination of SAS 5.3.3 and self–developed software (see Sect. 7.2).

Tab. 10: *Selected XMM-Newton energy bands*

Band	E_{min}[KeV]	E_{max}[KeV]
B1	0.2	0.5
B2	0.5	1.0
B3	1.0	2.0
B4	2.0	5.0
C1	0.2	5.0
C2	5.0	8.0
C3	8.0	12.0

7.2 Data Reduction

For the investigation of diffuse X-ray emission, it is necessary to have an *absolute calibration* of the observations. Therefore, we need a precise knowledge of all contaminating effects in the data. This is even more important in the case of the soft energy regime, since the signal is very faint in comparison to the sources of contamination.

In contrast to the RASS, there is no standard tool to perform such an absolute calibration for faint extended emission for XMM–Newton. There are some problems in the data reduction procedure that require the development of special tools to be solved. For example, Read & Ponman (2003) and Lumb et al. (2002) agree in the necessity for a reliable *solar proton flare filtering*, alternative to the method presented in the *ABC Guide to XMM–Newton Data Analysis*, and propose slightly different methods in order to achieve this goal. Read & Ponman (2003) and Kappes et al., in prep, also deepen in the analysis of the XMM–Newton vignetting and propose methods to overcome the insufficiency of the standard data reduction tools to deal with this effect. In practice, the standard tools produce an artificial enhancement of the intensity at the edges of the detector that can be described as an *inverted tunnel effect* (see Sect. 7.3 and Fig. 43).

Now, we present the method that we developed for the data reduction based on the *in–flight* performance of XMM-Newton, and which has the goal of allowing a reliable study of very faint diffuse emission. We emphasize in the effect of solar proton flares (Sect. 7.2.2) and vignetting (Sect. 7.3) and make use of the largest database for this kind of investigation today.

7.2.1 Selection of the Energy Bands

The first step that we performed is the splitting of the *event lists* in the energy bands compiled in Tab. 10 (see also Tab. 2 for a comparison with the ROSAT energy bands). We focus on the study of soft X-rays. Consequently, we select *three* energy bands in

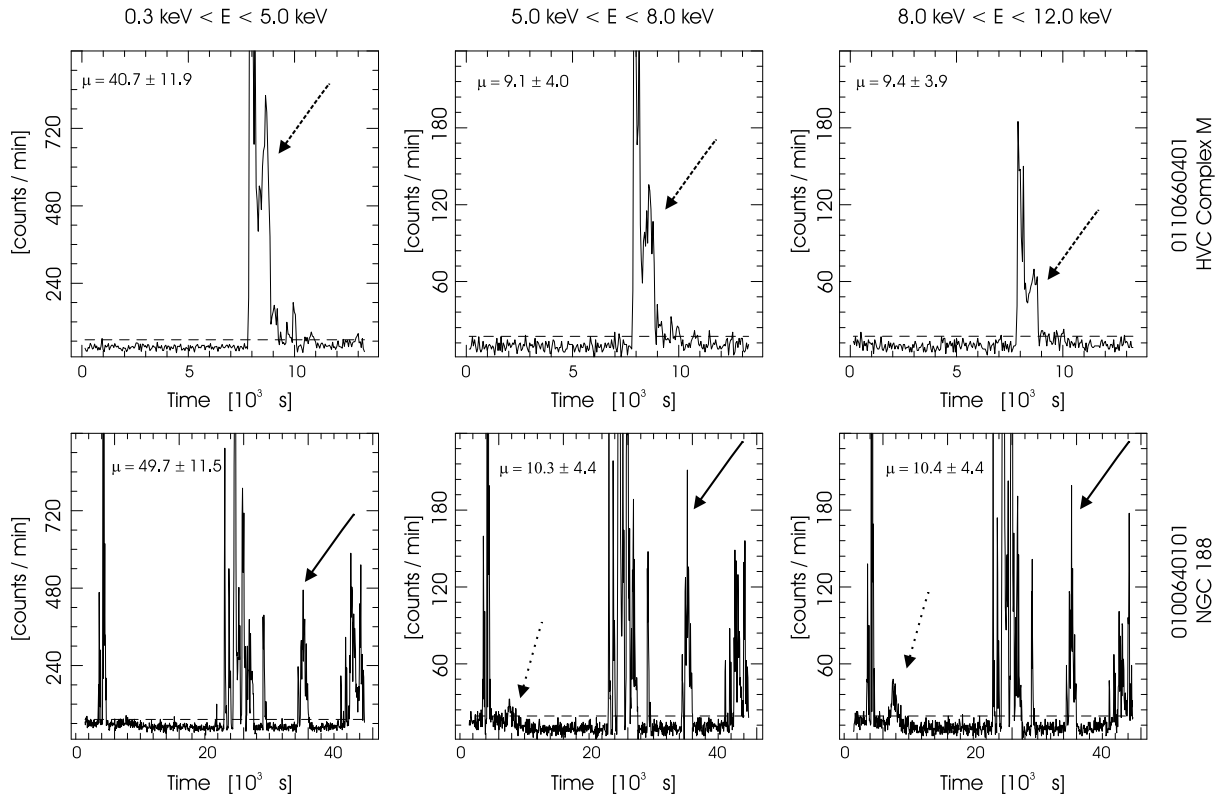

Fig. 41: *Light curves of the EPIC MOS1 camera in the three C1, C2 and C3 energy bands (indicated on top of the panels) for two observations representative of the sample and indicated on the right side of the panels. The dashed lines in each panel marks the two sigma level used for the rejection of contaminated time intervals at the final iteration step (see Sect. 7.2.2). Mean count rates as determined by our programs are shown in the upper parts of the panels as* μ*. The higher count rate for the light curves in the lower panels of this Fig., in apparent contradiction to the background values of Tab. 7, is explained because the curves shown in this figure are calculated with total event lists, which also include the contribution of point sources and not only background events. The arrows (solid, dashed and dotted) point to the effect of three typical solar proton flares with significant differences in their respective spectra (see Sect. 7.2.2).*

the range $E \leq 2\,\mathrm{keV}$, from B1 to B3. We neglect the energy range $E \leq 0.2\,\mathrm{keV}$ because of the uncertainties in the calibration of the data in this energy regime as explained in the *ABC Guide to XMM–Newton Data Analysis* and, e.g., by Read & Ponman (2003). Band B4 covers the energy range dominated by the extragalactic X-ray background (Hasinger et al., 2001). This background is very homogeneous in the B4 energy regime and its homogeneity can be used to test the validity of the data reduction methods applied. If the data reduction methods do not lead to quite homogeneous maps of the extragalactic background (for relatively low integration times), the validity of these methods is questioned. In practice, the extragalactic background can be used as a reference to normalize the intensities of the XRB, as we have done in the investigation with ROSAT data presented in Chap. 5.

Energy bands C1, C2 and C3 are only related to source detection and *proton flare filtering*. The choice of these bands is justified in the following Sect. 7.2.2.

Towards the aim of minimizing the contamination by *photon pile–up* (see Sect. 3.3.2), only single and double events are retained during the energy selection stage. This conservative choice yields a loss in signal that cannot be afforded for studies based on short exposure times (below 5 ks), but it is safe for a sample adding up to almost 1.5 Ms.

7.2.2 Solar Proton Flares

The effect produced by *solar proton flares* (see, e.g. Read & Ponman, 2003) in the observations performed by XMM–Newton is clearly visible in the light curves presented in Fig. 41. We now present a method to filter these events which is a fundamental step for a further analysis of diffuse emission with XMM–Newton data. In Marty et al. (2003) a compilation of alternative methods can be found. However, these methods cannot, in general, be applied in a fully automatic way, in opposition to the method presented here.

When the imaging instruments of the satellite cross interplanetary clouds of electrically charged particles, the count rate increases by up to several orders of magnitude. The low energy protons of these charged clouds are ejected from the Sun (Marty et al., 2003) and show a broad variety of X–ray spectra (see Fig. 41), with particle energies covering the entire energy coverage of the EPIC MOS cameras. It has been proposed (Lumb et al., 2002) that proton flares are composed of several components with different spectra and turn on times. However, Lumb et al. (2002); Read & Ponman (2003) suggest that the most important fraction of the solar proton flares show a hard X–ray spectrum with their dominant contribution at energies higher than $E \geq 10\,\mathrm{keV}$ and, therefore, they focus their methods for proton flare filtering only on the hardest energy regime, corresponding approximately to the C3 band in Tab. 10 . We now revise this suggestion by systematically extending the search for proton flares to all energy bands

noted in Tab. 10. The very broad bands C1, C2 and C3 are used because their high signal–to–noise ratio gives very stable count rates in the phases when the detectors are not being affected by proton flares. Finally, all three bands together cover the entire EPIC MOS energy range without any overlap.

Today, there is no method available to predict the occurrence of solar proton flares. Therefore, their effect can only be corrected in a *post–observation* data analysis. An accurate method of detecting the presence, beginning and end of a proton flare is required to keep the longest usable observation time. We developed such a temporal–filter method based on an iterative algorithm with an user definable σ–level. This σ–level gives the minimal relative contribution of a proton flare to the total count rate necessary to flag out the corresponding time interval.

For each energy band, we compute the mean μ_i and standard deviation σ_i of the count rate and search for observing intervals with a rate exceeding a threshold defined by the user, typically $\mu_i + 2\sigma_i$ or $\mu_i + 2.5\sigma_i$. These *bad time intervals* are flagged and μ_{i+1} and σ_{i+1} are calculated for the remaining observing time. This iteration continues until the difference of the mean values of two consecutive iteration steps stays below the statistical uncertainty of the data ($\mu_i - \mu_{i+1} \leq \sqrt{\mu_{i+1}}$). This "stop condition" is generally fulfilled after less than five iterations. Then, we compute the intersection of the *good time intervals* obtained for the different energy bands and obtain the maximal observing time with *all* bands free of proton flare contamination. Good time intervals with a shorter duration than four minutes are rejected.

After the application of the proton flare detection on the complete event lists, a first source detection (see Sect. 7.2.4 for more details) is carried out. The obtained *source lists* are then used to filter the complete event lists and produce event lists containing only background events. With these new *source filtered* lists used as input, we invoke the proton flare filter a second time. By eliminating the contribution of point sources from the input for this second application of the filter, we mitigate the confusion created by variable sources at the step of calculating the background count rates for each observation. With that, we achieve an important improvement in the sensitivity of the solar proton flare detection.

In the final step, the *filtered event lists* corresponding to the good time intervals are calculated. From the initial 1.4 Ms exposure time included in the total sample, about 1 Ms effective time is left after the application of our filtering of solar proton flares for both the MOS1 and MOS2 cameras (see columns 5 to 8 in Tabs. 7, 8 and 9), although the obtained effective exposure time for MOS2 is in general slightly larger than for MOS1.

The arrows in Fig. 41 (solid, dashed and dotted) indicate typical examples of proton flares. We have chosen the same scale in the vertical axes of the diagrams for the two observations shown in order to allow a direct comparison of the hardness of the three marked flares. The dotted arrow corresponds to the flare with the hardest spectrum,

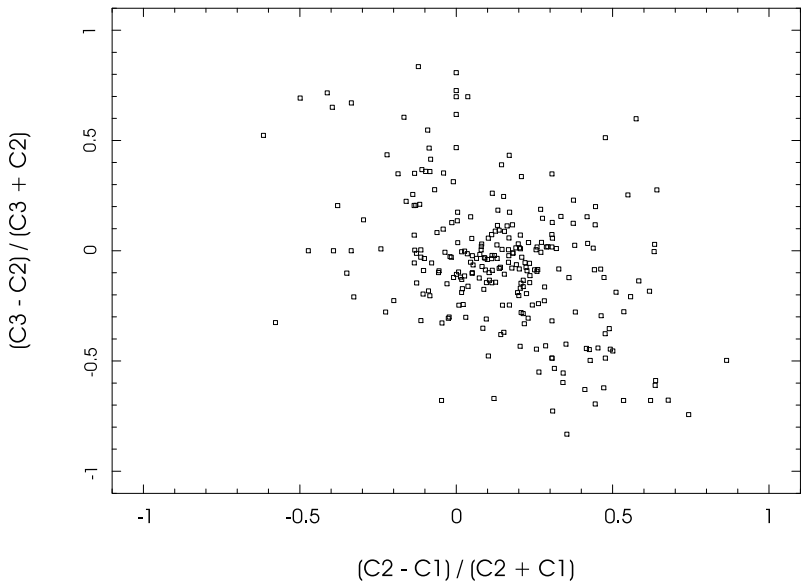

Fig. 42: *Hardness ratios of the solar proton flares detected with our procedure. With the energy bands C1, C2 and C3 we make use of the whole EPIC MOS energy coverage. For clarity, we omit the error bars which vary in a broad range. This is because there are significant differences in the respective intensities of the proton flares represented in the Fig., from very faint (big error bars) to very bright (small error bars). We can see that the hardness ratios of the proton flares are wide spread in all ranges. In contrast to the suggestions by Read & Ponman (2003); Lumb et al. (2002), there is an important fraction of proton flares with* soft *and* medium *spectra.*

with no significant contribution in the lowest energy regime (lower panels in Fig. 41). With a slightly softer spectrum than the previous flare, the solid arrow marks an example of a flare detected in all three energy regimes used. Finally, the dashed arrow indicates a solar proton flare with a very high contribution to C1 and a significantly softer spectrum than the other two flares of this example.

Equipped with our tools to automatically search for solar proton flares, we investigated a large number of XMM-Newton observations (see Tabs. 7 to 9). We found that solar proton flares show up in all XMM–Newton energy regimes with a broad variety of X–ray spectra. The results presented in Fig. 42 indicate that it is not safe to restrict the search for solar proton flares to the high energy regime. This is in opposition to the proposals by Lumb et al. (2002) or Read & Ponman (2003), which suggest a search for proton flares restricted to the $E \geq 10\,\mathrm{keV}$. Our results show that the search for solar proton flares should be extended to all energy regimes as part of the standard reduction of XMM–Newton data.

7.2.3 Other Sources of Contamination

Following Read & Ponman (2003), there are other sources of systematic contamination in the XMM–Newton data that should be taken into account (see also Sect. 3.3.3). Among these, *electronic noise* affects only the low energy regime $E \leq 0.3\,\mathrm{keV}$ and is almost completely excluded from the analysis with our selection of energy bands (see Tab. 10). However, the energy range $0.2\,\mathrm{keV} \leq E \leq 0.3\,\mathrm{keV}$ was not excluded from our energy band selection in order to improve the statistics of the B1 band by increasing its bandwidth. This is justified because the most important part of the *electronic noise* in confined to the $E \leq 0.2\,\mathrm{keV}$ regime *(ABC Guide to XMM–Newton Data Analysis)*. In the $0.2\,\mathrm{keV} \leq \mathrm{E} \leq 0.3\,\mathrm{keV}$ regime, the electronic noise contamination can be neglected in comparison with the contribution of the the XRB to a broad energy band like B1.

The contribution of the *cosmic–ray induced particle background* is negligible compared to the XRB in the energy range $\mathrm{E} \leq 5\,\mathrm{keV}$ and a further treatment of the data in this sense is not required for our study of the low and medium energy background in bands from B1 to B4. Concretely, in Figs. 7 and 8 from Read & Ponman (2003) we can see that the contribution of the XRB is over one order of magnitude above that of the cosmic–ray induced background in this energy regime.

In the case of *fluorescent lines* in the energy regime from B1 to B4, like the Al–K line at $\mathrm{E} \simeq 1.5\,\mathrm{keV}$ (Lumb et al., 2002), we must consider that the contribution of narrow lines vanishes when we focus on the study of broad energy bands. Consequently, we exclude a treatment of this effect in our data reduction process.

On the contrary, the contribution of the XRB is maximized for $\mathrm{E} \leq 5.0\,\mathrm{keV}$ and, in principle, it cannot be neglected in our study. In order to avoid a specific analysis of the XRB for each observation, which would dramatically increase the computation

time for an automatic procedure applied to a large database like in this thesis, we have chosen our sample to include a very broad range in Galactic coordinates (columns 2 and 3 in Tabs. 7 to 9). We also have a broad range in the column density of the photoelectric absorbing material ($0.6 \cdot 10^{20}\,\mathrm{cm}^{-2} < N_{\mathrm{H\,I}} < 909.1 \cdot 10^{20}\,\mathrm{cm}^{-2}$). These selections ensure a broad range in the XRB intensities of our sample, as already confirmed by the RASS. Additionally, the large number of selected observations yields a rich variety in structures of absorber column density present in the individual fields. Then, by averaging all fields of the sample, the differences in the structure of the XRB for each field are compensated. Consequently, a specific study of the XRB in each field can be neglected in our investigation of the vignetting in XMM–Newton.

7.2.4 Source Detection

The analysis of the diffuse XRB also requires the rejection of the contribution of point sources to the data. Here, we invoked the SAS tasks *eboxdetect* (boxsize=5, likemin=10, nrun=4) and *emldetect* (mlmin=10, scut=0.9, ecut=0.68) for all observations in Tab. 7 and for the energy band C1. This was performed in the *double run* mode proposed in the *ABC Guide to XMM–Newton Data Analysis* in which *eboxdetect* is run twice to obtain an appropriate background map which is then used as input for *emldetect*.

After completing the source detection, we make use of a self–developed tool to automatically eliminate the contribution of all point sources. This was done by the creation of so–called *cheese images* and posterior refilling of the gaps with the background level of a nearby *source–free* region. The refilling is necessary in order to avoid an artificial decrease in the intensity of our accumulated database towards the center of the detectors due to the higher source detection rate in the central area of the cameras. We explain this in some more detail in the following.

In Sect. 7.3 we will average the background maps obtained here and, for this aim, maps with a high number of sources close to the center of the field are unacceptable since they yield in a significant loss of XRB intensity in the inner 5 arcmin. A *refilling* step for every field is necessary. In this step, we fill each *hole* in the cheese images with an approximate background intensity value according to a source free region in its vicinity. For this purpose, we implemented an iterative procedure based on a Gaussian smoothing task (*asmooth* of SAS with smoothtype='simple') with $\sigma = 1.5\,\mathrm{arcmin}$. In each iteration, background areas (without sources) are kept constant. Then, the value obtained by the Gaussian filter for the areas with sources is used as input for the same areas in the next iteration step. In general at most five iteration steps are necessary until the difference between the areas with sources of two successive steps stays below the accuracy level of the data (see also Sect. 7.2.2).

Our choice of a smoothing size of $\sigma = 1.5\,\mathrm{arcmin}$ is justified with similar arguments

as for the exposure times in Sect. 7.1. At least one X–ray photon is expected in each point of the new resolution grid with 1.5 arcmin angular spacing.

7.3 Exposure Maps

The final step in the data reduction process for diffuse emission involves the correction due to the *vignetting* of the XMM–Newton mirrors. As we already mentioned in Sect. 3.3.3, vignetting is an effect that depends on photon energy and causes a gradual decrease of sensitivity towards the rim of the FOV. This dependency stems from the reduction of effective area of the detectors with off–axis angle and photon energy. The standard method to correct for vignetting consists in dividing the observed maps through the so–called *exposure maps*.

We tested the SAS 5.3.3 tool *eexpmap* for the calculation of the exposure maps. We detected an overestimation of the correction towards the rims of the FOV (see Fig. 43), which yields final intensity maps with very bright rims (*inverted tunnel effect*). Read & Ponman (2003) faced this problem and proposed a different method to correct for vignetting based on the *in–flight* performance of XMM–Newton. We extended their investigation to a longer accumulated exposure time (from $\simeq 0.7$ Ms to $\simeq 1.4$ Ms) and take advantage of the improved data reduction tools presented in the preceeding sections.

We use the background maps explained in Sect. 7.2.4 as a weighted sample to calculate the mean background intensity distribution affected by vignetting as observed by XMM–Newton *in–flight*. The weighting used for observations in the sample is proportional to the effective observation time (after solar proton filtering) as shown in columns 6 and 8 in Tabs. 7, 8 and 9. In all cases, the background maps are converted to *detector coordinates* (*XMM–Newton Users‘ Handbook*). Thus and since the observations are summed up always in the same orientation (see Sect. 7.4), we can study not only the radial distribution of the mean exposure maps, which is valid only if there is radial symmetry in the vignetting, but the complete 2–D distribution.

In Fig. 44, we present our results for the medium and low energy regimes (B1 to B4, $1\,\mathrm{keV} < E < 5\mathrm{keV}$). We focus on these regimes because:

- B1 and B2 are of most importance for the investigation of the diffuse X–ray plasma like, e.g., galactic X–ray Halos or the warm/hot intergalactic medium. This is because the bulk of the X–ray emission of such plasmas, with temperatures in the million K regime, is done in the keV regime covered by bands B1 and B2.
- B3 and B4 are dominated by the extragalactic X–ray background and, since this emission is well–known and very homogeneous, these two bands are a good

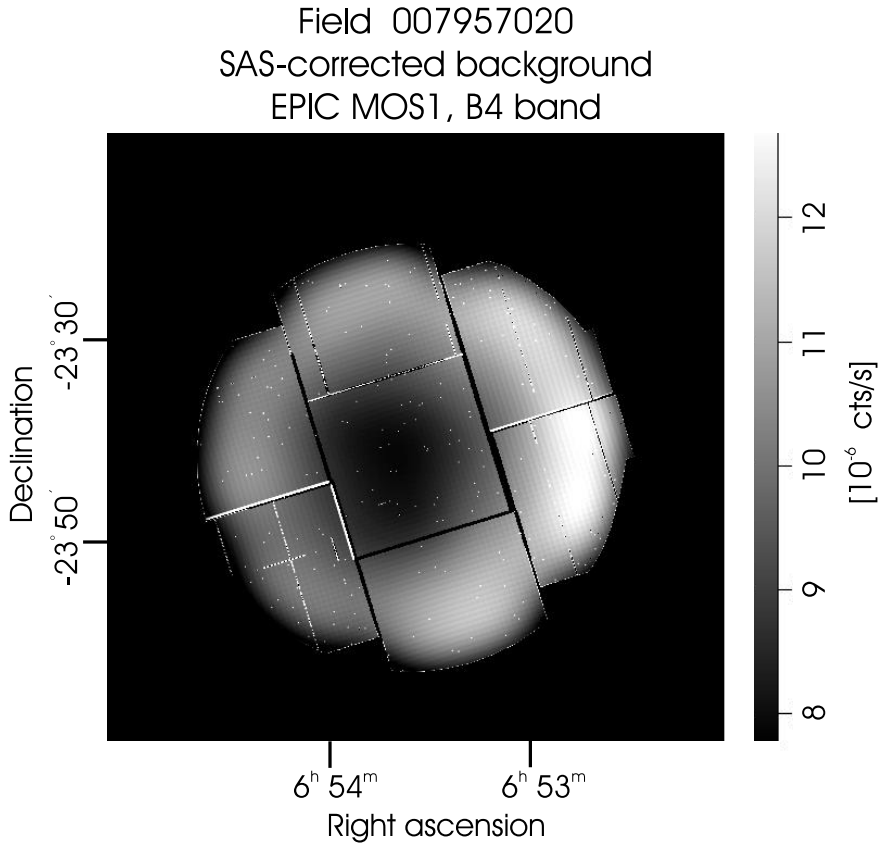

Fig. 43: *X–ray background map towards the field indicated in the upper part of the panel, as obtained by the standard SAS data reduction tasks: The SAS–calibrated photon image is "source filtered" (see Sect. 7.2.4), smoothed and finally corrected by the exposure map calculated by the corresponding SAS task (eexpmap). The increase in intensity towards the rims of the detector (see* inverted tunnel effect *in Sect. 7.3) is created by the use of the task eexpmap. This resulting background map is unacceptable since, at the B4 band, the X–ray background is dominated by the extragalactic background (Read & Ponman, 2003) which must yield in very homogeneous intensity distributions.*

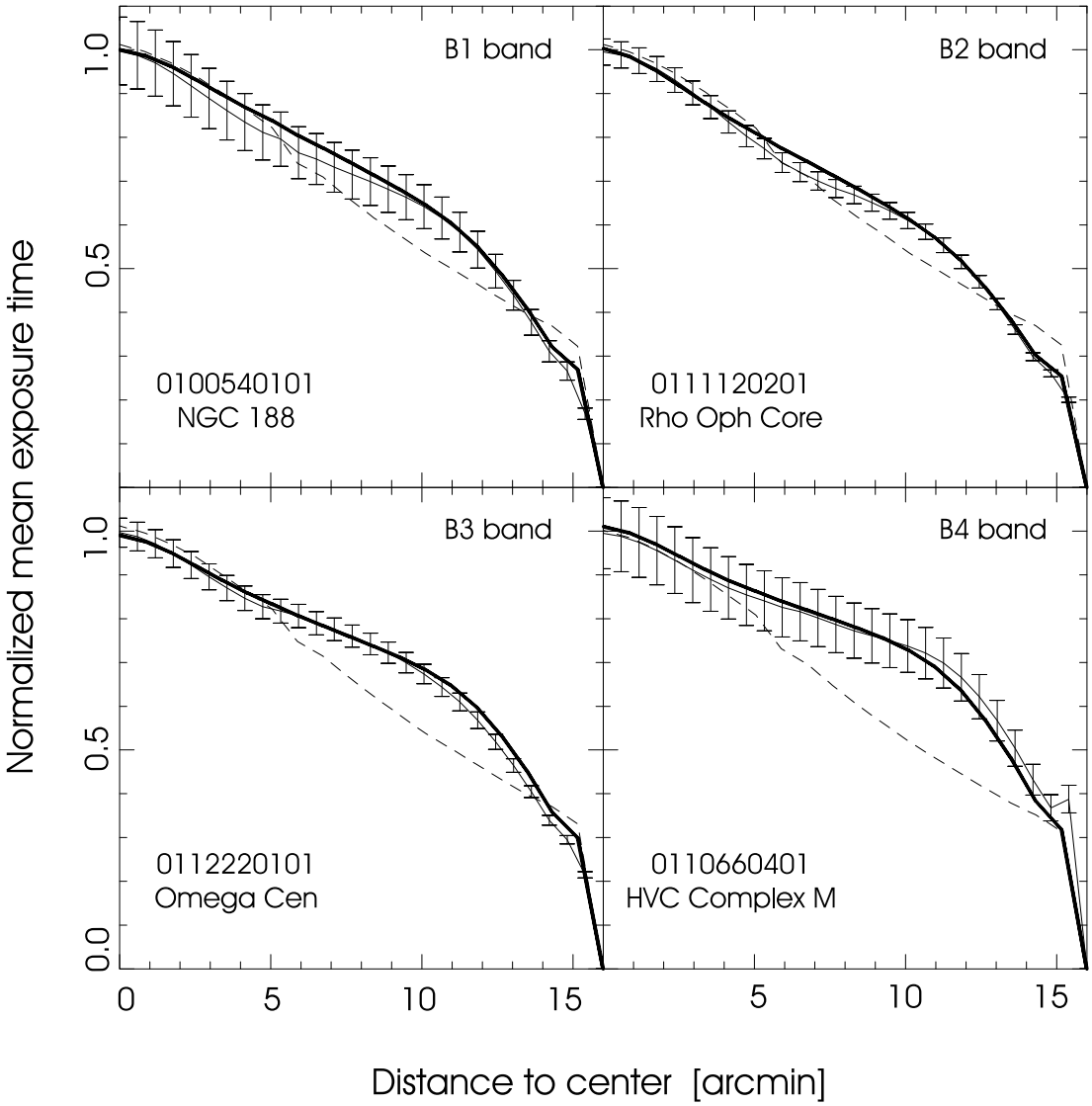

Fig. 44: *Normalized mean exposure time vs. radial distance to the optical center of the EPIC MOS2 camera for the four energy bands shown at the upper right part of each diagram. The thick solid line shows our new developed exposure maps. To illustrate the quality of these exposure maps, we also show the background intensity distribution, without correction for vignetting, of four different observations (thin solid lines). The error bars are calculated based on the photon statistics of the inner 5 arcmin of the observations. The solid lines can be compared to the SAS calculated exposure maps (dashed lines) for the corresponding observations and bands.*

choice to perform the normalization of the intensity distribution across the fields of interest.

The presented method leads to a better agreement between the observations and our results than between observations and the respective exposure maps as calculated by *eexpmap*. Some examples, included in our database, are shown in Fig. 44. This agreement is extended to the remaining observations in the database. The data reduction method results in the elimination of the *inverted tunnel effect* in the background intensity obtained by the use of the standard data reduction tools. Early versions of these maps, with slight differences in the source detection and smoothing parameters in comparison to our method as well as a shorter accumulated exposure time, have been already successfully used for the detection of very faint extended X–ray emission in nearby dwarf galaxies by Kappes et al., (in prep.). However, it is important to note that this success is reduced to the inner region of the detector ($\sim$ CCD1), while we are interested in extending this analysis to the entire FOV.

Concerning the use of our exposure maps for specific XMM–Newton pointings, the maps must be rescaled to the *effective* exposure time of the observation. In some cases, an additional rescaling is necessary to adjust the overall shape of the exposure maps and the observed X–ray distribution before performing the correction for vignetting. This is because individual observations of the background – mainly in the low energy regime B1 and B2 – show real structure partly due to variations in the absorbing column density in the FOV (see Sect. 5) and partly to the limitations in the source detection procedures which may fail to detect point sources with very faint emission. These effects occasionally result in an enhancement or in a decrease of the background intensity in the center region of the detector for the individual observations. Since this inner region ($r \leq 2$ arcmin) is used as default reference to normalize the rescaling of the exposure maps, a new scaling (based in another detector region and generally within 10% of the default solution) might be needed in some cases to avoid an over- or underestimation of the total background count rate. At this point, the exposure maps are ready to be used.

7.4 Radial Asymmetry of the XMM–Newton MOS1 Vignetting in the Soft Energy Regime

Until this point, we have supposed that the exposure maps of the EPIC MOS detectors are radially symmetric. Excluding the gaps of the so–called detector mask and the asymmetry at the rims of the FOV, the radial symmetry assumption is acceptable because vignetting depends only on properties of the mirrors. This argumentation is supported by our results for all bands in the MOS2 camera and for bands B2 to B4 of MOS1. All these exposure maps show their intensity maximum at the center of the FOV and the decrease with increasing radius is constant for all azimuth angles, like

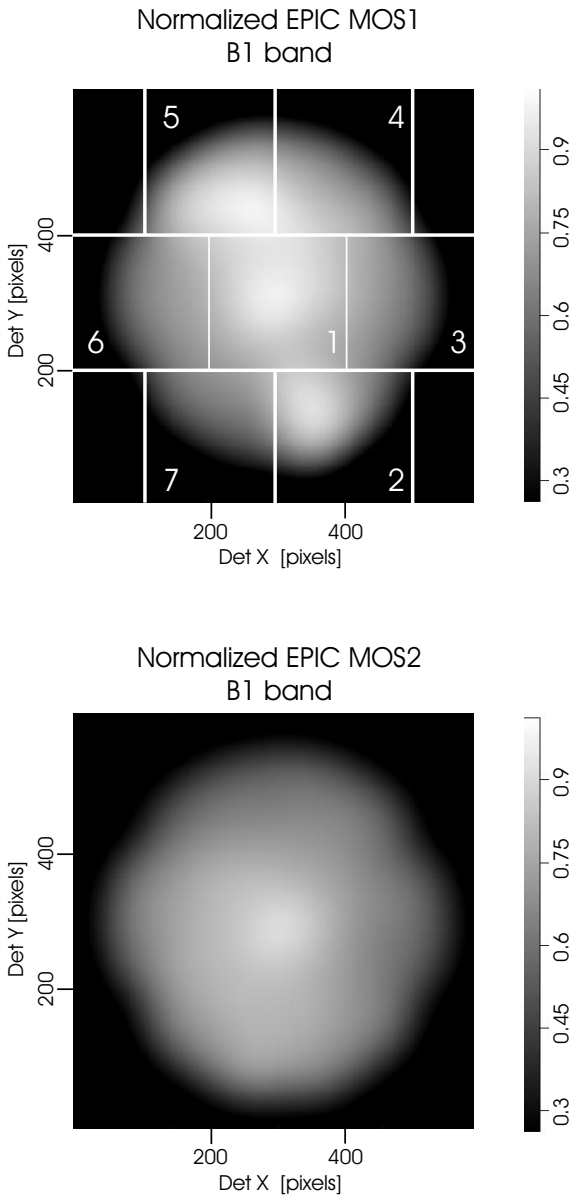

Fig. 45: **Upper panel:** *Normalized exposure maps for the EPIC MOS1 detector in the B1 energy band as obtained with the method presented in Section 7.3. Detector coordinates are used. The bright regions towards the bottom–right and top–left of the map are due to the inclusion of* bright CCD contaminated *(see Sect. 7.4) observations in the calculation of this map. More details for this camera and band are shown in Fig. 46. The gaps and numbers indicate the positions of the seven CCDs of the MOS1 camera.* **Lower panel:** *Normalized exposure map, EPIC MOS2, band B1. The radial symmetry of this map is representative of all other bands and MOS instruments. In order to eliminate the gaps of detector mask and the asymmetries towards the border of the FOV, we use the same procedure that we use for the refilling of the cheese images (see Sect. 7.2.4).*

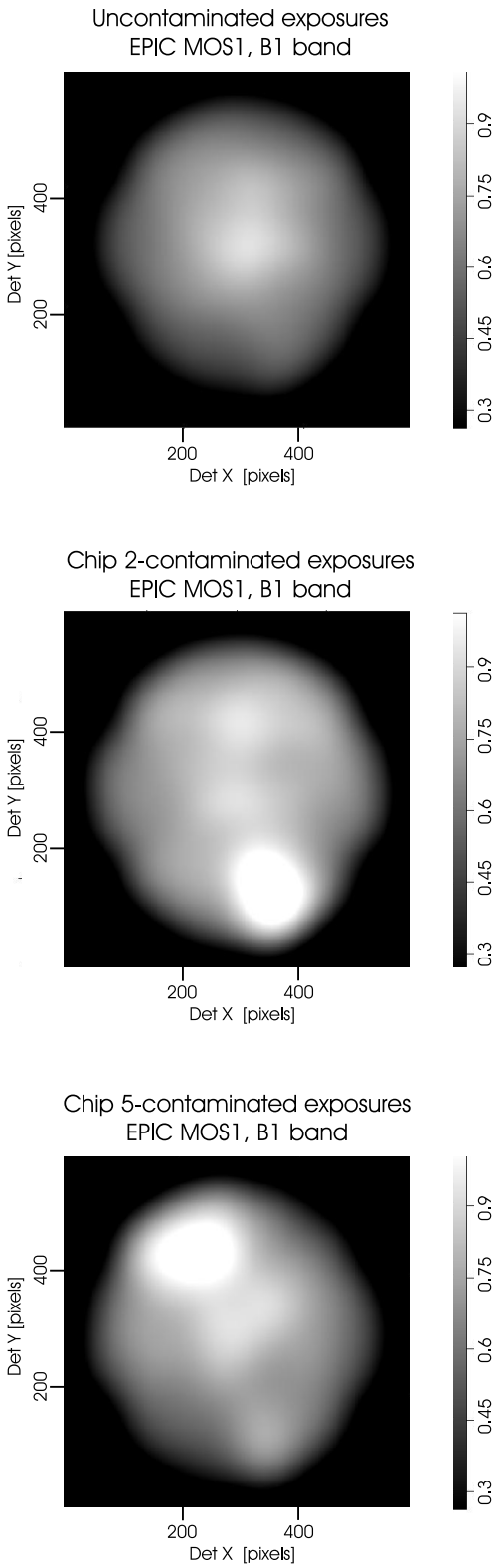

Fig. 46: *Exposure maps calculated for the three individual data sets indicated in the top of each figure. The maps are normalized to a value of 1 in the center of the map (like in the lower panel of Fig. 45). The artificial enhancement in the normalized count rate of the contaminated observations amounts up to a value of 1.5 in the affected regions of CCDs 2 and 5. This corresponds up to a factor of 2 above the uncontaminated case shown in the upper panel.*

in the lower panel of Fig. 45. But this structure is not present in the exposure maps obtained for MOS1 in the B1 band. The upper panel of Fig. 45 shows the result for this band. Significant enhancements of the exposure map in two regions associated to CCDs 2 and 5 (numeration is adopted from the *XMM–Newton Users' Handbook*) are detected at a first visual inspection of the data. The size of the database that we have used – over 1.4 Ms observation time – and the number of contaminated observations, indicates a high statistical significance to the reality of these enhancements. In the following, we will focus on the investigation of these *bright CCDs*.

We performed an individual study of the observations in our database and detected a number of observations which showed a clear enhancement, up to a factor of two, in the observed count rate (B1 band) in certain regions of the MOS1 detector. The count rate increase is confined to CCD2 in most cases. However, among these affected observations, some present an additional contamination of CCD5. In Tabs. 7, 8 and 9, the superscripts ^{2} and ^{5} in the first column mark observations which present contamination, in CCD2 and 5 respectively. We selected as contaminated the observations with mean background intensities in CCD2 or CCD5 exceeding those of the uncontaminated CCDs by more than the level of accuracy of the data ($1-\sigma$). More formally:

$$\begin{aligned} I_2 - \sigma_2 &\geq I_{345} \\ I_5 - \sigma_5 &\geq I_{345} \end{aligned} \tag{18}$$

Here I represents the mean background intensity, σ the error in its determination and the sub–indexes represent the CCDs used to calculate the respectives I and σ (see also Fig. 47 and Eq. 19).

It is important to note, that we also made use of more actual versions of the data analysis software (SAS 5.4.1) and calibration database (synchronization of March, 2004) to reanalyze the contaminated fields. The results obtained with the newest tools are only marginally different from those obtained with the older, and the bright CCD contamination appears in the same manner in both cases. Furthermore, the use of the SAS task *eexpmap* to calculate the exposure maps in the contaminated observations yields results that do not reflect the intensity enhancement registered during the observations. To summarize, the standard tools do not perform any correction for the contamination reported here.

We also compared our set of affected observations with those analyzed by Read & Ponman (2003) to compute their EPIC background maps for the *medium* filter. From a total of 21 pointings in their sample, at least 3 contain CCD5 contamination (observation IDs 0021740101, 0022740301 and 008564021) and several more shown up with CCD2 contamination. The use of this contaminated observations generates an up to

now undetected asymmetry in their MOS1 *event files*[12] and exposure maps for the soft energy regime (B1) equivalent to the one presented in Fig. 45.

Finally, we also rule out an origin for the contamination in the inhomogeneities of the quantum efficiency for the MOS 1 detector presented in Fig. 23 (Sect. 3.3.3). This is because a lower quantum efficiency for CCDs 2 and 5, as shown in Fig. 23, would imply a lower background rate in both CCDs and not an increase in the count rate as presented here (Fig 45).

After separating the observations in three sets, we repeated the calculation of the exposure maps for the cases: without bright CCDs, with bright CCD2 and with bright CCD5. The results are shown in Fig. 46. With this first rough classification of the observations, the map obtained for the cases without bright CCDs (conditions given by Eq. 18) is not completely satisfactory because the effect of CCD2 contamination is still present in the resulting exposure map (upper panel in Fig. 46). Furthermore, CCD2 contamination is also clearly present in the map calculated with the CCD5 contaminated observations (lower panel in Fig. 46). All this indicates that probably all observations are affected by the CCD2 contamination, as we might derive from the upper panels of Fig. 47. From those panels, we deduce that about 90% of the observations included in our sample show a higher background rate in CCD2 than in the remaining CCDs, although the excess is above the precision of the data only in about 50% of the cases (Eq. 18). In contrast, CCD5 contamination is confined to only a reduced fraction of the observations (15–20%) and its effect does not appear when calculating exposure maps with the remaining observations in the database: CCD2 contaminated and uncontaminated pointings in the middle and upper panel of Fig. 46 respectively. Another difference between both contaminations is given by the shape of the contaminated region in each case (see different shape for the contaminated regions in the middle and lower panels of Fig. 46). All these considerations point to different origins for the contaminations of CCD2 and CCD5. In the following, we present our first results in constraining these different origins.

7.4.1 Quantification of the Contamination in MOS1 CCDs 2 and 5

In order to develop a reliable tool to correct for the intensity enhancement in CCDs 2 and 5, we searched for a quantification of this effect based on the measured difference between contaminated and uncontaminated observations. We define the *contamination rate* of CCD 2 C_2 as

$$C_2 = \frac{I_2}{I_{346}} \tag{19}$$

[12] *http://www.sr.bham.ac.uk/xmm3/*

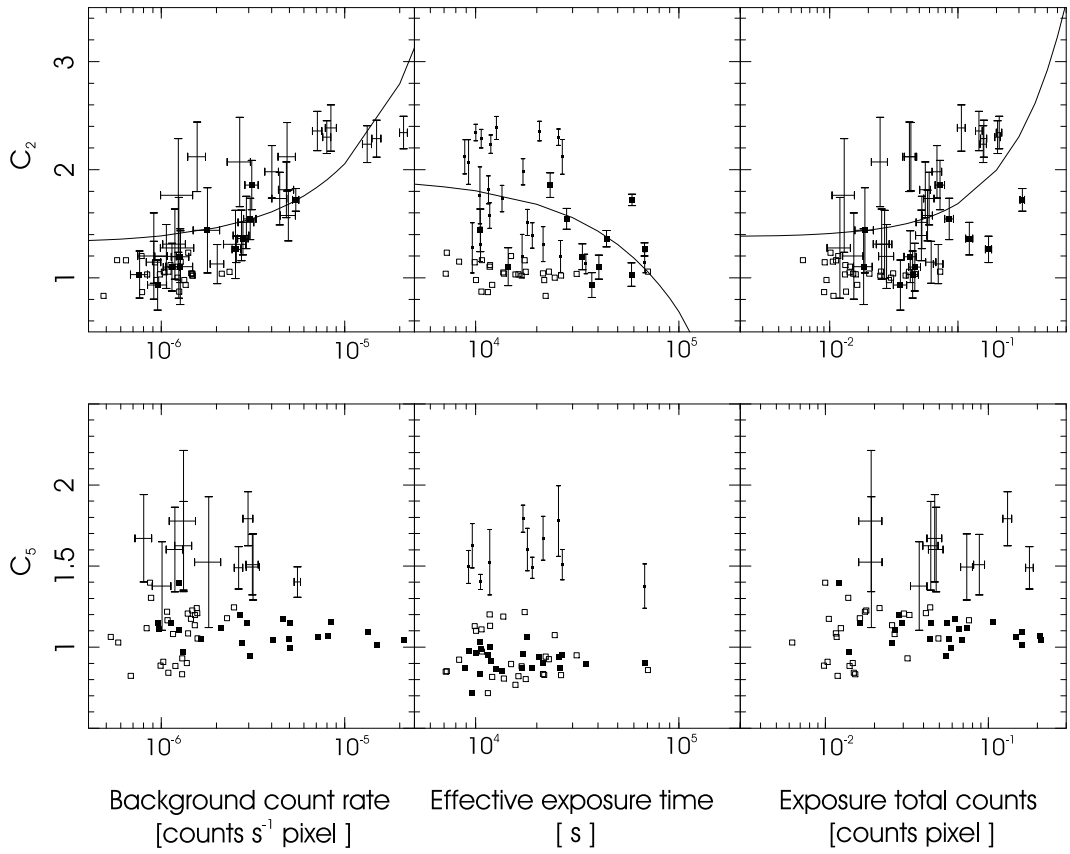

Fig. 47: **Upper panels:** *Scatter plot of the CCD2 contamination as defined in Eq. 19 vs. the quantities indicated in the horizontal axes in logarithmic scale. The points with error bars represent contaminated observations (Eq. 18), where solid squares correspond to observations which also present CCD5 contamination. Empty squares represent uncontaminated observations. The curves correspond to the regression lines of the data. The statistical significance of the regression lines is shown in Tab. 11. The mean background intensities of the left panel are calculated using the data gained with CCDs 3, 4, 5 and 7.* **Lower panels:** *Equivalent to the upper panels for the CCD5 contamination. Points with error bars are CCD5 contaminated, solid squares show CCD2 contaminated observations and empty squares represent uncontaminated observations. No regression lines are shown because the statistical tests do not reject the zero correlation hypothesis in any of the three cases shown here (see Tab. 11 and Sect. 7.4.1). Visually, the CCD5 contaminated set is well separated from the remaining observations which are located close to the* $C_5 = 1$ *line as expected for pointings free of contamination.*

Tab. 11: *Correlation coefficients of the CCD contamination rates as defined in Sect. 7.4 vs. the observation parameters listed in the left column of the table. The last row shows the critical value of a the statistical test for the significance of the correlation coefficient of the sample at a 95% confidence level adopted from Crow et al. (1960). We shown the 99% confidence level value in parenthesis. Note that the zero correlation is only rejected with the values of the CCD2 column.*

	C_2	C_5
Count rate	0.725	-0.366
Effective time	-0.405	-0.170
Total counts	0.473	-0.363
$\|r\|_{crit}$	0.339 (0.437)	0.602 (0.735)

We calculated the correlation coefficient of the contamination rate vs. different observation parameters like background count rate or effective exposure time. The upper panels of Figure 47 show a graphical comparison of the quantities and Tab. 11 the results of the correlation analysis. An equivalent contamination rate is defined for CCD 5 as is shown in the lower panels of Fig. 47.

CCD2 contaminated observations (points with error bars in the upper panels of Fig. 47) are concentrated towards the high background count rate part of the diagram. There is also a clear tendency to present higher contamination rates for higher count rates. This is confirmed by the statistical test for the significance of the correlation coefficient of the sample, which rejects the zero correlation hypothesis between contamination rate (Eq. 19) and the background count rates (see Tab. 11). With respect to the effective exposure time, after proton flare filtering, a negative correlation can be rejected at a 95% significance level but not at a 99% level. For this case, a larger sample of contaminated observations is necessary to derive definitive statistical conclusions. The correlation of CCD2 contamination rate with total counts is also accepted by the test, but the reliability of the correlation is significantly lower with respect to the case of the correlation with the background count rate. Furthermore, there are also uncontaminated observations in the high effective exposure time and high total counts parts of the diagrams (different to the count rate case). This indicates that probably the correlations found between the contamination rate and these two parameters are not real. As already mentioned, more data are necessary to derive definitive conclusions in this sense.

For the CCD5 contaminated data set, we detect a systematic overestimation in the CCD5 intensities of about a factor of two (points with error bars in the lower panels of Fig. 47). In contrast to the case of CCD2, there is no evidence for grouping of the contaminated observations towards any count rate, exposure time or total counts regime for CCD5 contamination. The correlation coefficients shown in the right column of

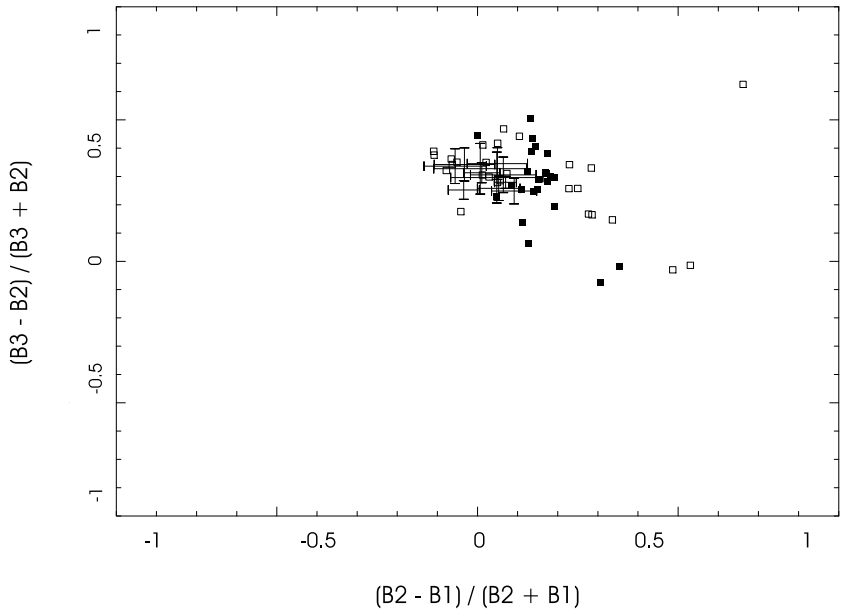

Fig. 48: *Hardness ratios of the X–ray backgrounds as detected with the EPIC MOS1 camera for the observations in Tab. 7. Empty squares correspond to observations free of CCD2 or CCD5 contamination, solid squares to CCD2 contaminated observations and the points with the error bars to CCD5 contaminations. However, in order to avoid the influence of this contamination in the hardness ratios presented here, we calculate the values based only on the data provided by uncontaminated CCDs. The results shown in this Figure rule out a correlation between the hardness ratio of the X–ray background towards the observed field and the presence of bright CCD contamination, either for the CCD5 or for the CCD2 case. This can be deduced from the fact that the contaminated observations are spread in the panel with a similar distribution to that of the uncontaminated observations.*

Tab. 11 do not reject the zero correlation in any of the three cases with contamination rate.

We also tested whether the bright CCD contamination is triggered by extreme values in the X–ray background hardness ratios of the observations or is correlated with the exposure date (see Fig. 48 and Tab. 7) and no correlation could be found.

From our analysis of the bright CCD contaminations, we conclude that they probably have their origin in *software* problems. The contamination is always present and grows with mean background count rate in the case of CCD2. Therefore, the use of diffuse X–ray data from this CCD2 should be avoided until a consistent method to mitigate the effect of the contamination is developed. For CCD5 case, since the frequency in the presence of this contamination is below 20% and the contamination rate is always high ($C_5 > 1.5$ using an equivalent definition to that of Eq. 19), we recommend to check whether the intensity increment is visible in the raw data before performing further analysis of the diffuse X–ray data gained with this CCD.

7.5 Conclusions for the XMM–Newton Data Reduction

Our study of the in–flight performance of XMM–Newton has produced new results concerning the treatment of *solar proton flares* and *vignetting*. These results imply the necessity of the inclusion of the soft energy bands in the search for solar proton flares, different to the conclusions of previous works (Lumb et al., 2002; Marty et al., 2003; Read & Ponman, 2003). For this data reduction step, we developed an iterative automatic procedure that can be "pipelined" to the XMM–Newton raw data.

Since the standard tools for the vignetting correction in the XMM–Newton EPIC detectors are not sufficient to allow a sensitive analysis of faint signals in the soft energy regime ($E \leq 2.0\,\mathrm{keV}$), as we can see in Fig. 43, we have developed a new task to calculate the *real* exposure map of XMM–Newton. It is based on the in–flight performance of the observatory and uses longest accumulated exposure time today. The process to calculate exposure maps can be repeated automatically for user defined energy bands and observations. An extension to alternative modes and filters (others than *FullFrame* and *Medium* presented here) can be performed by exploiting the XMM–Newton Science Archive.

We detect an artificial increase in the measured count rates (softest energy, $0.2\,\mathrm{keV} \leq E \leq 0.5\,\mathrm{keV}$) in the EPIC MOS1 CCDs 2 and 5. This contamination appears to be present in practically all observations and it seems to be associated to high background rates in the case of CCD2. The set of affected observations accumulated for CCD5 contamination until today is not sufficient to draw definitive conclusion on the origin of the contamination. The count rate in the affected CCDs is increased up to a factor of two. Such a significant difference must be taken into account when investigating

diffuse emission or the hardness ratios of faint sources detected by one of these two CCDs.

To summarize, the actual status of the data reduction for XMM–Newton still presents fundamental problems which prevent a reliable study of faint soft X–ray sources (e.g., *Bright CCD* contamination). These difficulties have to be further investigated and solved before being able of using the full capabilities of the satellite. Interesting topics that could be in principle investigated with XMM–Newton, like for example:

- emissivity distribution of faint X–ray halos of external galaxies,
- the X–ray emission of the WHIM,
- the degree of clumping of the ISM in its X–ray emitting and absorbing phases.

can be only investigated at present, if the X–ray emission is concentrated in the inner part of the FOV ($r < 5$ arcmin), where the uncertainties in the data reduction are reduced. This excludes the study of the three topics mentioned above which involve, in general, structures covering significantly larger angular scales.

8 Summary and Outlook

In this thesis, I made use of the latest release of the ROSAT all-sky survey (Snowden et al., 1997) and of the first stray–radiation corrected all–sky HI survey, the Leiden/Dwingeloo/Argentinian Institute of Radioastronomy/University of Bonn survey (Hartmann & Burton, 1997; Arnal et al., 2000, Kalberla et al., submitted), to derive a self–consistent model for the soft X–ray background (Chap. 5). Our effort has been focused on determining the number of independent Galactic X–ray plasmas contributing to this diffuse X–ray emission, as well as their respective temperatures and intensity distributions.

With a careful investigation of the radiative transfer for the soft X–rays through the ISM (Sect. 5.2), we have demonstrated that a single isothermal X–ray Halo is sufficient to explain the Galactic Halo contribution to the soft X–ray background, in contrast to a multi–component scenario (Kuntz & Snowden, 2000). We derive this conclusion based on the construction of a model for the X–ray emission that fits the ROSAT observations in *all* ROSAT energy bands *simultaneously* (Sect. 5.2.2) and for the entire high Galactic latitude sky (Figs. 35 and 36), extending previous works for the northern hemisphere (see, e.g. Pietz, 1997). Additionally, a gradient with Galactic coordinates in the temperature of the X–ray Halo (see, e.g. Almy et al., 2000) is ruled out for the high Galactic latitude sky within the accuracy of the ROSAT data. For the low latitude sky, a temperature gradient cannot be refuted or verified with the method presented here. This is because, in this region,the ISM is opaque to the soft X–rays, preventing a systematic analysis of the distant components of the SXRB in the lower energy regimes. Thus, more sensitivity and spectral resolution for data of higher energy regimes, which can cross the ISM even in the Galactic Plane region, are required to solve this question, making of XMM–Newton the ideal instrument for this purpose.

For the temperature of the Galactic X–ray Halo, we have obtained a best–fit value of $T_{\rm HALO} = 10^{6.15}$ K. The obtained temperature for the foreground component (LHB) is $T_{\rm LHB} = 10^{5.9}$ K. Concerning the intensity distribution of both components, the X–ray Halo is well described by the predictions given by the *Galactic Dark Matter Halo model* by Kalberla (2003) (Fig. 33), while the accuracy of the ROSAT data does not allow to determine exactly the shape of the LHB (Sect. 5.5.1).

We have also demonstrated that the distribution of the neutral phases of the ISM (CNM and WNM, Sect. 4.1) is sufficient to explain the intensity attenuation of the SXRB due to photoelectric absorption on all–sky scale. The contribution of the WIM can be neglected except for some special directions where the ratio of neutral to ionized

matter is minimized. Towards these regions, only the Lockman Window (Sect. 6.2) has a sufficient angular extension to be clearly detected in the all–sky maps (Fig. 35). For this case, we have to note that the Lockman Window region is a very extreme case where about 40% of the matter in the ISM is ionized (Kappes et al., 2003) in comparison to typical ratios from 10% to 15%.

In Chap. 6, we have taken advantage of the goodness of the fits obtained for the SXRB to search for faint unreported signals in the RASS. Concretely, with a reliable foreground and background subtraction from the ROSAT observations it is possible to constrain the distances to the HVC complexes. We conclude in Sect. 6.1 that the complexes A, C and M are located *outside* the Galactic X–ray Halo. This is based on the absence of an intensity attenuation in the SXRB that can be related to the mentioned HVC complexes (no corresponding X–ray shadows). Our results for the distances, together with the complementary constraints found in the literature (Woerden et al., 1999) and the reports on excess emission in some regions of the HVC complexes (see Kerp et al. (1999) and Fig. 38), are in agreement with an scenario in which the HVCs are falling into the Milky Way and are heated by shocks when they enter the Galactic Halo.

Another important result presented in Chap. 6 is the detection of an additional diffuse X–ray source whose position and temperature is in agreement with the predictions of Kravtsov et al. (2002) for the emission of the warm/hot intergalactic medium in the local Universe. Concretely, we obtain a result for the temperature of this region of $T \simeq 10^{6.3}$K, included in the $10^{6.3} - 10^{6.5}$K range proposed by Kravtsov et al. (2002). Unfortunately, the intensity of the detected emission is barely above the accuracy of the ROSAT data, corresponding to a 1.3σ detection in the R2 band. Further observations of the region of interest are necessary to improve the statistical significance to our detection. If the existence of the X–ray emission is confirmed by future observations, this would become the first direct unambiguous detection of the local warm/hot intergalactic medium in emission, complementing the actual detections performed with absorption line studies (see, e.g. Fang et al., 2002; Nicastro et al., 2002; Richter et al., 2004). However, our investigation demonstrates that a "perfect" background subtraction, here background denotes the contributions of the extragalactic X–ray background, Galactic X–ray Halo and LHB, is sufficient and necessary to detect such faint X–ray sources as the WHIM, even at the level of accuracy of the ROSAT data (about 10% in the RC band).

Following this argumentation, we will push forward in the future the search for additional diffuse X–ray sources in the RASS. In this line of investigation, an iterative procedure which uses the knowledge acquired on the additional sources in the RASS to improve the quality of the models for the SXRB, will increase the sensitivity of our methods for the detection of even fainter additional sources. Thus, it may be also possible to extend the area of interest to, for example, regions closer to the Galactic Plane than possible today (with the limit of $|b| > 25°$). The region $20° > |b| > 25°$ is of spe-

cial interest. There we can study the disk–halo interface (see, e.g. McClure-Griffiths et al., 2002).

Finally, we have presented in Chap. 7 our actual results in the development of a reliable data reduction method for the study of faint diffuse emission with XMM–Newton. We have seen, that despite the unmatched sensitivity of XMM–Newton in comparison to prior X–ray satellites, diffuse soft X–ray background studies are not possible with this observatory in the present, because of several technical problems. Although the difficulties with *solar proton flare* filtering (Sect. 7.2.2) or the calculation of *exposure maps* (Sect. 7.3) might already be surpassed, –permitting investigations that only involve the central part of the XMM–Newton detectors–, further work to overcome, for example, *bright CCD contamination* (Sect. 7.4) or the homogeneity of the detector quantum efficiency (Sect. 3.3.3) is needed to allow the use of the full field–of–view of XMM–Newton to investigate soft diffuse X–ray emission.

References

Almy, R. C., McCammon, D., Digel, S. W., Bronfman, L., & May, J. 2000, ApJ, 545, 290

Arnal, E. M., Bajaja, E., Larrarte, J. J., Morras, R., & Pöppel, W. G. L. 2000, A&AS, 142, 35

Ballet, J. 1999, A&AS, 135, 371

Barber, C. R., Roberts, T. P., & Warwick, R. S. 1996, MNRAS, 282, 157

Biermann, P., Kronberg, P. P., & Madore, B. F. 1982, ApJ, 256, L37

Bloemen, J. B. G. M. 1987, ApJ, 322, 694

Blumenthal, G. R. & Tucker, W. H. 1974, in ASSL Vol. 43: X-ray Astronomy, 99–+

Bondi, H. 1952, MNRAS, 112, 195

Bondi, H. & Hoyle, F. 1944, MNRAS, 104, 273

Bowyer, C. S., Field, G. B., & Mack, J. E. 1968, Nature, 217, 32

Bunner, A. N., Coleman, P. L., Kraushaar, W. L., & McCammon, D. 1971, ApJ, 167, L3+

Burrows, D. N. & Mendenhall, J. A. 1991, Nature, 351, 629

Charles, P. A. & Seward, F. D. 1995, Exploring the X-ray universe (Cambridge, New York: Cambridge University Press, |c1995, ISBN 0521261821)

Chu, Y. & Mac Low, M. 1990, ApJ, 365, 510

Crow, E., Davis, F., & Maxfield, M. 1960, Statistics Manual (Dover Publications; New York)

Dahlem, M. & Stuhrmann, N. 1998, A&A, 332, 449

Danly, L., Albert, C. E., & Kuntz, K. D. 1993, ApJ, 416, L29+

Dekel, A. & Ostriker, J. P. 1999, Formation of structure in the universe (Cambridge University Press)

Dickey, J. M. & Lockman, F. J. 1990, ARA&A, 28, 215

Efremov, I. N. 1989, Moscow Izdatel Nauka

Ehle, M., Pietsch, W., Beck, R., & Klein, U. 1998, A&A, 329, 39

Elwert, G. 1956, Zeitschrift fur Astrophysics, 41, 67

Fabbiano, G. 1989, ARA&A, 27, 87

Fabbiano, G. & Trinchieri, G. 1984, ApJ, 286, 491

Fabian, A. C. 1999, Proceedings of the National Academy of Science, 96, 4749

Fabian, A. C. & Barcons, X. 1992, ARA&A, 30, 429

Fabian, A. C., Schwarz, J., & Forman, W. 1980, MNRAS, 192, 135

Fang, T., Marshall, H. L., Lee, J. C., Davis, D. S., & Canizares, C. R. 2002, ApJ, 572, L127

Ferrando, P., Abbey, A. F., Altieri, B., et al. 2003, in X-Ray and Gamma-Ray Telescopes and Instruments for Astronomy. Edited by Joachim E. Truemper, Harvey D. Tananbaum. Proceedings of the SPIE, Volume 4851, pp. 232-242 (2003)., 232–242

Field, G. B., Goldsmith, D. W., & Habing, H. J. 1969, BAAS, 1, 240

Fink, H. H. & Trümper, J. 1982, Landolt–Börnstein (Springer–Verlag)

Forman, W., Jones, C., & Tucker, W. 1985, ApJ, 293, 102

Forman, W., Schwarz, J., Jones, C., Liller, W., & Fabian, A. C. 1979, ApJ, 234, L27

Freyberg, M. J. 1994, Ph.D. Thesis

Friedman, H., Lichtman, S. W., & Byram, E. T. 1951, Physical Review, 83, 1025

Giacconi, R., Gursky, H., Paolini, F., & Rossi, B. 1962, Physical Reviews Letters, 9, 439

Goldin, L. L. & Novikova, G. 1988, Introduccion a la Fisica cuantica (Mir)

Gondoin, P., Aschenbach, B., Erd, C., et al. 2000, in Proc. SPIE Vol. 4140, p. 1-12, X-Ray and Gamma-Ray Instrumentation for Astronomy XI, Kathryn A. Flanagan; Oswald H. Siegmund; Eds., 1–12

Gondoin, P., Aschenbach, B. R., Beijersbergen, M. W., et al. 1998a, in Proc. SPIE Vol. 3444, p. 278-289, X-Ray Optics, Instruments, and Missions, Richard B. Hoover; Arthur B. Walker; Eds., 278–289

Gondoin, P., Aschenbach, B. R., Beijersbergen, M. W., et al. 1998b, in Proc. SPIE Vol. 3444, p. 290-301, X-Ray Optics, Instruments, and Missions, Richard B. Hoover; Arthur B. Walker; Eds., 290–301

Gondoin, P., Aschenbach, B. R., Brauninger, H., et al. 1996, in Proc. SPIE Vol. 2808, p. 390-401, EUV, X-Ray, and Gamma-Ray Instrumentation for Astronomy VII, Oswald H. Siegmund; Mark A. Gummin; Eds., 390–401

Gorenstein, P. 1974, in ASSL Vol. 43: X-ray Astronomy, 299–+

Gursky, H., Kellogg, E., Murray, S., et al. 1971, ApJ, 167, L81+

Haffner, L. M., Reynolds, R. J., Tufte, S. L., et al. 2003, ApJS, 149, 405

Hartmann, D. & Burton, W. 1997, Atlas of Galactic Neutral Hydrogen (Cambridge University Press)

Hartmann, D., Kalberla, P. M. W., Burton, W. B., & Mebold, U. 1996, A&AS, 119, 115

Hartmann, D., Magnani, L., & Thaddeus, P. 1998, ApJ, 492, 205

Hasinger, G., Altieri, B., Arnaud, M., et al. 2001, A&A, 365, L45

Herbstmeier, U., Mebold, U., Snowden, S. L., et al. 1995, A&A, 298, 606

Jansen, F., Lumb, D., Altieri, B., et al. 2001, A&A, 365, L1

Kahabka, P. & van den Heuvel, E. P. J. 1997, ARA&A, 35, 69

Kalberla, P. M. W. 2003, ApJ, 588, 805

Kalberla, P. M. W. & Kerp, J. 1998, A&A, 339, 745

Kalberla, P. M. W., Mebold, U., & Velden, L. 1980, A&AS, 39, 337

Kappes, M., Kerp, J., & Richter, P. 2003, A&A, 405, 607

Katayama, H., Takahashi, I., Ikebe, Y., Matsushita, K., & Freyberg, M. J. 2004, A&A, 414, 767

Kato, T. 1976, ApJS, 30, 397

Kerp, J. 1994, A&A, 289, 597

Kerp, J., Burton, W. B., Egger, R., et al. 1999, A&A, 342, 213

Kerp, J., Herbstmeier, U., & Mebold, U. 1993, A&A, 268, L21

Kerp, J., Mack, K.-H., Egger, R., et al. 1996, A&A, 312, 67

Kirsch, M. 2004, XMM–EPIC status of calibration and data analysis, Tech. Rep. XMM–SOC–CAL–TN–0018, European Space Agency

Kravtsov, A. V., Klypin, A., & Hoffman, Y. 2002, ApJ, 571, 563

Kriss, G. A., Canizares, C. R., McClintock, J. E., & Feigelson, E. D. 1980, ApJ, 235, L61

Kuntz, K. D. & Snowden, S. L. 2000, ApJ, 543, 195

Lallement, R., Welsh, B. Y., Vergely, J. L., Crifo, F., & Sfeir, D. 2003, A&A, 411, 447

Landini, M. & Monsignori Fossi, B. C. 1970, A&A, 6, 468

Lepp, S., McCray, R., Shull, J. M., Woods, D. T., & Kallman, T. 1985, ApJ, 288, 58

Liedahl, D. A., Osterheld, A. L., & Goldstein, W. H. 1995, ApJ, 438, L115

Lilienthal, D., Wennmacher, A., Herbstmeier, U., & Mebold, U. 1991, A&A, 250, 150

Lockman, F. J. 1984, ApJ, 283, 90

Lockman, F. J. 1999, Ap&SS, 267, 139

Lockman, F. J., Hobbs, L. M., & Shull, J. M. 1984, BAAS, 16, 981

Lockman, F. J., Jahoda, K., & McCammon, D. 1986, ApJ, 302, 432

Loewenstein, M., Mushotzky, R. F., Angelini, L., Arnaud, K. A., & Quataert, E. 2001, ApJ, 555, L21

Low, F. J., Young, E., Beintema, D. A., et al. 1984, ApJ, 278, L19

Lumb, D. H., Finoguenov, A., Saxton, R., et al. 2003, in X-Ray and Gamma-Ray Telescopes and Instruments for Astronomy. Edited by Joachim E. Truemper, Harvey D. Tananbaum. Proceedings of the SPIE, Volume 4851, pp. 255-263 (2003)., 255–263

Lumb, D. H., Gondoin, P., Turner, M. J., et al. 2000, in Proc. SPIE Vol. 4140, p. 22-31, X-Ray and Gamma-Ray Instrumentation for Astronomy XI, Kathryn A. Flanagan; Oswald H. Siegmund; Eds., 22–31

Lumb, D. H., Warwick, R. S., Page, M., & De Luca, A. 2002, A&A, 389, 93

Lyot, B. 1932, Zeitschrift fur Astrophysics, 5, 73

Marty, P. B., Kneib, J., Sadat, R., Ebeling, H., & Smail, I. 2003, in X-Ray and Gamma-Ray Telescopes and Instruments for Astronomy. Edited by Joachim E. Truemper, Harvey D. Tananbaum. Proceedings of the SPIE, Volume 4851, pp. 208-222 (2003)., 208–222

McCammon, D., Burrows, D. N., Sanders, W. T., & Kraushaar, W. L. 1983, ApJ, 269, 107

McCammon, D. & Sanders, W. T. 1990, ARA&A, 28, 657

McClure-Griffiths, N. M., Dickey, J. M., Gaensler, B. M., & Green, A. J. 2002, ApJ, 578, 176

McKee, C. F. & Ostriker, J. P. 1977, ApJ, 218, 148

Mebold, U. 1972, A&A, 19, 13

Mewe, R., Gronenschild, E. H. B. M., & van den Oord, G. H. J. 1985, A&AS, 62, 197

Morrison, R. & McCammon, D. 1983, ApJ, 270, 119

Nicastro, F., Zezas, A., Drake, J., et al. 2002, ApJ, 573, 157

Nousek, J. A., Fried, P. M., Sanders, W. T., & Kraushaar, W. L. 1982, ApJ, 258, 83

Paresce, F. 1984, AJ, 89, 1022

Penzias, A. A. & Wilson, R. W. 1965, ApJ, 142, 419

Pfeffermann, E. & Briel, U. G. 1986, in X-ray instrumentation in astronomy; Proceedings of the Meeting, Cannes, France, December 2-4, 1985 (A87-19722 07-35). Bellingham, WA, Society of Photo-Optical Instrumentation Engineers, 1986, p. 208-212., 208–212

Pietsch, W., Vogler, A., Klein, U., & Zinnecker, H. 2000, A&A, 360, 24

Pietz, J. 1997, PhD thesis, Universität Bonn

Pietz, J., Kerp, J., Kalberla, P. M. W., et al. 1998, A&A, 332, 55

Pigot, C., Belsole, E., Bennie, P. J., et al. 1999, in Proc. SPIE Vol. 3765, p. 251-264, EUV, X-Ray, and Gamma-Ray Instrumentation for Astronomy X, Oswald H. Siegmund; Kathryn A. Flanagan; Eds., 251–264

Plucinsky, P. P., Snowden, S. L., Briel, U. G., Hasinger, G., & Pfeffermann, E. 1993, ApJ, 418, 519

Pradas, J., Kerp, J., & Kalberla, P. M. W. 2003, Astronomische Nachrichten, 324, 150

Pringle, J. E. & Rees, M. J. 1972, A&A, 21, 1

Raymond, J. C. & Smith, B. W. 1977, ApJS, 35, 419

Read, A. M. & Ponman, T. J. 2003, A&A, 409, 395

Reynolds, R. J. 1990, in IAU Symp. 139: The Galactic and Extragalactic Background Radiation, 157–169

Richter, P., Savage, B. D., Tripp, T. M., & Sembach, K. R. 2004, ApJS, 153, 165

Sanders, W. T., Kraushaar, W. L., Nousek, J. A., & Fried, P. M. 1977, ApJ, 217, L87

Schulz, N. S. 1999, ApJ, 511, 304

Sfeir, D. M., Lallement, R., Crifo, F., & Welsh, B. Y. 1999, A&A, 346, 785

Snowden, S. L., Cox, D. P., McCammon, D., & Sanders, W. T. 1990, ApJ, 354, 211

Snowden, S. L., Egger, R., Finkbeiner, D. P., Freyberg, M. J., & Plucinsky, P. P. 1998, ApJ, 493, 715

Snowden, S. L., Egger, R., Freyberg, M. J., et al. 1997, ApJ, 485, 125

Snowden, S. L. & Freyberg, M. J. 1993, ApJ, 404, 403

Snowden, S. L., Freyberg, M. J., Plucinsky, P. P., et al. 1995, ApJ, 454, 643

Snowden, S. L., Hasinger, G., Jahoda, K., et al. 1994, ApJ, 430, 601

Snowden, S. L., McCammon, D., & Verter, F. 1993, ApJ, 409, L21

Snowden, S. L., Mebold, U., Hirth, W., Herbstmeier, U., & Schmitt, J. H. M. 1991, Science, 252, 1529

Spitzer, L. J. 1956, ApJ, 124, 20

Strüder, L., Briel, U., Dennerl, K., et al. 2001, A&A, 365, L18

Strickland, D. K., Heckman, T. M., Colbert, E. J. M., Hoopes, C. G., & Weaver, K. A. 2004, ApJS, 151, 193

Sutherland, R. S. & Dopita, M. A. 1993, ApJS, 88, 253

Tozzi, P., Rosati, P., Nonino, M., et al. 2001, ApJ, 562, 42

Trümper, J. 1984, Advances in Space Research, 3, 483

Trinchieri, G., Fabbiano, G., & Canizares, C. R. 1986, ApJ, 310, 637

Trinchieri, G., Fabbiano, G., & Kim, D.-W. 1997, A&A, 318, 361

Turner, M. J. L., Abbey, A., Arnaud, M., et al. 2001, A&A, 365, L27

Unsöld, A. & Baschek, B. 1988, Der neue Kosmos (Berlin ; New York : Springer, c1988. 4., vollig neubearbeitete Aufl.)

Voges, W., Aschenbach, B., Boller, T., et al. 1999, A&A, 349, 389

Wakker, B. P. 1991, A&A, 250, 499

Wakker, B. P., Savage, B. D., Sembach, K. R., et al. 2003, ApJS, 146, 1

Wakker, B. P. & van Woerden, H. 1991, A&A, 250, 509

Wakker, B. P. & van Woerden, H. 1997, ARA&A, 35, 217

Welsh, B. Y., Sallmen, S., & Lallement, R. 2004, A&A, 414, 261

Wilms, J., Allen, A., & McCray, R. 2000, ApJ, 542, 914

Woerden, H. V., Peletier, R. F., Schwarz, U. J., Wakker, B. P., & Kalberla, P. M. W. 1999, in ASP Conf. Ser. 165: The Third Stromlo Symposium: The Galactic Halo, 469–+

Wolfire, M. G., Hollenbach, D., McKee, C. F., Tielens, A. G. G. M., & Bakes, E. L. O. 1995, ApJ, 443, 152

List of Figures

List of Tables